INTERLAMINAR CRACK PROPAGATION IN THICK COMPOSITE SHELLS

by

Feridun Ozdil

A Dissertation Submitted to the Faculty of

The College of Engineering

In Partial Fulfillment of the Requirements for the Degree of

Doctor of Philosophy

Florida Atlantic University

Boca Raton, Florida

April 1999

INTERLAMINAR CRACK PROPAGATION IN THICK COMPOSITE SHELLS

by

Feridun Ozdil

This dissertation was prepared under the direction of the candidate's dissertation advisor, Dr. Leif A. Carlsson, Department of Mechanical Engineering, and has been approved by the members of his supervisory committee. It was submitted to the faculty of the College of Engineering and was accepted in partial fulfillment of the requirements for the degree of Doctor of Philosophy in Mechanical Engineering.

SUPERVISORY COMMITTEE:

Chairperson, Dr. L. A. Carlsson

Dr. G. Gaonkar

Dr. C. T. Tsai

Dr. G. Cai

Chairperson, Department of Mechanical Engineering

Dean, College of Engineering

Dean of Graduate Studies and Research

3/1/99
Date

ACKNOWLEDGEMENTS

I wish to express my gratitude to my dissertation advisor, Dr. L. A. Carlsson. His continuous support and guidance made it a pleasure to complete this work. My special thanks are due to the members of my supervisory committee, Dr. G. Gaonkar, Dr. C. T. Tsai, and Dr. G. Cai for their expertise and support. I am indebted to Dr. Y. Rajapakse of the Office of Naval Research (ONR) for sponsoring this research and his continuous support and encouragement. I am also grateful to Dr. P. Davies of the National French Oceanographic Research Organization (IFREMER) for his support and the provision of cylinder specimens examined in this work.

I give my deepest appreciation to my wife, Constanza, and my family. Their love, support, and patience have been vital throughout this work. I would like to thank also to my friends, Mr. M. Gonzalez and Ms. X. Li, for their assistance and support during this work. The assistance by Mrs. R. Chiucci with typing, Mr. P. Sip and Mr. L. Silverstein with machining, and Ms. Shawn Pennel with graphics work is also greatly appreciated.

ABSTRACT

Author:	Feridun Ozdil
Title:	Interlaminar Crack Propagation in Thick Composite Shells
Institution:	Florida Atlantic University
Dissertation Advisor:	Dr. Leif A. Carlsson
Degree:	Doctor of Philosophy
Year:	1999

Delamination growth has been investigated as a potential failure mechanism for filament-wound composite cylinders used for offshore and underwater structures. Analysis and experiments on DCB, ENF, and MMB beam fracture specimens machined from angle-ply laminate panels and filament-wound composite cylinders are presented. Bending analysis of beam fracture specimens machined from flat panels and composite cylinders was derived from first order shear deformation theory and one-dimensional expressions obtained from laminated plate and shell theories. For the DCB specimens, elastic foundation effects were modeled. Experiments on flat, glass/polyester laminate beam specimens considered $[0]_6$, $[\pm 30]_5$ and $[\pm 45]_5$ lay-ups with mid-plane delaminations. Experiments on beam specimens machined from composite cylinders

were conducted on $[\pm\theta]_6$ and $[\pm\theta]_{12}$ lay-ups with mid-surface delaminations where θ = 30°, 55° and 85°. For all lay-ups and specimen configurations, beam model predictions of compliance were in good agreement with experimental data over the range of laminate thicknesses, ply angles, and crack lengths examined. Fracture toughness for delamination propagation was examined for flat glass/polyester panels and glass/epoxy cylinders. The initiation value of mode II fracture toughness, G_{IIc}, was much larger than the initiation value of mode I fracture toughness G_{Ic}. The initiation value of mixed mode fracture toughness, G_c, increased with decreased ratio G_I/G_{II} and increased ply angle θ. Debonding of transversely oriented fiber bundles was observed as a major crack arrest and fracture resistance mechanism for the flat, glass/polyester angle-ply laminates. Bridging by interlaced fiber bundles and crack jumping to another interface contributed to crack arrest and limited the growth in the curved, glass/epoxy angle-ply laminates. For all lay-ups, the crack propagated in a non-uniform manner across the width of the specimen as explained by elastic coupling effects in the laminate beams of the cracked region.

TABLE OF CONTENTS

List of Figures

List of Tables

Chapter 1 INTRODUCTION

Thick-walled filament-wound composites are candidates for surface ship and naval submersible structures such as underwater vehicles and vessels [1] because they offer substantial weight reduction, good fatigue resistance, and low susceptibility to corrosion compared to metals. Besides graphite fibers in an epoxy or thermoplastic matrix, there has been considerable interest in glass fibers combined with epoxy, polyester and vinyl-ester matrices. Since marine structures are usually less weight critical than aerospace structures, glass fiber composites may provide optimal design solutions [2].

Applications of composites to thick-walled structures subject to biaxial compression loads are currently limited by their inability to attain the theoretical compressive strength of the material because of processing and manufacturing induced defects in the material and structure [2,3]. Besides the necessity of sufficient compression strength of the material, an important, but less researched issue is the degrading influence of an interlaminar defect, "delamination", on the integrity of such a structure. A delamination that involves crack propagation between the plies in a laminated composite may occur as a result of contaminations during lay-up, accumulation of voids during processing, shock or blast loadings, or hard object impact loading during service of the

structure. In externally pressurized filament wound structures, Fig. 1.1, a delamination between angle-plies may propagate leading to buckling instability failure and reduce the pressure capability of such structures [3,4], and there is much need to investigate this issue in more detail.

Although structural integrity of thick composite shells is a key issue in the design and manufacture of surface ship and underwater structures, the area of delamination propagation has received little attention. At present, there are no specifications on the allowable size of defects for nondestructive evaluation of such structures, and the influences of wall thickness, curvature, pressure, and lay-up on defect propagation remain to be determined. Defect criticality assessment of marine structures should thus consider analysis of interlaminar cracks in thick and curved composite structures.

This dissertation addresses delamination growth as potential failure mechanism for filament-wound composite cylinders, Fig. 1.1. The overall objective is to establish experimental and analytical methods for characterization of interlaminar crack propagation in such structures. Chapter 2 of this dissertation will first provide a brief background on the mechanics of composite plates and shells. In Chapter 3, bending analyses will be developed to evaluate compliance and strain energy release rate for flat and angle-ply laminate fracture specimens machined from filament-wound composite cylinders. In particular, the Double Cantilever Beam (DCB), End-Notched Flexure (ENF) and the Mixed Mode Bending (MMB) specimens schematically depicted in Fig. 1.2 will be analyzed. The analytical compliance predictions will be compared with previously

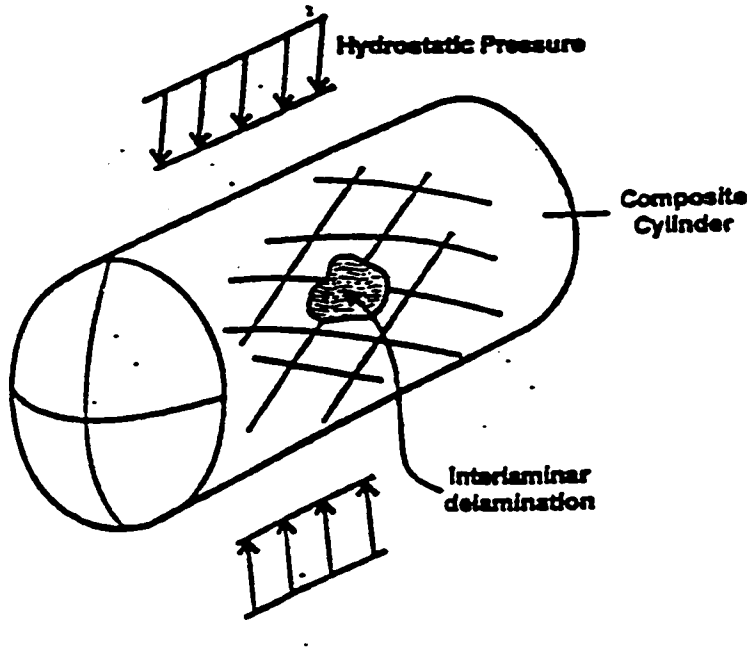

Fig. 1.1 A filament wound composite under hydrostatic pressure.

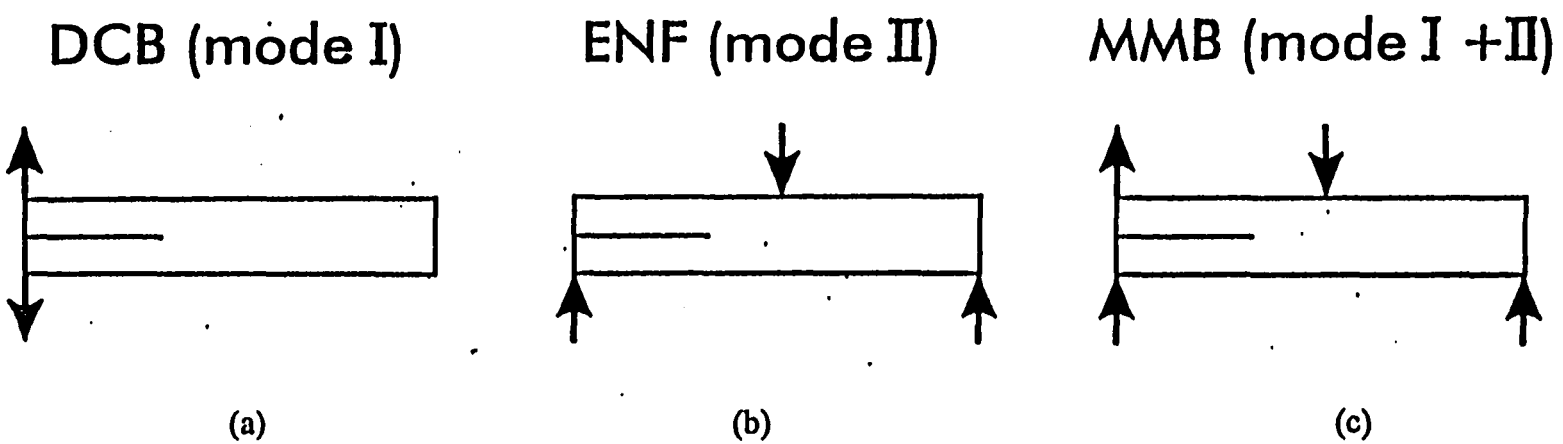

Fig. 1.2 Schematic illustrations of a) DCB, b) ENF, and c) MMB tests.

developed models and experimental data to determine the viability of the laminated beam analysis. Chapter 3 will also discuss evaluation of fracture toughness from experimental data and crack front shapes in the beam fracture specimens. Chapter 4 will establish experimental characterization of delamination propagation in glass/polyester and glass/epoxy beam fracture specimens machined from angle-ply laminate panels and filament-wound cylindrical shells. The experimental program will include basic mechanical property characterization of the composites and fracture testing of unidirectional and angle-ply, flat and curved beam specimens under mode I (DCB), mode II (ENF), and mixed mode (I+II) (MMB) loading, Fig. 1.2, and examination of crack growth mechanisms. Special emphasis will be put on the details of load versus displacement (P-δ) responses, crack growth and arrest mechanisms, fracture resistance curves (R-curves), and shape of delamination front following a fracture test. The crack front shapes observed in the experiments will be discussed and compared with previously published guidelines. The experimentally determined critical fracture loads will be employed in energy release rate expressions derived in Chapter 3 to determine the delamination fracture toughness of the beam fracture specimens. In addition, for comparison purposes, the delamination fracture toughness will be determined from the experimental compliance calibration method. The conclusions drawn in this research and recommendations for further study will be presented in Chapter 5.

Chapter 2 BACKGROUND

2.1 Anisotropic Elasticity

The stress-strain relation is a basic descriptor for quantifying the mechanical response of materials. The mechanical response of a composite material exhibits a strong dependence upon the direction in which the loads are applied. Therefore, the design and analysis of anisotropic composite structures requires a knowledge of the stress-strain response characteristics for all directions in which loads may be anticipated. Fortunately, it can be shown that the properties in any direction can be specified in terms of a minimum number of properties characterized along certain special directions of an anisotropic material [5]. The minimum number of properties required to completely characterize the stress-strain behavior of an anisotropic material is in turn determined by the materials symmetry associated with the microstructure of the material [5].

2.1.1 Stress-Strain Behavior Relations for Anisotropic Materials

The generalized Hooke's law relating stresses to strains can be written in the following matrix form [6],

$$\begin{bmatrix} \sigma_1 \\ \sigma_2 \\ \sigma_3 \\ \tau_{23} \\ \tau_{31} \\ \tau_{12} \end{bmatrix} = \begin{bmatrix} C_{11} & C_{12} & C_{13} & C_{14} & C_{15} & C_{16} \\ C_{12} & C_{22} & C_{23} & C_{24} & C_{25} & C_{26} \\ C_{13} & C_{23} & C_{33} & C_{34} & C_{35} & C_{36} \\ C_{14} & C_{24} & C_{34} & C_{44} & C_{45} & C_{46} \\ C_{15} & C_{25} & C_{35} & C_{45} & C_{55} & C_{56} \\ C_{16} & C_{26} & C_{36} & C_{46} & C_{56} & C_{66} \end{bmatrix} \begin{bmatrix} \varepsilon_1 \\ \varepsilon_2 \\ \varepsilon_3 \\ \gamma_{23} \\ \gamma_{31} \\ \gamma_{12} \end{bmatrix} \tag{2.1}$$

or in contracted notation as [7],

$$\sigma_i = C_{ij}\,\varepsilon_j \tag{2.2}$$

where σ_i are the stress components, C_{ij} is the stiffness matrix, and ε_j are the strain components. The contracted notation is used rather than the tensor notation for three-dimensional stresses and strains. The stiffness matrix, C_{ij}, is symmetric, i.e., $C_{ij} = C_{ji}$, and only 21 of the constants are independent. Equation (2.1) is the most general expression within the framework of linear elasticity characterizing *anisotropic* materials since there are no planes of symmetry for the material properties.

For an *orthotropic* material, there are three orthogonal planes of material property symmetry. The stress-strain relations then become [7],

$$\begin{bmatrix} \sigma_1 \\ \sigma_2 \\ \sigma_3 \\ \tau_{23} \\ \tau_{31} \\ \tau_{12} \end{bmatrix} = \begin{bmatrix} C_{11} & C_{12} & C_{13} & 0 & 0 & 0 \\ C_{12} & C_{22} & C_{23} & 0 & 0 & 0 \\ C_{13} & C_{23} & C_{33} & 0 & 0 & 0 \\ 0 & 0 & 0 & C_{44} & 0 & 0 \\ 0 & 0 & 0 & 0 & C_{55} & 0 \\ 0 & 0 & 0 & 0 & 0 & C_{66} \end{bmatrix} \begin{bmatrix} \varepsilon_1 \\ \varepsilon_2 \\ \varepsilon_3 \\ \gamma_{23} \\ \gamma_{31} \\ \gamma_{12} \end{bmatrix} \tag{2.3}$$

Note that there are no interaction between normal stresses σ_1, σ_2, and σ_3 and shear strains γ_{23}, γ_{31}, and γ_{12}. Similarly, there is no interaction between shear stresses and normal strains as well as none between shear stresses and shear strains in different planes. Note also that there are only *nine* independent constants in the stiffness matrix.

If there is one plane in which the mechanical properties are equal in all directions, then the material is termed *transversely isotropic*. If, for example, the 2-3 plane is the special plane of isotropy, then the 2 and 3 subscripts on the stiffnesses are interchangeable. The stress-strain relations then have only *five* independent constants and are [7],

$$\begin{bmatrix} \sigma_1 \\ \sigma_2 \\ \sigma_3 \\ \tau_{23} \\ \tau_{31} \\ \tau_{12} \end{bmatrix} = \begin{bmatrix} C_{11} & C_{12} & C_{12} & 0 & 0 & 0 \\ C_{12} & C_{22} & C_{23} & 0 & 0 & 0 \\ C_{12} & C_{23} & C_{22} & 0 & 0 & 0 \\ 0 & 0 & 0 & (C_{22}-C_{23})/2 & 0 & 0 \\ 0 & 0 & 0 & 0 & C_{55} & 0 \\ 0 & 0 & 0 & 0 & 0 & C_{55} \end{bmatrix} \begin{bmatrix} \varepsilon_1 \\ \varepsilon_2 \\ \varepsilon_3 \\ \gamma_{23} \\ \gamma_{31} \\ \gamma_{12} \end{bmatrix} \tag{2.4}$$

2.1.2 Transformation of Elastic Stiffnesses Under Rotation of Coordinate Axes

The stress-strain relations given in eqs. (2.1) through (2.4) are defined in the principal material directions which are normals to three mutually orthogonal planes of symmetry. However, in engineering applications, the principal directions often do not coincide with coordinate directions that are geometrically natural to the solution of the problem. For example, in this work we consider helically wound fiberglass cylindrical

shells, Fig. 2.1. There, the coordinates natural to the solution of the shell problem are x, y, z, whereas the principal material coordinates are x′, y′, z′ (z′ = z). Another common example is a laminated plate with laminae (or plies) at different orientations.

To transform stiffnesses of an orthotropic material corresponding to a rotation of the 1-2 plane around the 3-axis, Fig. 2.2, the following equations apply [5],

$$
\begin{aligned}
C_{11}' &= C_{11}m^4 + 2(C_{12} + 2C_{66})m^2n^2 + C_{22}n^4 \\
C_{12}' &= C_{12}(m^4 + n^4) + (C_{11} + C_{22} - 4C_{66})m^2n^2 \\
C_{13}' &= C_{13}m^2 + C_{23}n^2 \\
C_{16}' &= -[(C_{11} - C_{12} - 2C_{66})m^2 - (C_{22} - C_{12} - 2C_{66})n^2]mn \\
C_{22}' &= C_{22}m^4 + 2(C_{12} + 2C_{66})m^2n^2 + C_{11}n^4 \\
C_{23}' &= C_{23}m^2 + C_{13}n^2 \\
C_{26}' &= [(C_{22} - C_{12} - 2C_{66})m^2 - (C_{11} - C_{12} - 2C_{66})n^2]mn \\
C_{33}' &= C_{33} \\
C_{36}' &= -(C_{13} - C_{23})mn \\
C_{44}' &= C_{44}m^2 + C_{55}n^2 \\
C_{45}' &= -(C_{55} - C_{44})mn \\
C_{55}' &= C_{55}m^2 + C_{44}n^2 \\
C_{66}' &= (C_{11} + C_{22} - 2C_{12})m^2n^2 + C_{66}(m^2 - n^2)^2
\end{aligned}
\tag{2.5}
$$

where $m = \cos\theta$, $n = \sin\theta$, θ is the angle of rotation, Fig. 2.2, and C_{ij}' are the components of the transformed stiffness matrix. Note that C_{ij}' is not orthotropic since C_{45}', C_{16}', C_{36}' are non-zero.

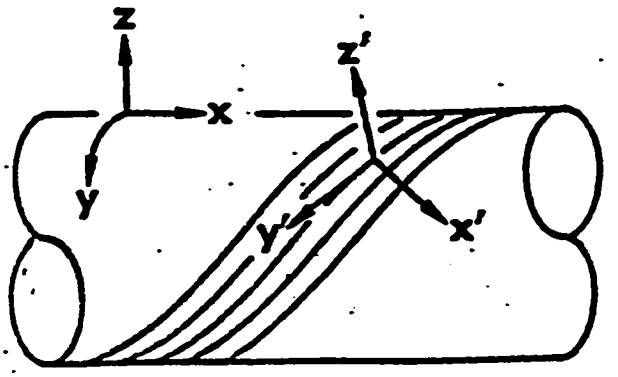

Fig. 2.1 Principal and natural coordinates for a helically wound fiberglass-cylindrical shell.

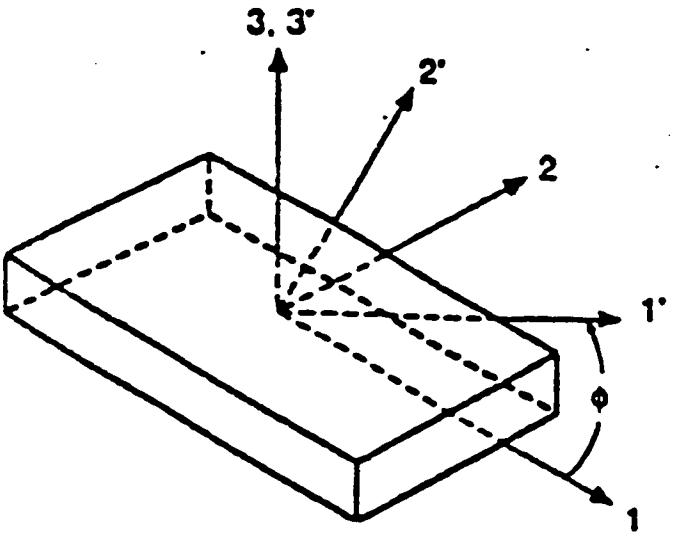

Fig. 2.2 Rotation of the 1-2 plane around the 3-axis.

2.1.3 Lamina Stress-Strain Behavior

The following stress-strain relations apply in the principal material coordinates (denoted as 1-2-3 coordinate system) for a lamina under plane stress [7],

$$\begin{Bmatrix}\sigma_1\\ \sigma_2\\ \sigma_3\end{Bmatrix}=\begin{bmatrix}Q_{11} & Q_{12} & 0\\ Q_{12} & Q_{22} & 0\\ 0 & 0 & Q_{66}\end{bmatrix}\begin{Bmatrix}\varepsilon_1\\ \varepsilon_2\\ \varepsilon_{12}\end{Bmatrix} \tag{2.6}$$

The reduced stiffnesses, Q_{ij}, may be related to the C_{ij}'s defined in eq. (2.1), see Ref. [5], and are defined in terms of engineering constants as [7],

$$\begin{aligned} Q_{11} &= \frac{E_1}{1-\nu_{12}\nu_{21}}\\ Q_{12} &= \frac{\nu_{12}\,E_2}{1-\nu_{12}\nu_{21}} = \frac{\nu_{21}\,E_1}{1-\nu_{12}\nu_{21}}\\ Q_{22} &= \frac{E_2}{1-\nu_{12}\nu_{21}}\\ Q_{66} &= G_{12} \end{aligned} \tag{2.7}$$

where E_1 and E_2 are the extensional moduli in the fiber (1) and transverse to fiber (2) directions, respectively, and ν_{12} and ν_{21} are the Poisson's ratios. In any other coordinate system in the plane of the lamina, Fig. 2.2, the stresses are [7],

$$\begin{Bmatrix}\sigma_x\\ \sigma_y\\ \tau_{xy}\end{Bmatrix}=\begin{bmatrix}Q_{11}' & Q_{12}' & Q_{16}'\\ Q_{12}' & Q_{22}' & Q_{26}'\\ Q_{16}' & Q_{26}' & Q_{66}'\end{bmatrix}\begin{Bmatrix}\varepsilon_x\\ \varepsilon_y\\ \gamma_{xy}\end{Bmatrix} \tag{2.8}$$

where the transformed reduced stiffnesses, Q_{ij}', are defined in terms of Q_{ij} and orientation angle θ, Fig. 2.2.

2.2 Classical Laminated Plate Theory

One of the most useful forms for composite materials is that of a layered or laminated system. These layers may be of the same fiber/matrix system or different systems and may be stacked at arbitrary fiber orientations. The layers (or plies may be visualized as any region of consistent fiber orientation. Classical laminated plate theory (CLPT) offers a systematic way to study laminates consisting of arbitrarily oriented unidirectional plies. By use of CLPT, we consistently proceed from the basic building block, the lamina (or ply), to the end result, a structural laminate. The results of CLPT may be employed to calculate stress and strain at any point in the material and effective elastic properties in any direction, and determine whether the material has failed at any point (in conjunction with a strength theory) [8].

The mathematical basis of CLPT borrows heavily from classical plate theory (CPT) [9] extended to laminated composites. It should be noted that in CLPT, the fiber and matrix properties are no longer identified directly but replaced by effective homogeneous ply properties [8].

2.2.1 Strain and Stress Variation in a Laminate

Knowledge of the variation of stress and strain through the laminate thickness is essential to the definition of the mechanical response of a laminate. CLPT assumes perfectly bonded laminae. Moreover, the bonds are presumed to be infinitesimally thin as well as non-deformable. That is, the displacements are continuous across lamina

boundaries so that no lamina can move relative to another [7]. Thus the lamina acts as a single layer.

If the laminate is thin, cross-sections originally straight and perpendicular to the mid-surface of the laminate are assumed to remain so after the laminate is extended or bent, Fig. 2.3. In addition, the normals are presumed to have constant length, i.e., $\varepsilon_z = 0$. The foregoing assumptions of the behavior of the single layer that represents the laminate constitutes the familiar Kirchhoff hypothesis for plates [7].

The Kirchhoff hypothesis leads to the following displacement field [10],

$$\begin{aligned} u &= u_0(x,y) + z\frac{\partial w_o}{\partial x} \\ v &= v_0(x,y) + z\frac{\partial w_o}{\partial y} \\ w &= w_0(x,y) \end{aligned} \tag{2.9}$$

where u, v, and w are the displacements in the x, y, and z directions of any point in the laminate, and u_0, v_0, and w_0 are the corresponding displacements of the mid-surface, Fig. 2.3.

The laminate strains have been reduced to ε_x, ε_y, γ_{xy} by virtue of Kirchhoff hypothesis, i.e., $\varepsilon_z = \gamma_{xz} = \gamma_{yz} = 0$. For small strains, linear elasticity theory defines the remaining strains in terms of displacement as [7],

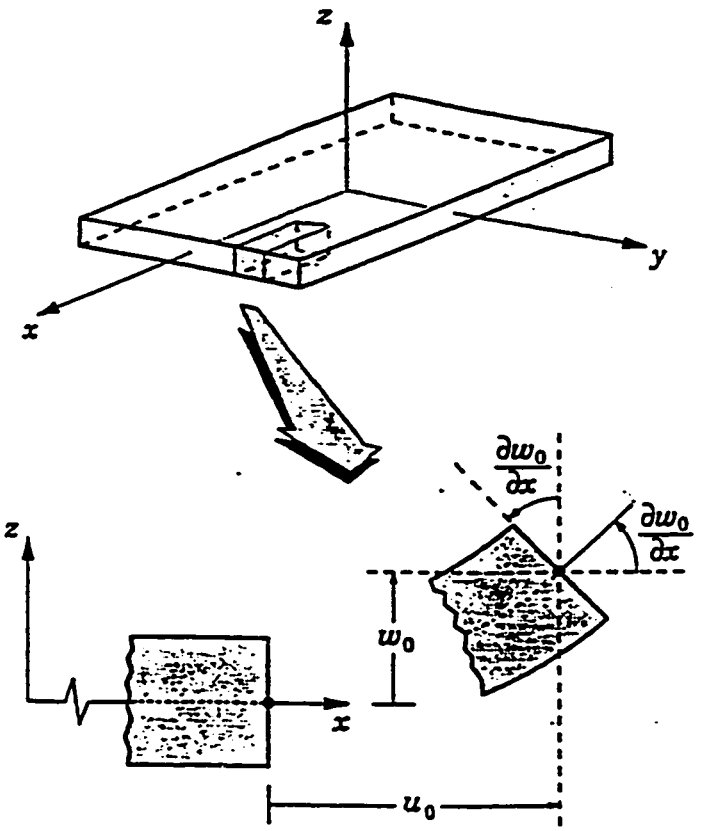

Fig. 2.3 Kinematics of deformation of a plate under the assumptions of the classical plate theory (CLPT).

$$\varepsilon_x = \frac{\partial u}{\partial x}$$
$$\varepsilon_y = \frac{\partial \mathrm{v}}{\partial y} \tag{2.10}$$
$$\gamma_{xy} = \frac{\partial u}{\partial x} + \frac{\partial \mathrm{v}}{\partial y}$$

Substituting the displacements u and v in eq. (2.9) into eq. (2.10), the strains become [7],

$$\begin{Bmatrix} \varepsilon_x \\ \varepsilon_y \\ \gamma_{xy} \end{Bmatrix} = \begin{Bmatrix} \varepsilon_x^{\,0} \\ \varepsilon_y^{\,0} \\ \gamma_{xy}^{\,0} \end{Bmatrix} + z \begin{Bmatrix} \kappa_x \\ \kappa_y \\ \kappa_{xy} \end{Bmatrix} \tag{2.11}$$

where the mid-surface strains are,

$$\begin{Bmatrix} \varepsilon_x^{\,0} \\ \varepsilon_y^{\,0} \\ \gamma_{xy}^{\,0} \end{Bmatrix} = \begin{Bmatrix} \dfrac{\partial u_o}{\partial x} \\ \dfrac{\partial \mathrm{v}_0}{\partial y} \\ \dfrac{\partial u_0}{\partial y} + \dfrac{\partial \mathrm{v}_0}{\partial x} \end{Bmatrix} \tag{2.12}$$

and the mid-surface curvatures are,

$$\begin{Bmatrix} \kappa_x \\ \kappa_y \\ \kappa_{xy} \end{Bmatrix} = -\begin{Bmatrix} \dfrac{\partial^2 w_o}{\partial x^2} \\ \dfrac{\partial^2 \mathrm{w}_0}{\partial y^2} \\ 2\dfrac{\partial^2 w_0}{\partial x \partial y} \end{Bmatrix} \tag{2.13}$$

Thus, the Kirchhoff's hypothesis has been readily verified to imply a linear variation of strain through the laminate thickness.

The stress-strain relations in arbitrary coordinates, eq. (2.8), are useful in the definition of the laminate stiffnesses because of the arbitrary orientation of the constituent laminae. Both eqs. (2.6) and (2.8) can be thought of stress-strain relations for the k^{th} layer of a multilayered laminate. Substituting eq. (2.11) into eq. (2.8), the stresses in the k^{th} layer of a laminate can be expressed in terms of the laminate mid-surface strains and curvatures [7],

$$\begin{Bmatrix} \sigma_x \\ \sigma_y \\ \tau_{xy} \end{Bmatrix}_k = \begin{bmatrix} \bar{Q}_{11} & \bar{Q}_{12} & \bar{Q}_{16} \\ \bar{Q}_{12} & \bar{Q}_{22} & \bar{Q}_{26} \\ \bar{Q}_{16} & \bar{Q}_{26} & \bar{Q}_{66} \end{bmatrix}_k \left\{ \begin{Bmatrix} \varepsilon_x^0 \\ \varepsilon_y^0 \\ \gamma_{xy}^0 \end{Bmatrix} + z \begin{Bmatrix} \kappa_x \\ \kappa_y \\ \kappa_{xy} \end{Bmatrix} \right\} \tag{2.14}$$

Since the $\bar{Q}_{ij}$ can be different for each layer of the laminate, the stress variation through the laminate thickness is in general linear within each ply only, even though the strain variation is linear.

2.2.2 Laminate Constitutive Relations

The force and moment resultants (defined per unit width) for an N-layered laminate, Fig. 2.4, are [7],

$$\begin{Bmatrix} N_x \\ N_y \\ N_{xy} \end{Bmatrix} = \sum_{k=1}^{N} \int_{z_{k-1}}^{z_k} \begin{Bmatrix} \sigma_x \\ \sigma_y \\ \tau_{xy} \end{Bmatrix}_k dz \tag{2.15}$$

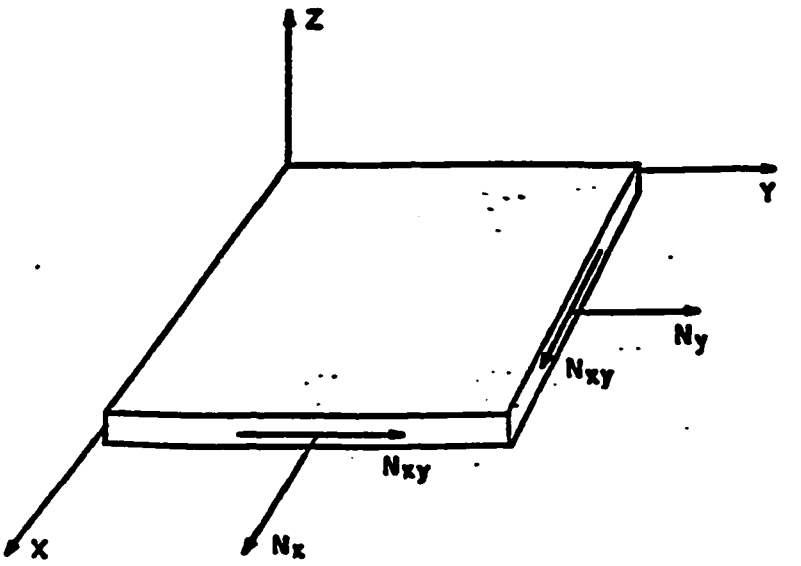

(a)

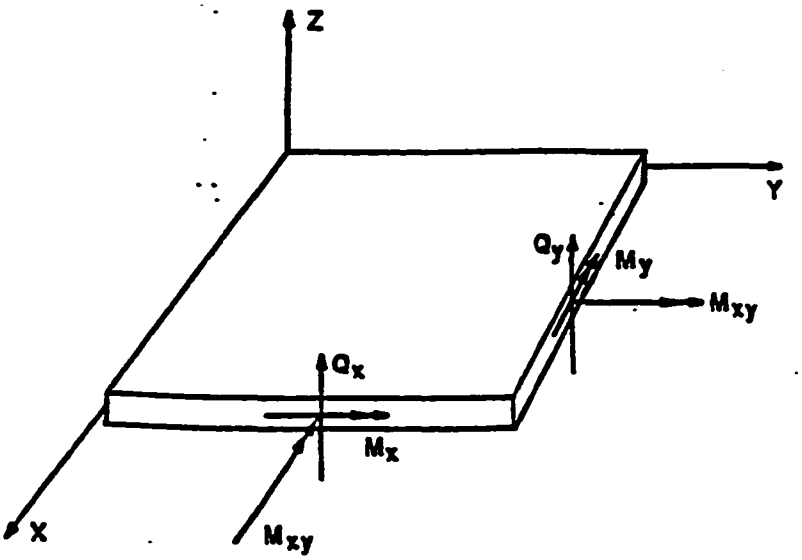

(b)

Fig. 2.4 In-plane normal and shear force (a) and moment and transverse shear force resultants (b) of a flat laminate.

$$\begin{Bmatrix} M_x \\ M_y \\ M_{xy} \end{Bmatrix} = \sum_{k=1}^{N} \int_{z_{k-1}}^{z_k} \begin{Bmatrix} \sigma_x \\ \sigma_y \\ \tau_{xy} \end{Bmatrix}_k z\,dz \tag{2.16}$$

where z_k and z_{k-1} are defined in Fig. 2.5. Note that $z_0 = -t/2$ where t is the laminate thickness. The force and moment resultants do not depend on z, but are functions of x and y, the in-plane coordinates of the laminate mid-surface. Substituting the lamina stress-strain relations, eq. (2.8), into eqs. (2.15) and (2.16) and recalling that the stiffness matrix for a lamina is constant within the lamina and that mid-surface strains and curvatures, eqs. (2.12) and (2.13), are not functions of z, we obtain [7],

$$\begin{Bmatrix} N_x \\ N_y \\ N_{xy} \end{Bmatrix} = \begin{bmatrix} A_{11} & A_{12} & A_{16} \\ A_{12} & A_{22} & A_{26} \\ A_{16} & A_{26} & A_{66} \end{bmatrix} \begin{Bmatrix} \varepsilon_x^{\,0} \\ \varepsilon_y^{\,0} \\ \gamma_{xy}^{\,0} \end{Bmatrix} + \begin{bmatrix} B_{11} & B_{12} & B_{16} \\ B_{12} & B_{22} & B_{26} \\ B_{16} & B_{26} & B_{66} \end{bmatrix} \begin{Bmatrix} \kappa_x \\ \kappa_y \\ \kappa_{xy} \end{Bmatrix} \tag{2.17}$$

$$\begin{Bmatrix} M_x \\ M_y \\ M_{xy} \end{Bmatrix} = \begin{bmatrix} B_{11} & B_{12} & B_{16} \\ B_{12} & B_{22} & B_{26} \\ B_{16} & B_{26} & B_{66} \end{bmatrix} \begin{Bmatrix} \varepsilon_x^{\,0} \\ \varepsilon_y^{\,0} \\ \gamma_{xy}^{\,0} \end{Bmatrix} + \begin{bmatrix} D_{11} & D_{12} & D_{16} \\ D_{12} & D_{22} & D_{26} \\ D_{16} & D_{26} & D_{66} \end{bmatrix} \begin{Bmatrix} \kappa_x \\ \kappa_y \\ \kappa_{xy} \end{Bmatrix} \tag{2.18}$$

where

$$A_{ij} = \sum_{k=1}^{N} (Q_{ij}^{'})_k \, (z_k - z_{k-1}) \tag{2.19}$$

$$B_{ij} = \frac{1}{2} \sum_{k=1}^{N} (Q_{ij}^{'})_k \, (z_k^{\,2} - z_{k-1}^{\,2}) \tag{2.20}$$

$$D_{ij} = \frac{1}{3} \sum_{k=1}^{N} (Q_{ij}^{'})_k \, (z_k^{\,3} - z_{k-1}^{\,3}) \tag{2.21}$$

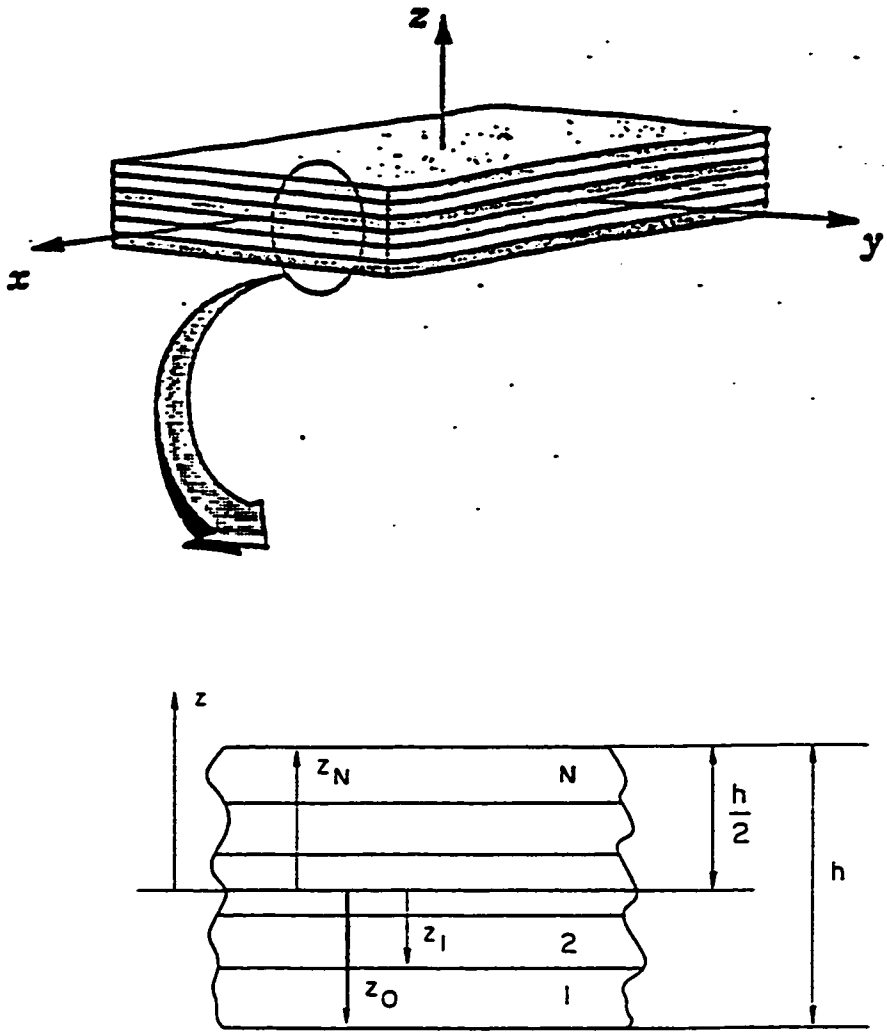

Fig. 2.5 Geometry of an N-layered laminate.

where the A_{ij} are called extensional stiffnesses, B_{ij} are called coupling stiffnesses, and D_{ij} are called bending stiffnesses. Equations (2.19) to (2.21) can be written in abbreviated notation,

$$\begin{bmatrix} N \\ M \end{bmatrix} = \begin{bmatrix} A & B \\ B & D \end{bmatrix} \begin{bmatrix} \varepsilon^{o} \\ K \end{bmatrix} \tag{2.22}$$

The laminate stiffness matrices, A, B, and D, defines a relationship between the stress resultants (i.e., loads) applied to a laminate element and the corresponding reference surface strains and curvatures (i.e., deformations). This form is a direct result of the Kirchhoff hypothesis, the plane stress assumption, and the definition of the stress resultants. The matrices A, B, D contain all information that is necessary to define the laminate, i.e., ply material properties, fiber orientation, thickness, and location.

Equations (2.21) and (2.22) indicate that certain elastic coupling effects occur in composite laminates as illustrated in Fig. 2.6. The presence of B_{ij} terms implies coupling between bending and extension of a laminate. Thus, an extensional force results in not only extensional deformations, but also twisting and/or twisting of the laminate. Also such a laminate can not be subjected to a moment without at the same time suffering extension of the mid-surface. For laminates that are symmetric in both geometry and material properties about the mid-surface, the B_{ij} terms and corresponding couplings, Fig. 2.6, vanish. The other important coupling terms are A_{16} and A_{26} which indicate extensional/shear coupling, Fig. 2.6, and D_{12} bending/bending coupling while D_{16} and D_{26} indicate bending/twist coupling, Fig. 2.6.

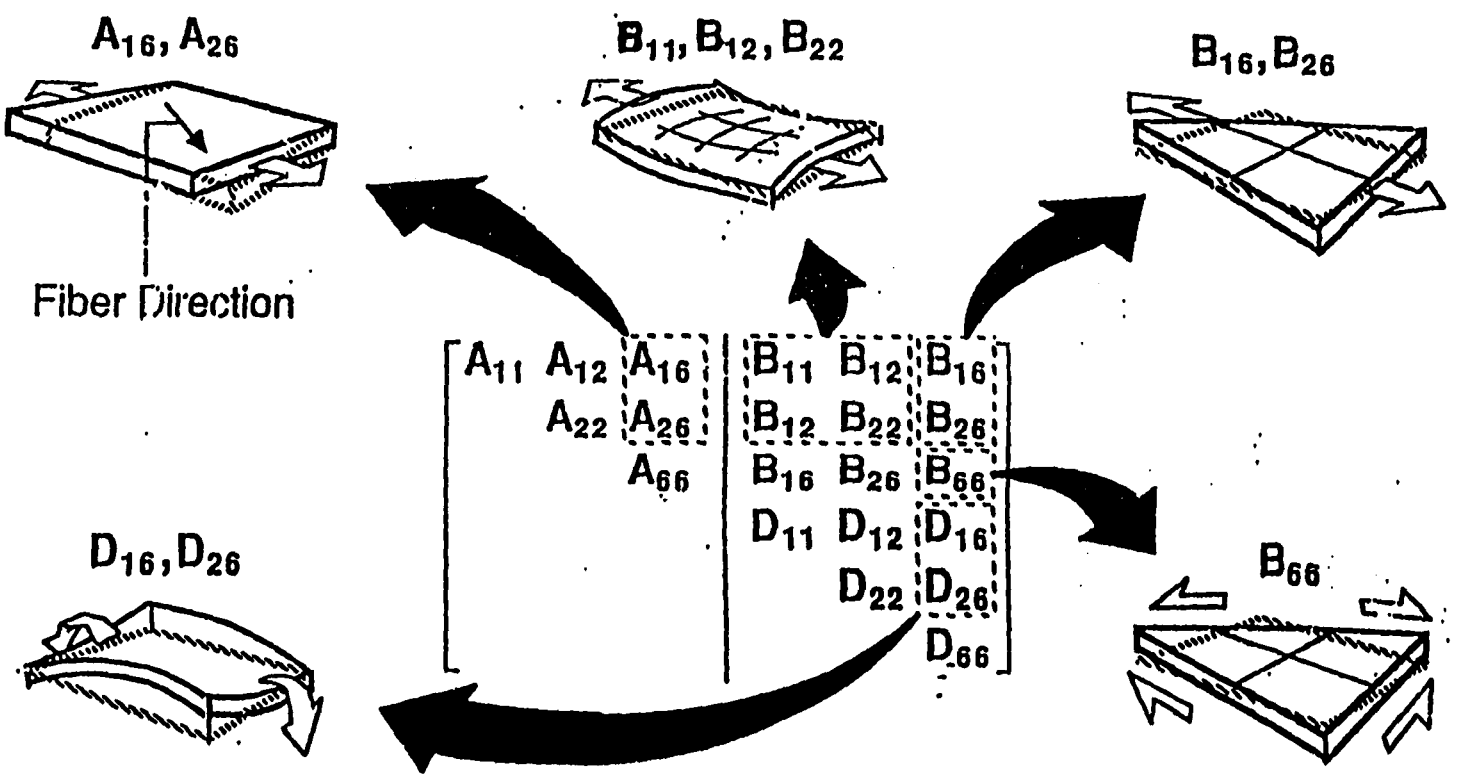

Fig. 2.6 Illustrations of coupling phenomena in laminated composites.

2.2.3 Shear Deformation Laminated Plate Theory

The transverse shear moduli of composite materials are usually very low compared to the in-plane longitudinal extensional moduli, with the result that transverse shear deformation can be of considerable importance. For composites having a large ratio of in-plane Young's modulus to interlaminar shear modulus and a ratio of in-plane dimensions to thickness less than ten, significant departure from CLPT was observed [6]. As a result, it may be necessary to include the effect of transverse shear deformation in the analysis of composite plates and shells.

In the first order shear deformation plate theory (SLPT), the Kirchhoff hypothesis, See Sect. 2.2, is relaxed such that the transverse normals do remain straight but not orthogonal to the mid-surface after deformation, see Fig. 2.7 [10]. This amounts to including transverse shear strains γ_{xz} and γ_{yz} in the theory.

Under the same assumptions as in CLPT, the displacement field of the SLPT is of the form [10],

$$\begin{aligned} u &= u_0(x,y) + z\varphi_x(x,y) \\ v &= v_0(x,y) + z\varphi_y(x,y) \\ w &= w_0(x,y) \end{aligned} \tag{2.23}$$

Note that,

$$\frac{\partial u}{\partial z} = \varphi_x \quad , \quad \frac{\partial v}{\partial z} = \varphi_y \tag{2.24}$$

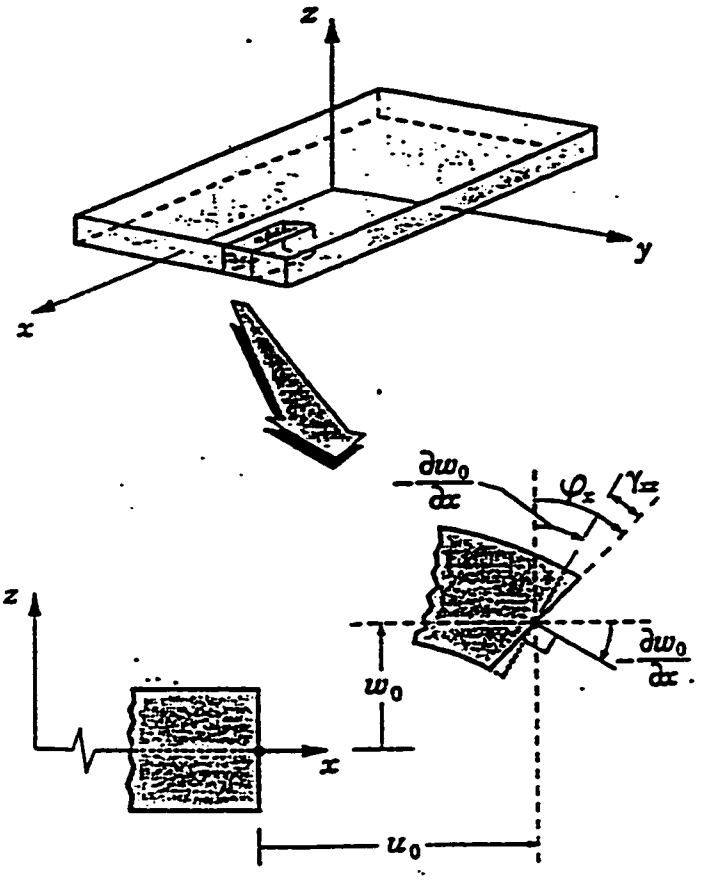

Fig. 2.7 Kinematics of deformation of a plate under the assumptions of the first order shear deformation plate theory (SLPT).

which shows that φ_x and φ_y are the rotations of a transverse normal about the y- and x-axes, respectively, Fig. 2.7. Using eqs. (2.23) in conjunction with strain-displacement relations, eq. (2.10), yields,

$$\begin{aligned} \varepsilon_x &= \varepsilon_x^{\circ} + z\kappa_x \\ \varepsilon_y &= \varepsilon_y^{\circ} + z\kappa_y \\ \gamma_{xy} &= \gamma_{xy}^{\circ} + z\kappa_{xy} \end{aligned} \tag{2.25}$$

which are of the same form as those of the CLPT, eq. (2.11), where $[\varepsilon^{\circ}]$ are the mid-surface strains defined in eq. (2.12), and,

$$\kappa_x = \frac{\partial \varphi_x}{\partial x}, \quad \kappa_y = \frac{\partial \varphi_y}{\partial y}, \quad \kappa_{xy} = \frac{\partial \varphi_x}{\partial y} + \frac{\partial \varphi_y}{\partial x} \tag{2.26}$$

In addition, the interlaminar shear strains, Fig. 2.7, are given by [6],

$$\begin{aligned} \gamma_{xz} &= \varphi_x + \frac{\partial w}{\partial x} \\ \gamma_{yz} &= \varphi_y + \frac{\partial w}{\partial y} \end{aligned} \tag{2.27}$$

Using eq. (2.25) in conjunction with the assumption of plane stress within each ply, eq. (2.7), and the definition of force and moment resultants, eqs. (2.17) and (2.18), we obtain a constitutive relation of exactly the same form as given by eq. (2.22),

$$\begin{bmatrix} N \\ M \end{bmatrix} = \begin{bmatrix} A & B \\ B & D \end{bmatrix} \begin{bmatrix} \varepsilon^0 \\ \kappa \end{bmatrix} \tag{2.28}$$

where the stiffness matrices A, B, and D are defined by eqs. (2.19) to (2.21). The shear force resultants are [6],

$$(Q_x, Q_y) = \int_{-h/2}^{h/2} (\tau_{xz}^{(k)}, \tau_{yz}^{(k)})\, dz \tag{2.29}$$

where the interlaminar shear stresses τ_{xz} and τ_{yz} are obtained from [6],

$$\begin{bmatrix} \tau_{yz}^{(k)} \\ \tau_{xz}^{(k)} \end{bmatrix} = \begin{bmatrix} C_{44}' & C_{45}' \\ C_{45}' & C_{55}' \end{bmatrix}_k \begin{bmatrix} \gamma_{yz} \\ \gamma_{xz} \end{bmatrix} \tag{2.30}$$

where the anisotropic shear moduli C_{ij}' (i,j = 4,5) are defined by eq. (2.5) and the interlaminar shear strains, γ_{xz} and γ_{yz}, are given by eq. (2.27). Integration of eq. (2.29) using eq. (2.30) yields [6],

$$\begin{bmatrix} Q_y \\ Q_x \end{bmatrix} = k \begin{bmatrix} A_{44} & A_{45} \\ A_{45} & A_{55} \end{bmatrix} \begin{bmatrix} \gamma_{yz} \\ \gamma_{xz} \end{bmatrix} \tag{2.31}$$

where k is a shear correction factor, and,

$$A_{ij} = \int_{-h/2}^{h/2} C_{ij}'\, dz = \sum_{k=1}^{N} (C_{ij}')_k \, (z_k - z_{k-1}) \qquad (i, j = 4,5) \tag{2.32}$$

2.4 Laminated Shell Theory

In the previous sections, we have considered analysis of flat laminated plates. Several structures, however, have curvature in at least in one direction such as the cylinders considered herein, Fig. 1.1. In this section, a first order theory including the

effect of transverse shear is reviewed. Consideration will be given to cylindrical shells of shallow curvature in order to utilize simplifying assumptions in developing the governing equations. Figure 2.8 illustrates a cylindrical shell element of constant radius R. As in the case of flat plates of rectangular cross-section, the thickness and in-plane dimensions are denoted by h, a and b, respectively. The displacements in the x, s and z directions are denoted by u, v, and w, respectively. The radius of the shell, R, is assumed to be much larger than the thickness, h. In addition, transverse shear strains γ_{xz} and γ_{sz} are considered as discussed in Sect. 2.3. The remaining assumptions are the same as those for flat plates [6].

The classical theory of elasticity gives the following strain-displacement relations for the shell element shown in Fig. 2.8 [6],

$$\varepsilon_x = \frac{\partial u}{\partial x}, \quad \varepsilon_s = \frac{1}{(1+z/R)}\frac{\partial \mathrm{v}}{\partial s} + \frac{w}{R}, \quad \varepsilon_z = \frac{\partial w}{\partial z} = 0$$

$$\gamma_{xz} = \frac{1}{(1+z/R)}\frac{\partial w}{\partial s} + \frac{\partial \mathrm{v}}{\partial z} - \frac{\mathrm{v}}{R(1+z/R)} \tag{2.33}$$

$$\gamma_{xz} = \frac{\partial u}{\partial z} + \frac{\partial w}{\partial x}, \quad \gamma_{xs} = \frac{\partial \mathrm{v}}{\partial x} + \frac{1}{(1+z/R)}\frac{\partial u}{\partial s}$$

The first order shear deformation shell theory assumes the following displacements [6],

$$\begin{aligned} u &= u_0(x,s) + z\psi_x(x,s) \\ \mathrm{v} &= \mathrm{v}_0(x,s) + z\psi_s(x,s) \\ w &= w_0(x,s) \end{aligned} \tag{2.34}$$

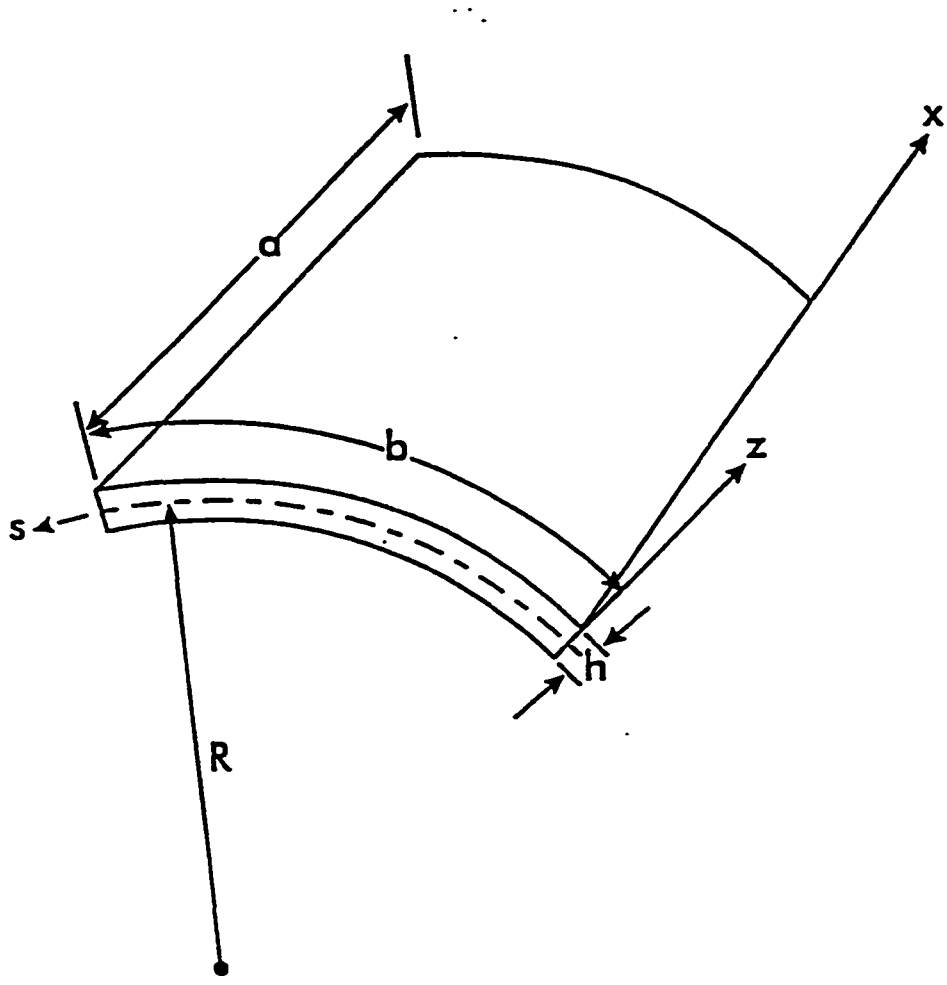

Fig. 2.8 Nomenclature for a cylindrical shell.

where u_0,v_0, and w_0 are the axial, tangential, and transverse displacements of the mid-surface, respectively, and ψ_x and ψ_s are the rotation of cross-sections originally normal to the x and s axes [6]. Since the shell is assumed to be shallow (R >>h), z/R is small compared to unity. Thus, we may neglect the z/R terms in eqs. (2.32). Equations (2.22) in (2.33) in conjunction with eq. (2.34), yield,

$$\begin{aligned} \varepsilon_x &= \varepsilon_x^{\circ} + z\kappa_x \\ \varepsilon_s &= \varepsilon_s^{\circ} + z\kappa_s \\ \gamma_{xs} &= \gamma_{xs}^{\circ} + z\kappa_{xs} \end{aligned} \tag{2.35}$$

where [ε°] and [K] are the mid-surface strains and curvatures, respectively, defined as [6],

$$\begin{aligned} \varepsilon_x^{\circ} &= \frac{\partial u_0}{\partial x}, \quad \varepsilon_s^{\circ} = \frac{\partial v_0}{\partial s} + \frac{w}{R}, \quad \gamma_{xs}^{\circ} = \frac{\partial u_0}{\partial s} + \frac{\partial v_0}{\partial x} \\ \kappa_x &= \frac{\partial \psi_x}{\partial x}, \quad \kappa_s = \frac{\partial \psi_s}{\partial s}, \quad \kappa_{xs} = \frac{\partial \psi_x}{\partial s} + \frac{\partial \psi_s}{\partial x}, \end{aligned} \tag{2.36}$$

In addition, the interlaminar shear strains are given by [6]

$$\begin{aligned} \gamma_{xz} &= \psi_x + \frac{\partial w}{\partial x} \\ \gamma_{sz} &= \psi_s + \frac{\partial w}{\partial s} - \frac{v}{R} \end{aligned} \tag{2.37}$$

It is noted that these results are of exactly the same form as for flat, laminated plates of rectangular cross-section with the exception of the w/R term appearing in the expression for the mid-surface tangential strain ε_s° and the –v/R term in the expression for the interlaminar shear strain γ_{xz}, eq. (2.27). Since the analysis assumes that displacements u,

v, and w are small compared to the plate thickness h, and the radius of the shell R is much larger than h, the additional terms w/R and –v/R in eqs. (2.33) and (2.37) drop out.

The force and moment resultants [N] and [M] for the shell are [6],

$$(N_x, N_s, N_{xs}) = \int_{-h/2}^{h/2} (\sigma_x^{(k)}, \sigma_s^{(k)}, \tau_{xs}^{(k)})\, dz$$
$$(M_x, M_s, M_{xs}) = \int_{-h/2}^{h/2} (\sigma_x^{(k)}, \sigma_s^{(k)}, \tau_{xs}^{(k)})\, z\, dz \tag{2.38}$$

where $\sigma_x^{(k)}$, $\sigma_s^{(k)}$, and $\tau_{xs}^{(k)}$ are the in-plane stresses in the k^{th} ply. Integration yields the constitutive equations for extension and bending of a laminated cylindrical shell [6],

$$\begin{bmatrix} N \\ M \end{bmatrix} = \begin{bmatrix} A & B \\ B & D \end{bmatrix} \begin{bmatrix} \varepsilon^0 \\ \kappa \end{bmatrix} \tag{2.39}$$

where [A], [B], and [D] are the extensional, coupling and bending stiffness matrices, respectively, defined in eqs. (2.19) to (2.21). Inversion of this relation yields,

$$\begin{bmatrix} \varepsilon^\circ \\ K \end{bmatrix} = \begin{bmatrix} a & b \\ c & d \end{bmatrix} \begin{bmatrix} N \\ M \end{bmatrix} \tag{2.40}$$

where the compliance matrices [a], [b], [c], and [d] are defined as [7],

$$[a] = [A]^{-1} + [A]^{-1}[B]([D]-[B][A]^{-1}[B])^{-1}[B][A]^{-1}$$

$$[b] = -[A]^{-1}[B]([D]-[B][A]^{-1}[B])^{-1}$$

$$[c] = -([D]-[B][A]^{-1}[B])^{-1}[B][A]^{-1} \tag{2.41}$$

$$[d] = ([D]-[B][A]^{-1}[B])^{-1}$$

With the following definition of shear force resultants [6],

$$(Q_x, Q_s) = \int_{-h/2}^{h/2} (\tau_{xz}^{(k)}, \tau_{yz}^{(k)})\, dz \tag{2.42}$$

we obtain an additional constitutive relation involving transverse shear [6],

$$\begin{bmatrix} Q_s \\ Q_x \end{bmatrix} = k \begin{bmatrix} A_{44} & A_{45} \\ A_{45} & A_{55} \end{bmatrix} \begin{bmatrix} \gamma_{yz} \\ \gamma_{xz} \end{bmatrix} \tag{2.43}$$

where k is a shear correction factor [6] and A_{ij} are given by eq. (2.32).

2.5 Fracture Mechanics of Composite Materials

If composites are to be used to their fullest extent as engineering materials, it is necessary to know in advance their limits in load-bearing applications. This requires predictive techniques for the various failure modes that can occur in such applications. Fracture mechanics, the discipline concerned with failure by crack initiation and propagation, has been developed for this purpose. Fracture mechanics aims to predict the onset of fracture for a body containing a crack of a given size and geometry, and to

isolate material parameters of importance to crack resistance so that materials with improved fracture toughness can be devised [11].

Crack propagation can occur through three distinct fracture modes [12], as shown in Fig. 2.9. Normal stresses give rise to the mode I or "opening mode" where the displacements of the crack surfaces are perpendicular to the plane of the crack. In-plane shear results in mode II or "sliding mode"; the displacement of the crack surfaces is in the plane of the crack and perpendicular to the leading edge of the crack. The "tearing mode" or mode III is caused by transverse shear loading causing crack surface displacements in the plane of the crack and parallel to the leading edge of the crack. These modes are necessary and sufficient to describe all the possible combinations of loads and deformations in a cracked body.

For interlaminar fracture analysis of composites, it has become customary to use the strain energy release rate, G. The strain energy release rate, G, is a thermodynamic parameter that quantifies the energy available for crack growth. It is mathematically well defined as well as physically measurable in experiments [13]. The general expression for G is given by,

$$G = \frac{P^2}{2b}\frac{\partial C}{\partial a} \tag{2.44}$$

where b is the material thickness in the vicinity of the crack and $\partial C/\partial a$ is the change in the compliance C of the structure with crack length a. Since $\partial C/\partial a$ is a global property of a particular specimen, evaluation of G is independent of the detailed stress crack tip stress

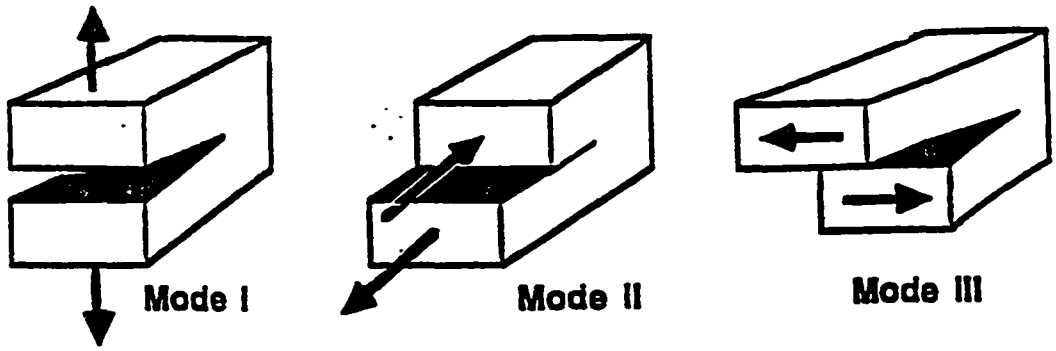

Fig. 2.9 The three basic modes of fracture.

distribution. Furthermore, $\partial C/\partial a$ and hence G can be determined from experiments by measuring compliance versus crack length for a structure. Therefore, difficulties encountered in analyzing the crack tip stresses are avoided. The critical value of $G = G_c$ is commonly denoted as the "interlaminar fracture toughness".

The analysis of delamination growth in filament wound cylinders is complicated by several aspects. A delamination in such a structure exists between angle-plies (e.g., $\pm\theta$) at a curved interface, while the overwhelming literature on delamination is limited to crack propagation in thin, flat unidirectional (0°) composites. A delamination between angle-plies has the feature of a crack between dissimilar anisotropic materials which complicates the fracture mechanics analysis and toughness characterization due to the possibility of oscillations of stresses and displacements near the crack tip, see Refs. [14-17]. In particular, the separation of the strain energy release rate, G, into individual components, G_I, G_{II}, and G_{III}, is impossible because the limit of the crack closure integral becomes undefined due to the oscillations of stresses and displacements near the tip. Similarly, the definition of stress intensity factors for the individual modes is associated with substantial difficulties. Schemes to suppress the influence of the oscillating singularity in the local analysis of crack tip fields have been suggested [18,19], although this issue is not fully resolved yet.

Another complication related to the established practice of using laminated beam fracture specimens for delamination characterization is that laminated beams containing off-axis plies typically possess elastic coupling phenomena such as bending/twisting and

bending/bending couplings [20,21]. Such couplings may complicate mechanical test procedures and may lead to a nonuniform distribution of energy release rate along the delamination front resulting in skewed and curved crack fronts when propagating an initially straight crack in a fracture test, Fig. 2.10 [20,21]. This in turn may lead to error in the evaluation of fracture toughness based on analysis assuming a uniform crack extension across the specimen width and assumption of a fracture mode from global considerations. The distributions of strain energy release rate in double cantilever beam (DCB) and end-notched flexure (ENF) specimens have been investigated by a number of researchers [20-26]. They found that the energy release rate in a DCB specimen is maximum at the center and lowest at the edges, while in an ENF specimen the energy release rate is largest at the edges and least at the center. One reason for such variations is the anticlastic curvature of the sub-beams. To quantify the nonuniformity of energy release rate along the crack front in flat delamination specimens, Davidson and Schapery [20] introduced a non-dimensional parameter, d_c, defined as,

$$d_c = D_{12}^2/(D_{11}D_{22}) \tag{2.45}$$

where D_{12}, D_{11}, and D_{22} are elements of the bending stiffness (D) matrix [7] for the sub-beams of the cracked region of the specimen. The difference between the maximum and minimum energy release rate in DCB and ENF specimens was found to scale in proportion to d_c.

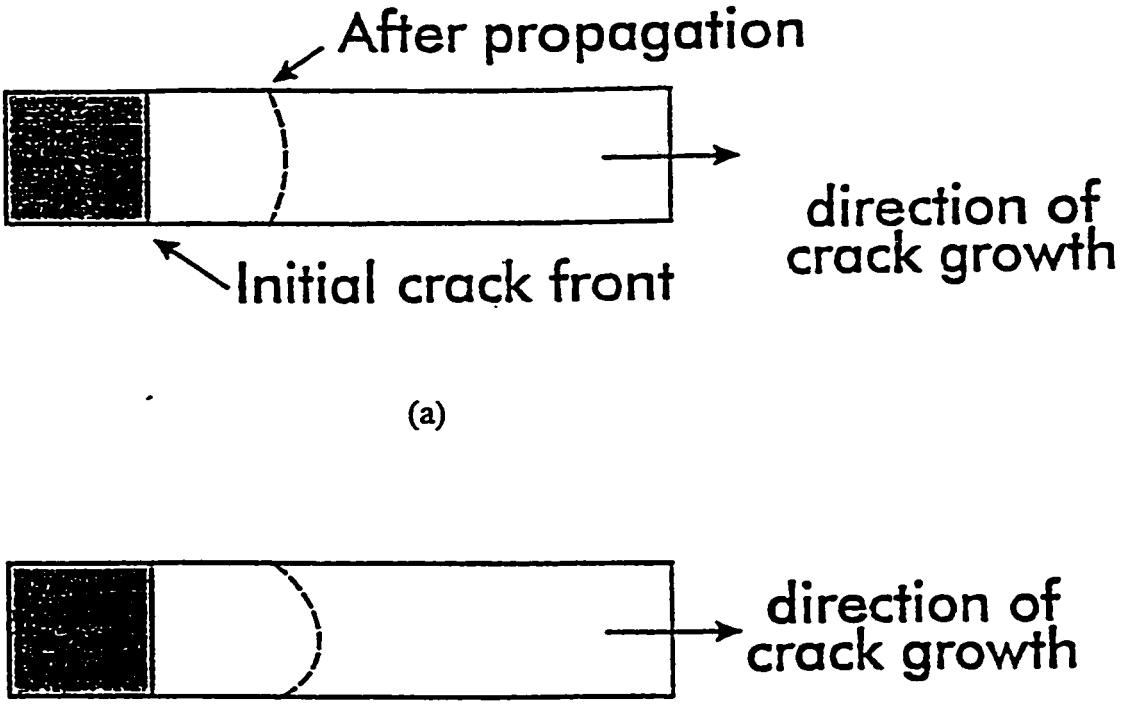

Fig. 2.10 Nonuniform delamination crack fronts in angle-ply laminated beams, a) curved, b) skewed.

For specially orthotropic composites such as cross-ply and unidirectional laminates, the distribution of energy release rate at the crack front is symmetric with respect to the specimen's longitudinal axis, similar to that in an isotropic specimen. For angle-ply laminates, however, even if they are symmetric and balanced, the energy release rate distribution across the width may be asymmetric or skewed [21,36]. Sun and Zheng [21] showed that the degree of skewness depends on the lay-up sequence and scales with the parameter s defined as,

$$s = D_{16}/D_{11} \tag{2.46}$$

where D_{16} is the i=1, j=6 element of the bending stiffness matrix for the sub-laminates of the cracked region [7]. Figure 2.11 shows symmetric (s=0) and skewed ($s \neq 0$) distributions of energy release rate for a DCB specimen [21]. If lay-up sequences are chosen to minimize either of d_c and s, then the other parameter increases [26].

In addition to crack front variations, a non-uniform G distribution indicates mixed mode effects. For the multidirectional laminate ENF specimens considered by Davidson et al. [26], the overall fracture mode ratio, G_{II}/G, was 0.92 at $d_c = 0.25$, and G_{III}/G was 0.08. Davidson et al. [26] suggested a limiting value of $d_c = 0.25$ below which the fracture toughness results from multidirectional DCB or ENF tests may be interpreted as "pure" mode I or mode II toughnesses. Furthermore, asymmetry in lay-up and specimen geometry with respect to the crack interface is common which may further induce mixed mode effects [27,28] and release of residual thermal stresses upon crack propagation.

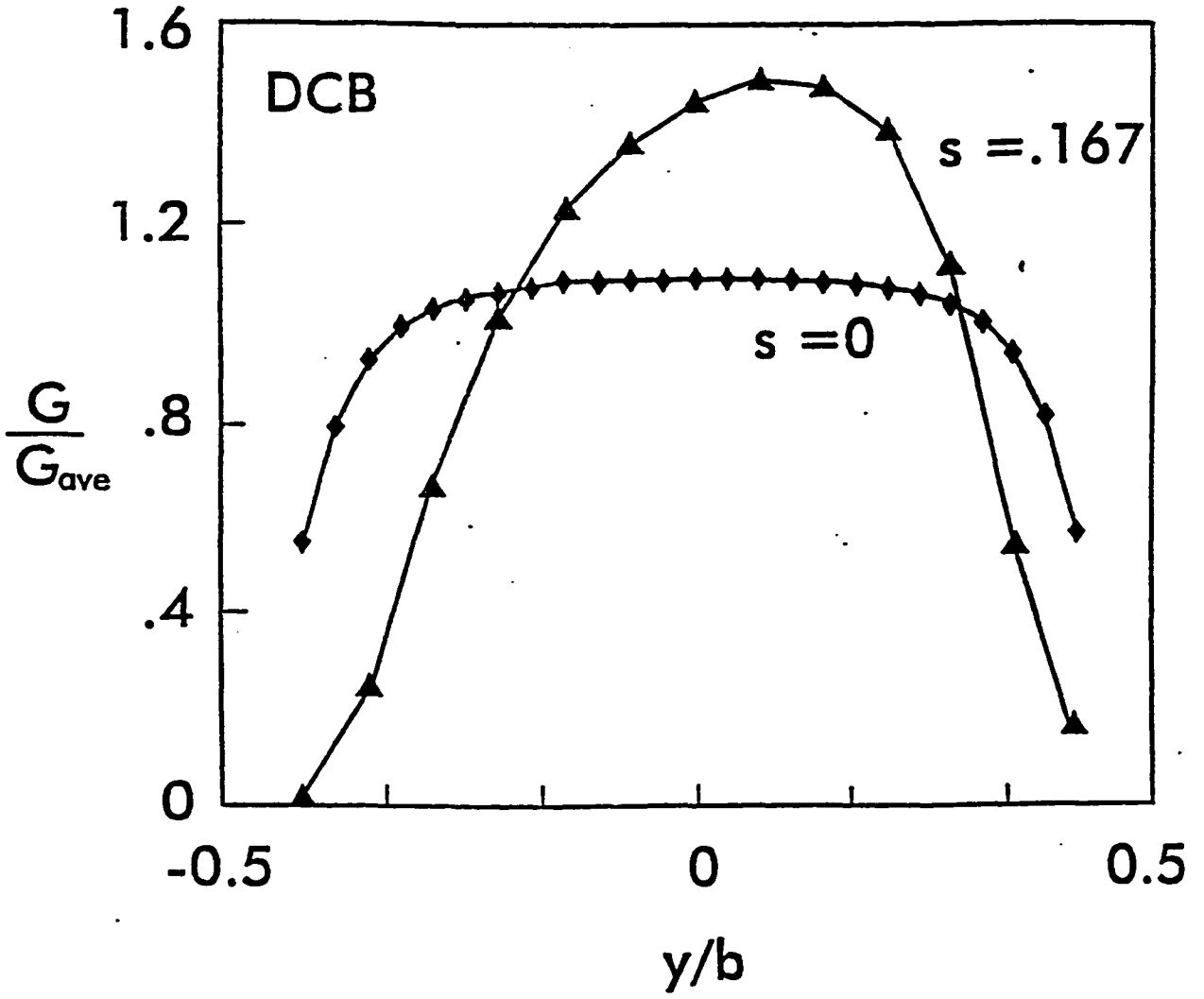

Fig. 2.11 Symmetric (s=0) and skewed (s≠0) distribution of energy release rate for a DCB specimen [21].

Despite these difficulties, beam fracture specimens cut from a composite structure are in many cases the only viable and appropriate choice for evaluation of the in-situ delamination of laminated composites. The current analysis and data reduction methodology for fracture toughness evaluation of beam fracture specimens, however, considers thin, unidirectional, high-modulus fiber composites. Because naval composites are commonly based on glass fibers, contain off-axis plies, may be thick and unsymmetric, and may have curved crack interfaces (in the case of specimens cut from cylinders) the fracture toughness reduced from current analysis methods is apparent and expected to be influenced by several factors that are not properly accounted for.

Delamination characterization of marine composite structures has not received much consideration although some appropriate related studies have been presented. Todero et al. [29] present experimental and finite element results for thick composites and demonstrated that the experimentally measured compliance of the thick specimens did not follow simple beam theory predictions although more refined finite element analysis also disagreed with experiments. Prel et al. [30] studied moderately thick, flat unidirectional composites (up to 20 mm thick) and found small effects of thickness on fracture toughness.

Nicholls and Gallagher [31] studied mode I crack growth using DCB specimens in graphite/epoxy (AS1/3502) laminates of the type $[\pm\theta/0_8/\pm\theta]_s$, with θ ranging from 0° to 90°. In all off-axis laminates, the crack initially deviated from the specimen mid-plane at the $-\theta/-\theta$ interface breaking through an off-axis ply. The apparent fracture toughness,

G_{IC}, was large and increased with increasing ply angle. In the 45° and 60° laminates crack branching was frequently observed. For ply angles of 60° and 90°, crack propagation was usually unstable. Chai [32] studied mode I delamination crack growth at different interfaces in thick laminates $[\pm 45/0_2/\pm 45/0_2/\pm 0/90]_{2S}$. The tests were performed on one brittle epoxy system and one medium tough epoxy. When regions with fiber breakage, fiber pull-out and shift of crack plane were excluded, G_{Ic} was of similar magnitude for 0°/0°, 0°/45°, 45°/-45° and 0°/90° interfaces. Laksimi et al. [33] examined DCB specimens with 0°/0°, 0°/90° and 90°/90° interfaces. Initiation G_{Ic} values for the 90°/90° and 0°/90° specimens were 26% and 40% larger than for the unidirectional specimen, and propagation values were roughly doubled. Robinson and Song [34] devised a modified DCB specimen for mode I fracture testing of multidirectional laminates. They proposed a novel technique of placing insert films at the intended crack interface along the edges of the specimen to suppress the crack jumping and fiber bridging observed in conventionally prepared DCB specimens. It was found that the apparent G_{Ic} value was significantly larger for 45°/45° and 45°/-45° interfaces than for the 0°/0° interface.

Chapter 3 ANALYSIS

Fracture mechanics analysis methods will be developed for delamination specimens machined from flat angle-ply laminate panels and filament wound composite cylinders, Fig. 3.1. Delamination propagation generally occurs as a result of mode I, mode II, and mode III loadings, or combinations thereof (mixed mode), Fig. 2.9. In this study, delamination fracture characterization in mode I, mode II, and mixed mode (I+II) will be examined using the DCB, ENF, and MMB test principles schematically shown in Fig. 1.2. The DCB specimen, Fig. 1.2a, has recently been accepted as an ASTM standard (ASTM D5528) for mode I characterization of unidirectional, high modulus fiber composites. The ENF specimen, Fig. 1.2b, for characterizing mode II crack propagation in unidirectional laminates is currently being considered for standardization by several international standard issuing organizations. The MMB test introduced by Reeder and Crews [35], Fig. 1.2c, was developed for characterization of delamination under mixed mode loading, and is also considered for standardization.

3.1 Bending Analysis of Flat Angle-Ply Laminate Beam Specimens

Analysis of flat DCB, ENF and MMB laminate beam fracture specimens with rectangular cross-section is presented. We will particularly consider $[\pm\theta]_n$ angle-ply

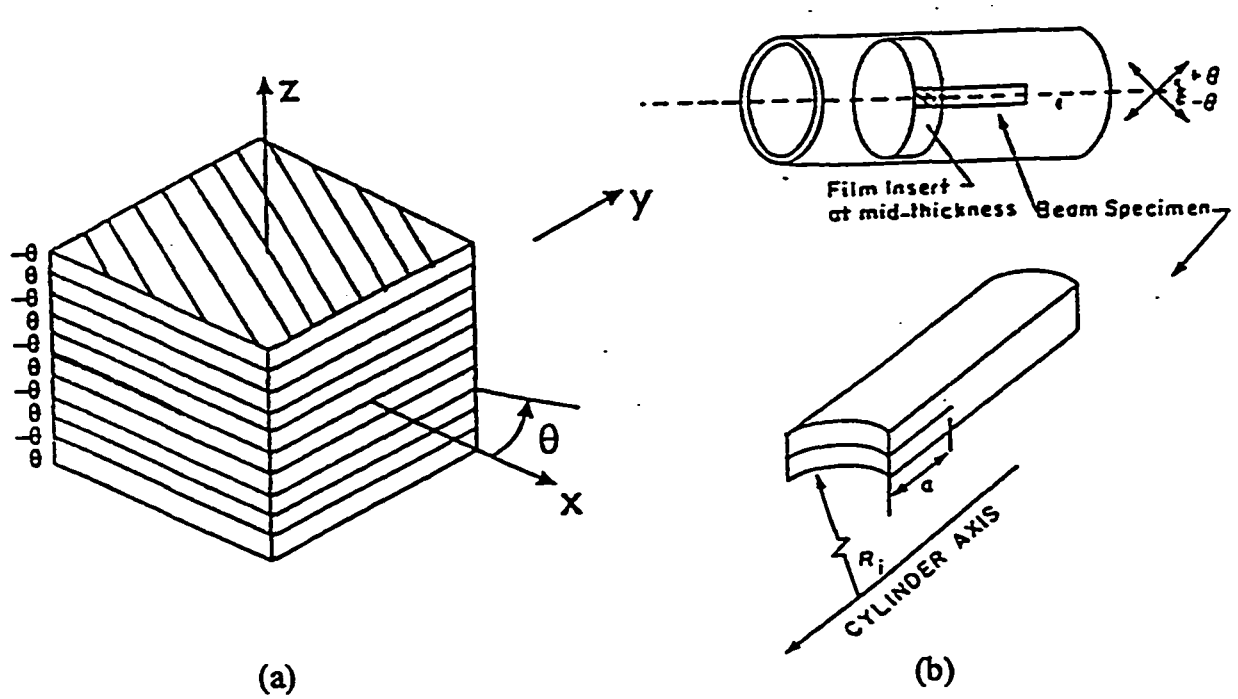

Fig. 3.1 Delamination specimens machined from a)flat angle-ply laminate panels and b) filament wound composite cylinders.

laminates with a delamination at the laminate mid-plane, but the analysis may be extended to more general lay-ups and delamination locations. The particular flat laminate considered in the experiments, Chapter 4, have n = 5. For a $[\pm\theta]_5$ laminate, Fig. 3.2, the beams of the delaminated region have [θ/-θ/θ/-θ/θ] and [-θ/θ/-θ/θ/-θ] lay-ups. Examination of the laminate [A], [B], and [D] stiffness matrices, eqs. (2.22), reveals the following:

Full laminate: $A_{16} = A_{26} = D_{16} = D_{26} = 0, B_{16} \neq 0, B_{26} \neq 0$

Sublaminates: $B_{ij} = 0, A_{16} \neq 0, A_{26} \neq 0, D_{16} \neq 0, D_{26} \neq 0$

The full laminate is unsymmetric while the laminates of the delaminated region are symmetric. The full laminate, furthermore, is balanced, while the sublaminates are unbalanced. It is also noted that the extension/shear coupling terms A_{16} and A_{26} are of equal magnitude, but of opposite signs for the two sub-laminates in the delaminated region. In a general situation where such specimens are tested at a temperature different than the cure temperature, there would be energy release associated with the release of residual thermal stresses during crack extension. For the room temperature cured laminates considered herein, however, this is not an issue.

The implications of the non-zero coupling terms on the response of the beam fracture specimens may be examined using the laminate constitutive equations given in eq. (2.22), Chapter 2. Considering the arms of the DCB specimen, Fig. 1.2a, as loaded by bending moments of opposite signs, it is recognized that the arms would experience twisting ($K_{xy} \neq 0$) in the same amount and direction due to the equal magnitude but opposite sign of D_{16} for the laminates above and below the mid-plane, Fig. 2.6. For the

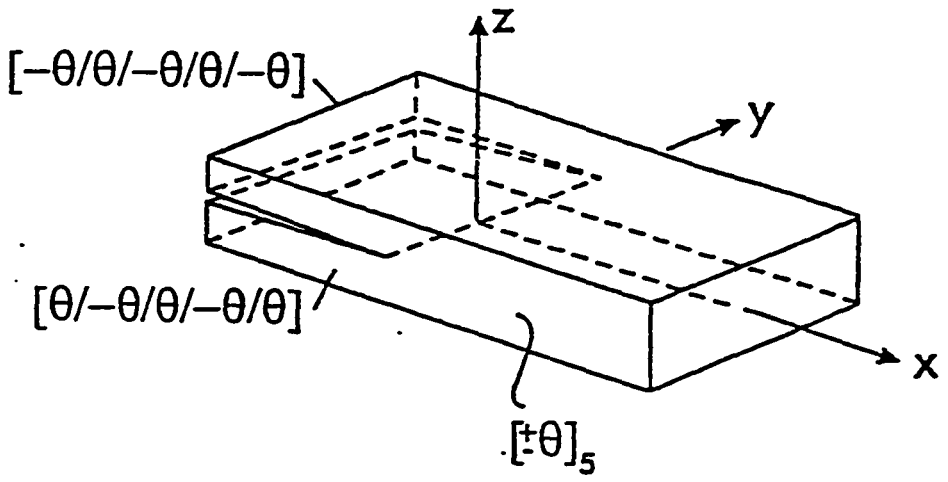

Fig. 3.2 Schematic of a flat $[\pm\theta]_5$ laminate.

ENF specimen, Fig. 1.2b, application of bending moment M_x to the full laminate would lead to in-plane shear deformation due to B_{16}, Fig. 2.6. Furthermore, the sub-laminates would experience twisting ($K_{xy} \neq 0$) in opposite directions due to opposite sign of D_{16} for the laminates above and below the mid-plane and anticlastic bending due to the D_{12} terms, Fig. 2.6. Such couplings for the sub-laminates may lead to nonuniform crack growth and mixed mode effects as discussed in Chapter 1, see also Refs. [27,28].

In this Chapter, we will focus on analysis of flat, angle-ply laminate DCB, ENF and MMB beam specimens with rectangular cross-section machined from angle-ply composite panels. The beam displacements will be used to calculate the compliance and energy release rate of the beam fracture specimens.

3.1.1 Bending Analysis of Flat Angle-Ply Laminate DCB Specimen

Figure 3.3 shows the geometry of the DCB specimen with a delamination at the laminate mid-plane. In elementary beam theory analysis of the DCB specimen [36], each arm of the specimen is considered as rigidly built-in in the uncracked region of the beam, and thus assumes zero slope and displacement at the beam root (crack tip) and ignores the remainder of the specimen in the analysis. In reality, however, as first recognized by Kanninen [37,38], the two arms of the specimen rotate slightly due to the elastic support provided at the crack tip. Following Kanninen's original work for isotropic DCB specimens, we will here develop a foundation model for the angle-ply laminate DCB specimen considered. The elastic foundation model of a mid-plane symmetric DCB specimen is illustrated in Fig. 3.4. The cracked region is considered as a free beam of

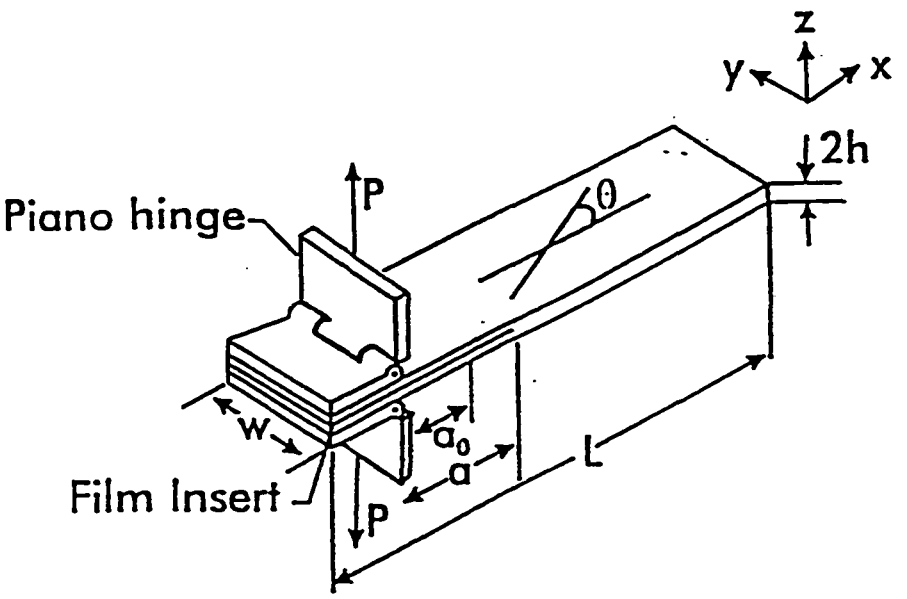

Fig. 3.3 Geometry, coordinate system and test configuration of angle-ply laminate DCB specimen.

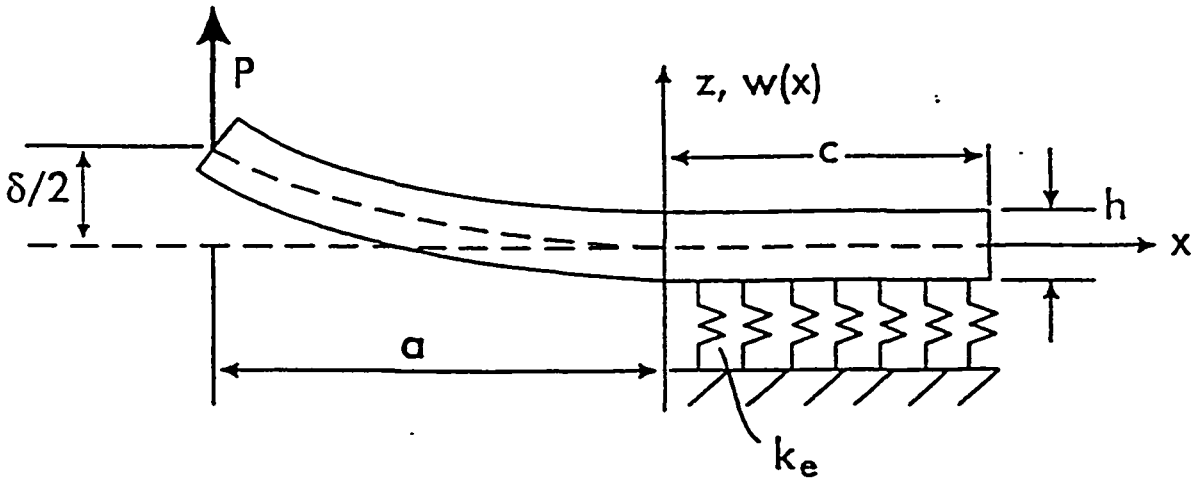

Fig. 3.4 Elastic foundation model of a mid-plane symmetric DCB specimen.

length "a" loaded with a concentrated load P at one end. The uncracked section beyond the crack tip is modeled as a beam on a Winkler elastic foundation [39], with extensional modulus k_e.

The mathematical description of the DCB specimen shown in Fig. 3.4 is based upon the Euler-Bernoulli beam theory and the Winkler foundation analysis of Kanninen [37] here modified for angle-ply laminates according to the laminated beam theory formulation of Whitney [6] and a laminate homogenization method of Hyer and Knott [40] summarized in Appendix A. The governing differential equation for the deflection w(x) of the laminate beam, Fig. 3.4, may be written:

$$\frac{d^4 w(x)}{dx^4} + 4\lambda^4 H(x)\, w(x) = 0 \tag{3.1a}$$

where

$$H(x) = \begin{cases} 1 & x > 0 \\ 0 & x < 0 \end{cases} \tag{3.1b}$$

and

$$\lambda^4 = \frac{3 k_e}{E_x b\, h^3} \tag{3.1c}$$

in which k_e is the foundation modulus and E_x is the effective bending modulus of the laminate. E_x is obtained from eqs. (2.40),

$$E_x = \frac{12}{d_{11} h^3} \tag{3.2}$$

where d_{11} is the i = j = 1 element of the bending compliance matrix given in eqs. (2.41). The Winkler model assumes the reaction forces of the elastic foundation to be proportional to the beam deflection at any point. Since the elastic foundation incorporates the elasticity of the uncracked part of the DCB specimen, the foundation modulus may be related to the out-of-plane extensional stiffness (E_z) of the laminate. Following Ref. [37] and from Fig. 3.4, the average thickness stretch in the region beyond the crack tip is,

$$\varepsilon_z = \frac{w(x)}{h/2} \tag{3.3}$$

where w(x) is the beam deflection in the uncracked region ($x \geq 0$) and h is the semi-thickness of the DCB specimen. Hooke's law yields,

$$\sigma_z = E_z \varepsilon_z \tag{3.4}$$

But k_e is defined as [37],

$$k_e = \frac{b\sigma_z(x)}{w(x)} \tag{3.5}$$

Equations (3.4) and (3.5) combined yield,

$$k_e = \frac{2\,b\,E_z}{h} \tag{3.6}$$

Then, from eq. (3.1c),

$$\lambda = \frac{6^{\frac{1}{4}}}{h}\left(\frac{E_z}{E_x}\right)^{\frac{1}{4}} \tag{3.7}$$

The modulus E_z, required for calculation of λ, is estimated using the laminate homogenization method of Hyer and Knott [40] summarized in Appendix A.

The appropriate boundary conditions are those for a shear force P acting at the left beam end and a free end condition at the right-hand end, Fig. 3.4. Using the prime notation to indicate differentiation with respect to x, the boundary conditions can be written:

$$\begin{aligned} w'(-a) &= 0 \\ w'''(-a) &= \frac{12P}{E_x b h^3} \\ w'(c) &= w'''(c) = 0 \end{aligned} \tag{3.8}$$

The solution to eq. (3.1a) satisfying these conditions is obtained by considering the intervals (-a,0) and (0,c) (Fig. 3.4) separately, then matching the values of the deflection and its first three derivatives at x = 0 [37]. The result for the laminate beam is,

$$w(x) = \frac{6P}{E_x b h^3 \lambda^3} \begin{cases} \frac{\lambda^3 x^3}{3} + a\lambda^3 x^2 - A\lambda x + B & -a \le x \le 0 \\ a\lambda \sin\lambda x \sinh\lambda x - \left(\frac{A-1}{2}\right)\sin\lambda x \cosh\lambda x & \\ + B\cos\lambda x \cosh\lambda x - \left(\frac{A+1}{2}\right)\cos\lambda x \sinh\lambda x & 0 \le x \le c \end{cases} \tag{3.9a}$$

where

$$A = \left[\frac{\sinh^2\lambda c + \sin^2\lambda c}{\sinh^2\lambda c - \sin^2\lambda c}\right] + 2a\lambda\left[\frac{\sinh\lambda c\cosh\lambda c + \sin\lambda c\cos\lambda c}{\sinh^2\lambda c - \sin^2\lambda c}\right] \tag{3.9b}$$

$$B = \left[\frac{\sinh\lambda c\ \cosh\lambda c - \sin\lambda c\ \cos\lambda c}{\sinh^2\lambda c - \sin^2\lambda c}\right] + a\lambda\left[\frac{\sinh^2\lambda c + \sin^2\lambda c}{\sinh^2\lambda c - \sin^2\lambda c}\right] \tag{3.9c}$$

Since the deflection of each arm at the point of load application is $\delta/2 = w(-a)$, the DCB specimen compliance $C = \delta/P$ can be written:

$$C = \frac{4}{E_x b h^3 \lambda^3}\left[2\lambda^3 a^3 + 6\lambda^2 a^2 \frac{(\sinh \lambda c \cosh \lambda c + \sin \lambda c \cos \lambda c)}{\sinh^2 \lambda c - \sin^2 \lambda c}\right.$$
$$\left. + 6\lambda a \frac{(\sinh^2 \lambda c + \sin^2 \lambda c)}{\sinh^2 \lambda c - \sin^2 \lambda c} + 3\frac{(\sin h\lambda c \cosh \lambda c - \sin \lambda c \cos \lambda c)}{\sinh^2 \lambda c - \sin^2 \lambda c}\right] \tag{3.10}$$

After substitution of the expression for λ into the compliance expression, eq. (3.10), and considering that the length of the undelaminated region, c, is much larger than the beam thickness for commonly used DCB specimens, it is recognized that the hyperbolic sine and cosine functions in eq. (3.10), will dominate leading to substantial simplification of eq. (3.10),

$$C = \frac{8}{E_x b}\left(\frac{a}{h}\right)^3\left[1 + 1.92\left(\frac{h}{a}\right)\left(\frac{E_x}{E_z}\right)^{1/4} + 1.22\left(\frac{h}{a}\right)^2\left(\frac{E_x}{E_z}\right)^{1/2} + 0.39\left(\frac{h}{a}\right)^3\left(\frac{E_x}{E_z}\right)^{3/4}\right] \tag{3.11}$$

The strain energy release rate, G, available for propagating the crack, is obtained using eq. (2.44) with eq. (3.11) yielding,

$$G = \frac{12P^2a^2}{E_x b^2 h^3}\left[1 + 1.28\left(\frac{h}{a}\right)\left(\frac{E_x}{E_z}\right)^{1/4} + 0.41\left(\frac{h}{a}\right)^2\left(\frac{E_x}{E_z}\right)^{1/2}\right] \tag{3.12}$$

The first term on the right-hand side of eq. (3.12) is identified as the energy release rate expression for a DCB specimen given by classical beam theory [41]. This expression is

strictly valid only for infinitely long crack lengths. The term inside the parenthesis is the elastic foundation correction factor for an angle-ply laminate that accounts for the finite crack length by incorporating the transverse elasticity of the uncracked region of the specimen. Equation (3.12) indicates that the energy release rate increases with increasing modulus ratio E_x/E_z and thickness-to-crack length ratio h/a.

The one-dimensional beam analysis presented here may be applied for prediction of compliance and overall energy release rate of laminated DCB specimens, but does not provide local mode mixity at the crack front. A three-dimensional finite element analysis of laminate DCB specimens with anti-symmetric lay-ups (full laminate), similar to those considered herein, indicates that the mode II and mode III contributions to the total strain energy release rate are negligible (<1%) [25]. Therefore, the fracture toughness evaluated for the DCB specimens examined herein is expected to represent close to pure mode I conditions at the crack front.

3.1.2 Bending Analysis of Flat Angle-Ply Laminate ENF Specimen

Figure 3.5 shows the geometry of the angle-ply laminate ENF specimen with a delamination at the mid-plane. To analyze the laminated ENF specimen, the compliance form of the laminate constitutive relation, eq. (2.40), is most convenient,

$$\begin{bmatrix} \varepsilon^{\circ} \\ K \end{bmatrix} = \begin{bmatrix} a & b \\ c & d \end{bmatrix} \begin{bmatrix} N \\ M \end{bmatrix} \tag{3.13}$$

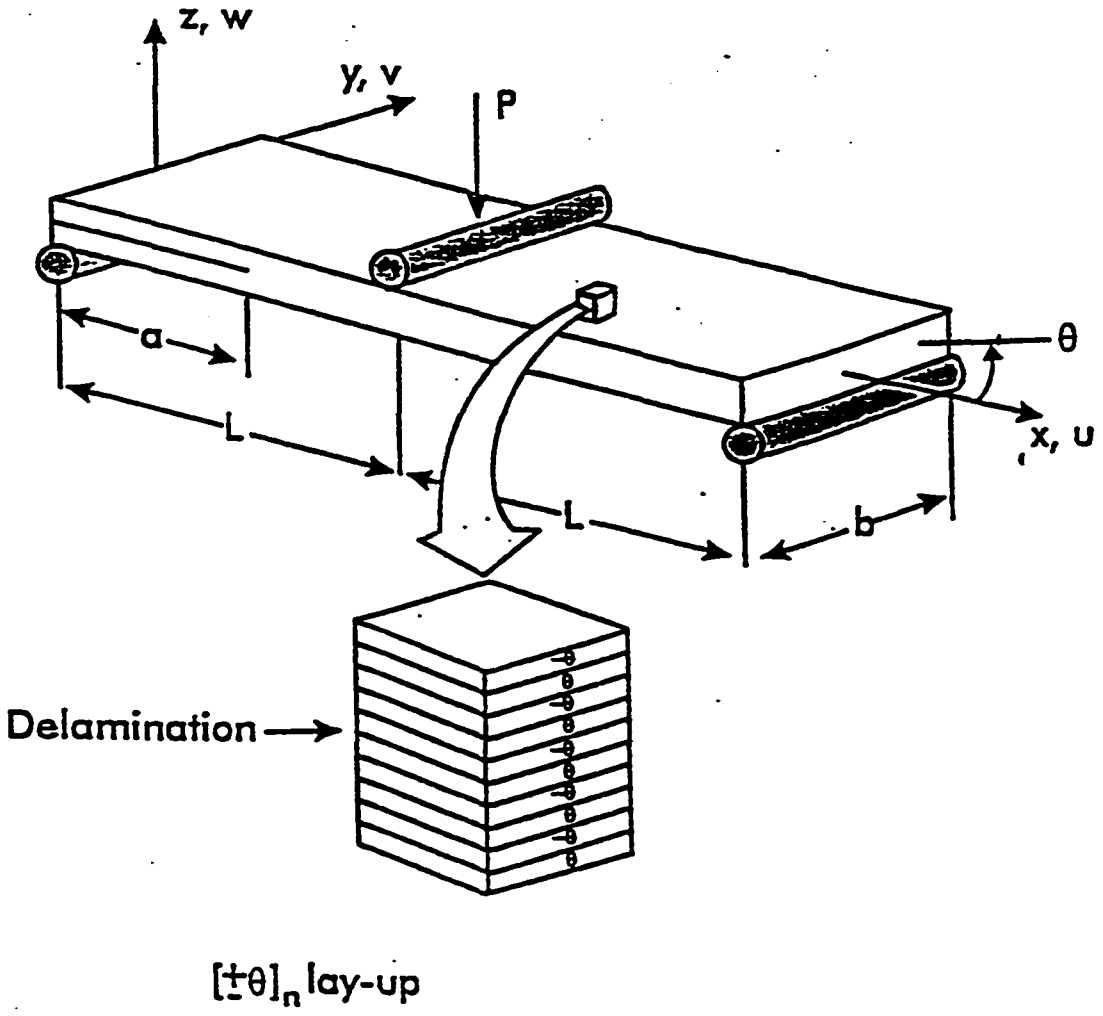

Fig. 3.5 Geometry, coordinate system, and test configuration of angle-ply laminate ENF specimen.

where expressions for the matrices [a], [b], [c], [d] are given in eqs. (2.41). The angle-ply laminate ENF specimen will be approached by a first order shear deformation beam theory [6] previously used to model sandwich beams [42].

With the coordinate system shown in Fig. 3.6 and [N] = [0] and $M_y = M_{xy} = 0$, eq. (3.13), yields,

$$K_x = d_{11} M_x \tag{3.14}$$

where d_{11} is given by eq. (2.41). In a beam theory formulation incorporating shear deformation the following displacements are assumed [6],

$$u(x,z) = u_0(x) + z\varphi_x(x) \tag{3.15a}$$

$$w(x) = w_0(x) \tag{3.15b}$$

where u and w are the displacement components in the x and z directions, u_0 and w_0 are the x and z displacement components of the mid-surface, and φ_x is the rotation of a beam cross-section at position x, Fig. 2.7. The curvature K_x in eq. (3.14) is given from eq. (2.26),

$$K_x = \frac{d\varphi_x}{dx} \tag{3.16}$$

The compliance form of laminate constitutive relation including transverse shear, eq. (2.31), is,

$$\begin{bmatrix} \gamma_{yz} \\ \gamma_{xz} \end{bmatrix} = \frac{1}{k} \begin{bmatrix} a_{44} & a_{45} \\ a_{45} & a_{55} \end{bmatrix} \begin{bmatrix} Q_y \\ Q_x \end{bmatrix} \tag{3.17}$$

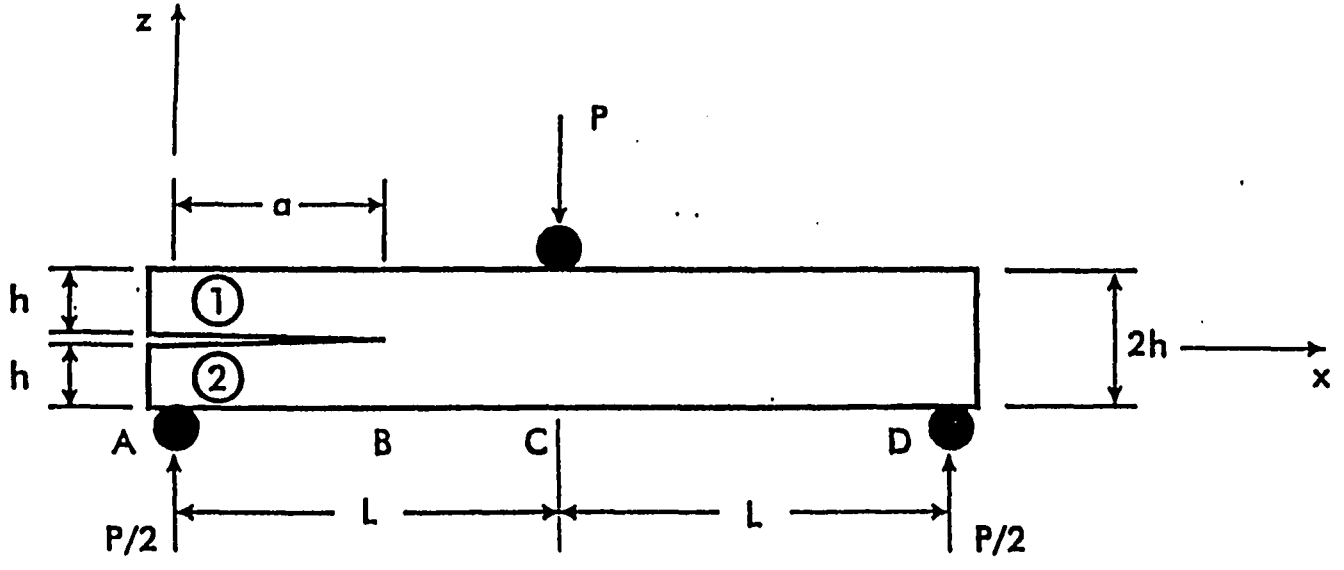

Fig. 3.6 Definition of delaminated (A-B) and intact (B-C-D) sections of the ENF specimen. 1 and 2 denote upper and lower sub-beams of the delaminated region.

where Q_x and Q_y are the shear stress resultants, Fig. 2.4, k is a shear correction factor [6,43], a_{ij} (i,j = 4,5) are the shear compliances, and γ_{yz} and γ_{xz} are the interlaminar shear strains, with γ_{xz} given by,

$$\gamma_{xz} = \psi_x + \frac{dw}{dx} \tag{3.18}$$

The equilibrium equation involving moment resultants M_y and M_{xy} and shear stress resultant Q_y [28] yields with $M_y = M_{xy} = 0$; $Q_y = 0$. Substitution of $M_{xy} = 0$ and Q_x given by eq. (3.17) (with $Q_y = 0$) into eq. (3.16) yields, in combination with the following equilibrium equation [6],

$$\frac{\partial M_x}{\partial x} + \frac{\partial M_{xy}}{\partial y} + Q_x = 0 \tag{3.19}$$

the following differential equation for the beam deflection,

$$\frac{dw}{dx} = -\psi_x + \frac{a_{55}}{k}\frac{dM_x}{dx} \tag{3.20}$$

Solution of the deflection for the actual angle-ply laminate ENF beam specimen requires the moment distribution along the beam for the three-point flexure loading, Fig. 3.5,

$$M_x = \frac{Px}{2b} \qquad 0 \le x \le L \tag{3.21a}$$

$$M_x = \frac{Px}{2b} \; \frac{PL}{b} \qquad L \le x \le 2L \tag{3.21b}$$

where b is the width of the beam. Solutions for each of the regions AB, BC and CD of the beam, Fig. 3.6, are then sought. The delaminated region AB of the beam is considered as a beam with effective bending and shear properties to be determined below. Regions BC and CD both have properties of the full laminate. A differential equation for

φ_x for each region of the beam is achieved by combination of eqs. (3.14), (3.16), (3.20) and (3.21). Integration of eq. (3.16) yields φ_x which is substituted into eq. (3.20). Further integration yields the vertical displacement, w, of the beam, and the axial displacement, u, is obtained from eq. (3.15a). Continuity in axial displacement across the interface of each subsection, along with continuity in vertical displacement at x = a and x = L with the requirements w(0) = w(2L) = 0 yields expressions for w(x) for each subsection of the ENF geometry. The vertical displacement at the point of load application, w(L), is given by,

$$w(L) = -\frac{PL^3(d_{11})_{BC}}{6b} - \frac{PL(a_{55})_{BC}}{2bk} - \frac{Pa^3\left[(d_{11})_{AB} - (d_{11})_{BC}\right]}{12b} - \frac{Pa\left[(a_{55})_{AB} - (a_{55})_{BC}\right]}{4bk} \tag{3.22}$$

The effective bending and shear compliances of the delaminated region AB are [42],

$$(d_{11})_{AB} = \frac{(d_{11})_2}{1 + (d_{11})_2/(d_{11})_1} \tag{3.23a}$$

$$(a_{55})_{AB} = \frac{(a_{55})_2}{1 + (a_{55})_2/(a_{55})_1} \tag{3.23b}$$

where subscripts 1 and 2 denote the upper and lower sub-laminates of the ENF specimen, Fig. 3.6. Due to the symmetry and similarity of the sub-laminates we have,

$$(d_{11})_1 = (d_{11})_2 = d_{11} \tag{3.24a}$$

$$(a_{55})_1 = (a_{55})_2 = a_{55} \tag{3.24b}$$

which shows that each sub-beam in the delaminated region carries equal load (P/4). Since each sub-laminate is symmetric, the coupling matrix [B] in eqs. (2.41) vanishes.

Therefore, the effective bending compliance element d_{11} for a sub-laminate is simply calculated from,

$$[d]=[D]^{-1} \tag{3.25}$$

where D_{ij} are defined in eq. (2.21). The shear compliance a_{55} is obtained from eqs. (2.30) and (3.17),

$$a_{55}=\frac{A_{44}}{A_{44}A_{55}-A_{45}^2} \tag{3.26}$$

where A_{ij} (i,j = 4,5) are given by eq. (2.32). Calculation of A_{ij} (i,j = 4,5) requires determination of shear stiffness terms C_{44} (= G_{13}) and C_{55} (= G_{23}), where G_{13} and G_{23} are the interlaminar shear moduli. Assumption of transverse isotropy in the 2-3 plane yields $G_{13} = G_{12}$ where G_{12} is the in-plane shear modulus conveniently measured in a standard material characterization test [44]. G_{23} can be estimated from the isotropic relation, $G_{23} = E_2/(2(1+\nu_{23}))$, where Poisson's ratio ν_{23} is assumed to be 0.3. For unidirectional laminates ($\theta = 0$), $C_{45} = 0$ which leads to $A_{45} = 0$. Hence the shear compliance a_{55} for a unidirectional laminate is simplified to: $a_{55} = 1/A_{55} = 1/(h_0 G_{13})$, where h_0 is the laminate ($h_0 = 2h$) or sub-laminate thickness ($h_0 = h$). Finally, the effective bending and shear compliances, $(d_{11})_{BC}$ and $(a_{55})_{BC}$, of the undelaminated region BC (full laminate) required for the calculation of the beam deflection, eq. (3.22), are calculated from eqs. (3.25) and (3.26), using eqs. (2.32) to obtain A_{ij}.

For purposes of subsequent fracture analysis and testing, we are interested in the compliance, C, of the beam defined as: $C = \delta/P$ where P is the applied load and δ is the associated deflection, $\delta = |w(L)|$. Equation (3.22) yields,

$$C = \frac{L^3 (d_{11})_{BC}}{6b} + \frac{L(a_{55})_{BC}}{2bk} + \frac{a^3 [(d_{11})_{AB} - (d_{11})_{BC}]}{12b} + \frac{a[(a_{55})_{AB} - (a_{55})_{BC}]}{4bk} \qquad (3.27)$$

Various values of the shear correction factor k have been used for homogeneous isotropic plates such as k = 5/6, $\pi^2/12$ and 2/3, see Whitney [6]. Comparison of exact solutions to the first order shear deformation theory provides a basis for determining k. For composite laminates, k depends on ply properties and stacking sequence. Detailed solutions by Whitney and Pagano [43] reveals that both k = 5/6 and 2/3 give good correlation with the exact theory. For the numerical results presented in this study we used k = 5/6.

The strain energy release rate, G, available for propagating the crack is obtained using eq. (2.44). Combination of eqs. (3.27) and (2.44) yields,

$$G = \frac{P^2}{8b^2} \left\{ a^2 [(d_{11})_{AB} - (d_{11})_{BC}] + \frac{(a_{55})_{AB} - (a_{55})_{BC}}{k} \right\} \qquad (3.28)$$

For unidirectional laminates, $(a_{55})_{AB} = (a_{55})_{BC}$, which in eq. (3.28) shows that the shear deformation contribution to the energy release rate vanishes. For angle-ply laminates, it may be shown that $(a_{55})_{AB} \approx (a_{55})_{BC}$, since A_{45} is small in comparison to A_{44} and A_{55}. Hence, according to this formulation, there is no or very small contribution from shear deformation to the energy release rate for unidirectional and angle-ply laminates with mid-plane cracks.

3.1.3 Bending Analysis of Flat Angle-Ply Laminate MMB Specimen

The MMB test introduced by Reeder and Crews [35], shown in Fig. 3.7, allows characterization of delamination initiation and propagation for a wide range of mixed mode ratios, G_I/G_{II}. The MMB loading can be represented by a superposition of mode I opening and mode II sliding, Fig. 2.9, equivalent to a combination of the DCB and ENF tests [35]. Thus, compliance and strain energy release rate equations from the DCB and ENF tests are combined to obtain the desired equations for the MMB test. Figure 3.8 shows a free body diagram for the MMB specimen and partition of the applied load P into mode I and mode II contributions [35]. According to Fig. 3.8 the mode I and mode II "components" of the applied load are,

$$P_I = \frac{(3c - L)P}{4L} \tag{3.29a}$$

$$P_{II} = \frac{(c + L)P}{L} \tag{3.29b}$$

Substitution of the loads P_I and P_{II} given by eq. (3.29) into the previously derived expressions for the strain energy release rate of angle-ply DCB and ENF laminate specimens, eqs. (3.12) and (3.28), gives the MMB energy release rate, $G = G_{DCB} + G_{ENF}$,

$$G = \left(\frac{P}{b}\right)^2 \left\{ \left(\frac{3c - L}{4L}\right)^2 \frac{12a^2}{E_x h^3} \left[1 + 1.28\left(\frac{h}{a}\right)\left(\frac{E_x}{E_z}\right)^{1/4} + 0.41\left(\frac{h}{a}\right)^2\left(\frac{E_x}{E_z}\right)^{1/2} \right] + \left(\frac{c + L}{L}\right)^2 \frac{a^2}{8}\left[(d_{11})_{AB} - (d_{11})_{BC}\right] \right\} \tag{3.30}$$

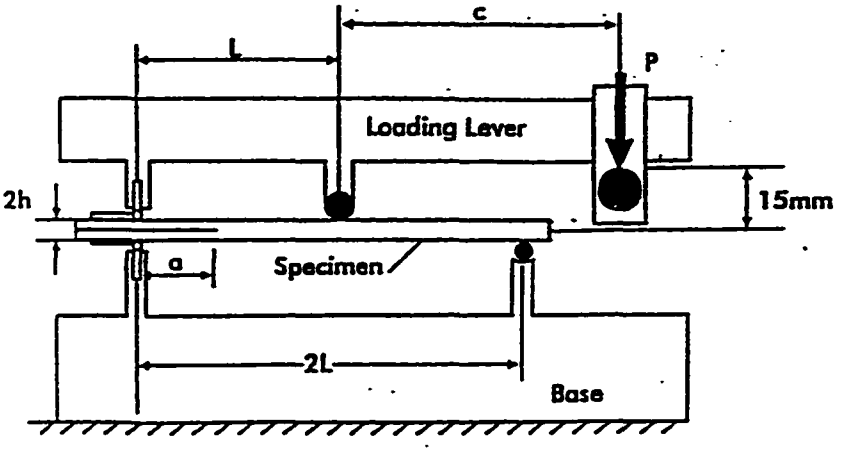

Fig. 3.7 MMB specimen and test principle [37].

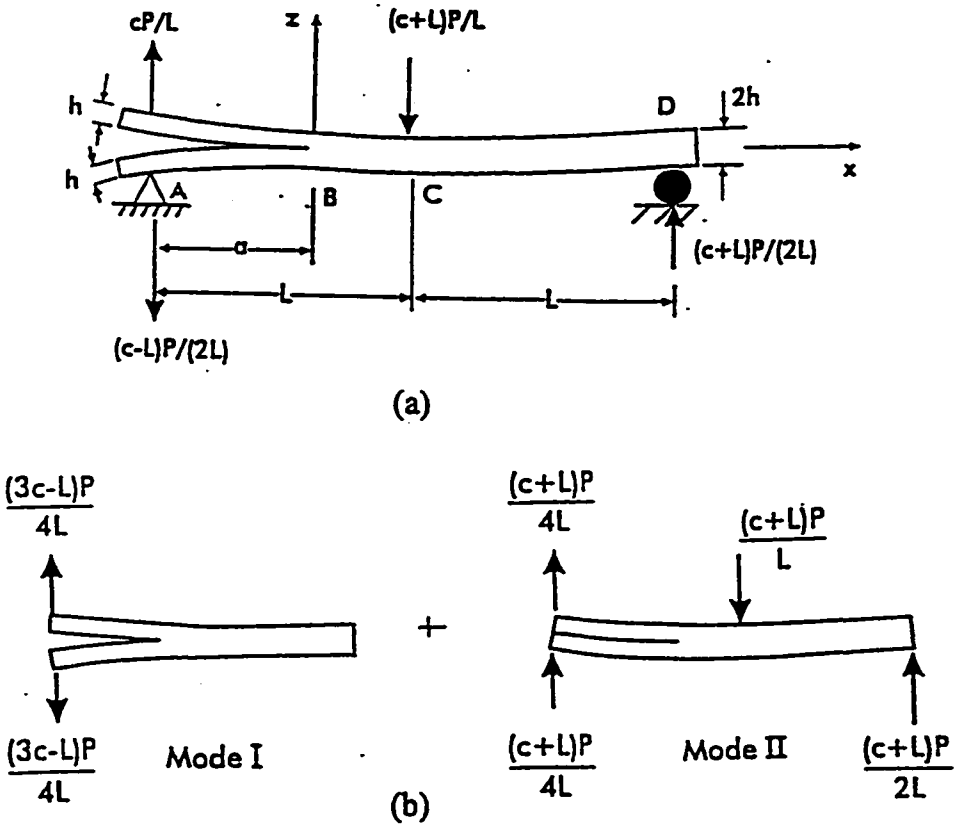

Fig. 3.8 Free-body diagram of a) MMB specimen loading and b) the partition of the applied load into mode I and mode II contributions [37].

From kinematics analysis of the deformation of the MMB test fixture and specimen, Figs. 3.7 and 3.8, the deflection δ at the load point can be expressed as,

$$\delta = \left(\frac{3c-L}{4L}\right)\delta_{DCB} + \left(\frac{c+L}{L}\right)\delta_{ENF} \tag{3.31}$$

DCB and ENF specimen compliances may be defined as,

$$C_{DCB} = \frac{\delta_{DCB}}{P_I} \tag{3.32a}$$

$$C_{ENF} = \frac{\delta_{ENF}}{P_{II}} \tag{3.32b}$$

where P_I and P_{II} are defined in eqs. (3.39). Substituting eqs. (3.32) and (3.29) in eq. (3.31) and dividing by the applied load P, the compliance of the MMB specimen, $C = \delta/P$, can be expressed as,

$$C = \left(\frac{3c-L}{4L}\right)^2 C_{DCB} + \left(1+\frac{c}{L}\right)^2 C_{ENF} \tag{3.33}$$

where expressions for C_{DCB} and C_{ENF} are given in eqs. (3.11) and (3.27). Substitution of these expressions into eq. (3.33) yields,

$$C = \left(\frac{3c-L}{4L}\right)^2 \left\{ \frac{8}{E_x b}\left(\frac{a}{h}\right)^3 \left[1 + 1.92\left(\frac{h}{a}\right)\left(\frac{E_x}{E_z}\right)^{1/4} + 1.22\left(\frac{h}{a}\right)^2\left(\frac{E_x}{E_z}\right)^{1/2} + 0.39\left(\frac{h}{a}\right)^3\left(\frac{E_x}{E_z}\right)^{3/4} \right] \right\}$$
$$+ \left(\frac{c+L}{L}\right)^2 \left\{ \frac{L^3 (d_{11})_{BC}}{6b} + \frac{L(a_{55})_{BC}}{2bk} + \frac{a^3\left[(d_{11})_{AB} - (d_{11})_{BC}\right]}{12b} \right\} \tag{3.34}$$

Equations (3.30) and (3.34) incorporate the influences of elastic foundation and transverse shear deformation. The fracture mode ratio, G_I/G_{II}, for the MMB test may be approximated as,

$$\frac{G_I}{G_{II}} = \frac{6\beta}{E_x h^3}\left(\frac{3c-L}{c+L}\right)^2 \qquad c \geq \frac{L}{3} \tag{3.35}$$

where

$$\beta = \frac{1+1.28\left(\frac{h}{a}\right)\left(\frac{E_x}{E_z}\right)^{1/4}+0.41\left(\frac{h}{a}\right)^2\left(\frac{E_x}{E_z}\right)^{1/2}}{(d_{11})_{AB}-(d_{11})_{BC}} \tag{3.36}$$

Examination of eq. (3.35) reveals that G_I/G_{II} is zero when c = L/3. For c < L/3 eq. (3.35) is invalid because of contact between the two arms of the specimen (G_I/G_{II} = 0 for c < L/3).

3.1.4 Comparison to Previous Analyses

Beam theory formulations developed above for bending analysis of flat unidirectional and angle-ply laminate beam specimens have been compared with previously models. It is interesting to note that the expression for the energy release rate, G, of flat, angle-ply laminate DCB specimen, eq. (3.12), has linear (h/a) and quadratic terms $(h/a)^2$ in agreement with the expression for G determined by orthotropy scaling of DCB specimens according to Suo et al. [45],

$$G = \frac{12 P^2 a^2}{E_1 b^2 h^3}\left[1 + 0.677\left(\frac{E_2}{E_1}\right)^{-1/4}\left(\frac{h}{a}\right)\right]^2 \tag{3.37}$$

The functional dependence of their scale factor, E_2/E_1, for orthotropy is in perfect agreement with the dependence of G on modulus ratio E_x/E_z in eq. (3.12) for a transversely isotropic composite ($E_x=E_1$ and $E_z=E_3=E_2$). The coefficients 1.28 and .41 are constants in eq. (3.12) but are dimensionless combinations of material parameters in the analysis of Suo et al. [45]. Their coefficients, however, do not show very large dependence of material anisotropy within reasonable practical limits. For the $[0]_6$ glass/polyester composite examined experimentally herein and for the range of crack lengths between 33 and 80 mm considered, the difference between the two expressions for G is less than 3%, see Fig. 3.9.

Compliance and energy release rate of the flat, angle-ply laminate ENF specimen predicted from the shear deformation laminated beam theory (SBT), eqs. (3.27) and (3.28), are compared with predictions from classical plate theory (CPT) analysis for specially orthotropic and symmetric laminate ENF specimens [26], see Appendix B. A parametric study was performed for a $[\pm 30]_n$ angle-ply laminate where n assumes odd numbers in the range from 3 to 11. Similar results are expected for $[\pm\theta]_n$ angle-ply laminates with different angles θ. In calculating the ENF compliance and energy release rate by the SBT and CPT approaches, the material properties in Table 3.1 were used along with the test configuration dimensions of L = 50 mm, b = 20 mm, a = 25 mm, and a ply thickness of 0.73 mm. The compliance calculated using SBT analysis was normalized

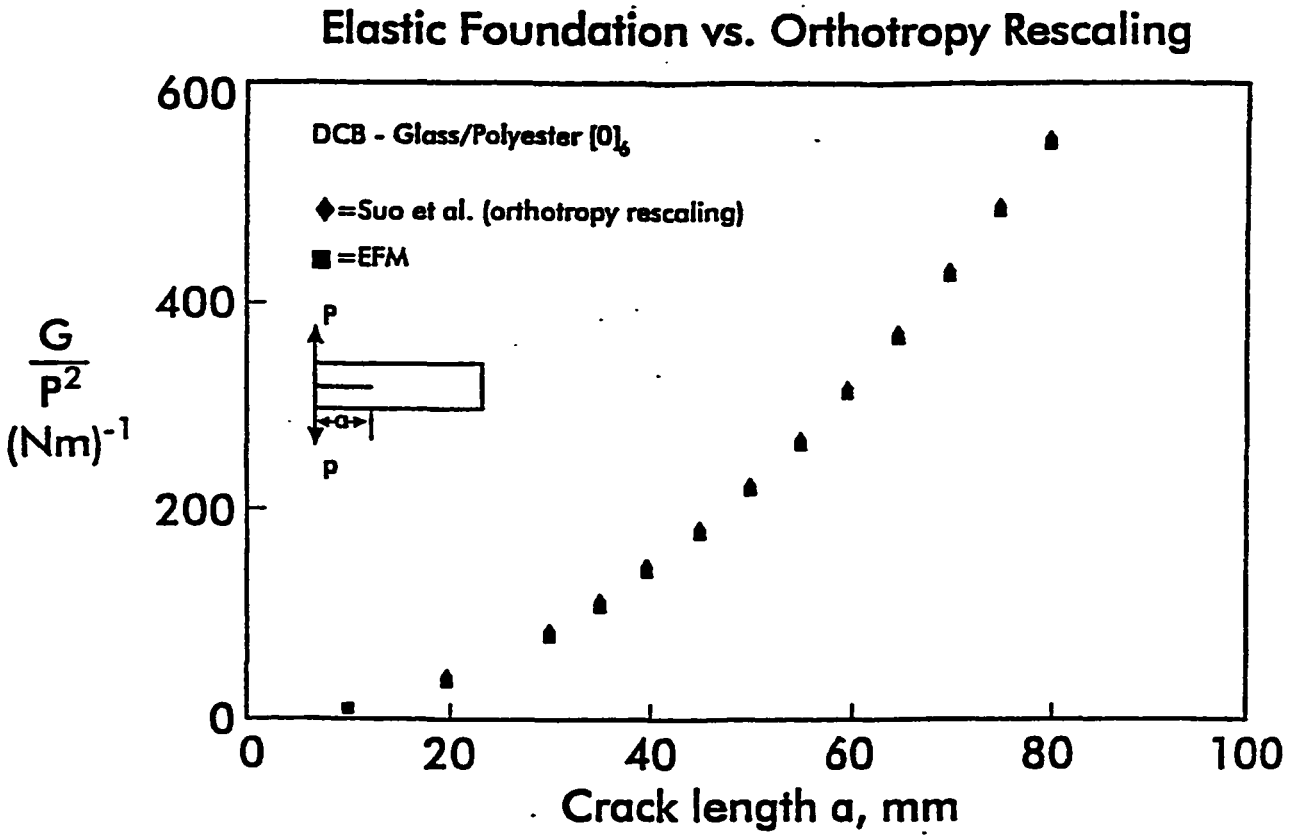

Fig. 3.9 Comparison of strain energy release rate vs. crack length data obtained from elastic foundation and orthotropy rescaling models for a $[0]_6$ glass/polyester specimen.

Table 3.1 Mechanical properties of unidirectional E-glass/polyester. E_{1f} represents the flexural modulus.

E_1, GPa	E_2, GPa	ν_{12}	G_{12}, GPa	E_{1f}, GPa
34.7	8.50	0.27	4.34	29.1

by the compliance calculated from CPT and the results are plotted versus the number n in Figure 3.10. As can be seen, the difference between the two approaches is negligible (< 3%) for thin laminates (h/L < .06). The discrepancy, however, becomes significant for thicker laminates, i.e. for n > 5. For a $[\pm 30]_{11}$ laminate, the difference between SBT and CPT predictions of the ENF specimen compliance is about 13%. The energy release rate calculated using the two approaches, however, is very close (within .01%) for all values of n considered. This calculation supports the earlier statement that shear deformation has negligible effect on the energy release rate for such specimens. The closeness between the two approaches also indicates that the unsymmetry of the full laminate and presence of non-zero D_{16} and D_{26} stiffnesses of the sublaminates have very little effect on the global compliance and overall energy release rate of this type of ENF specimens.

Crews and Reeder [35] showed that G_I/G_{II} for unidirectional laminates is almost entirely governed by the test geometry parameters c and L. Using finite element analysis, they predicted G_I/G_{II} ratios of 4, 1, and 0.25 at load positions, c, of 28, 42, and 97 mm, respectively. Within the useful delamination length range of 25 to 45 mm, the predicted G_I/G_{II} ratios varied only about 5% [35]. To examine the mode mixity for unidirectional and angle-ply laminates, calculations were performed on the glass/polyester laminates considered in the experiments described later in Chapter 4. Figure 3.11 illustrates the dependence of mode ratio on ply angle at some fixed loading lever positions (c). G_I/G_{II} shows a slight minimum at $\theta = 30°$ apparently due to elastic coupling effects. Overall, there is only a small variation in the mode ratio over the range of ply angles considered.

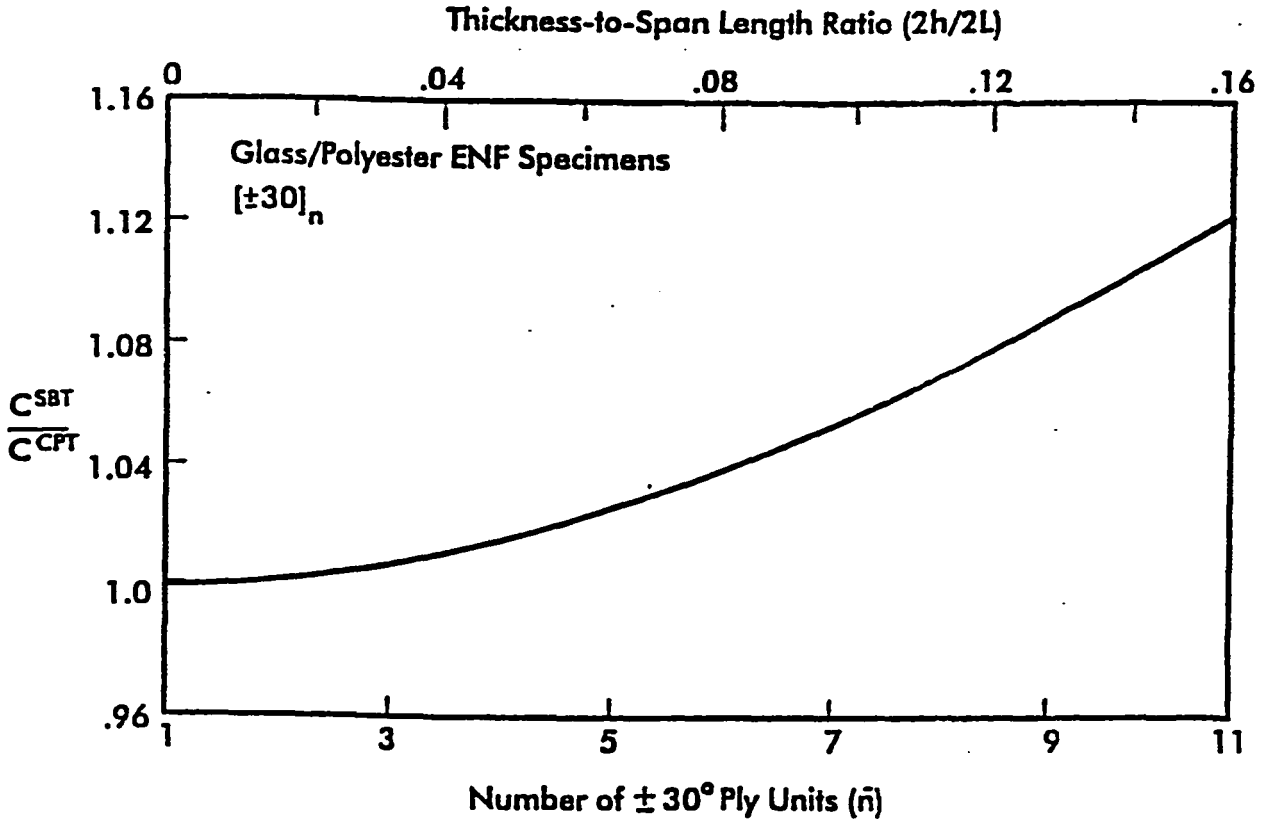

Fig. 3.10 Compliance, C^{SBT}, calculated from shear deformation beam theory formulation normalized with compliance calculated from a classical plate theory expression [16], C^{CPT}, versus number of ±30° ply units in a glass/polyester ENF specimen (L=50 mm, a=25 mm).

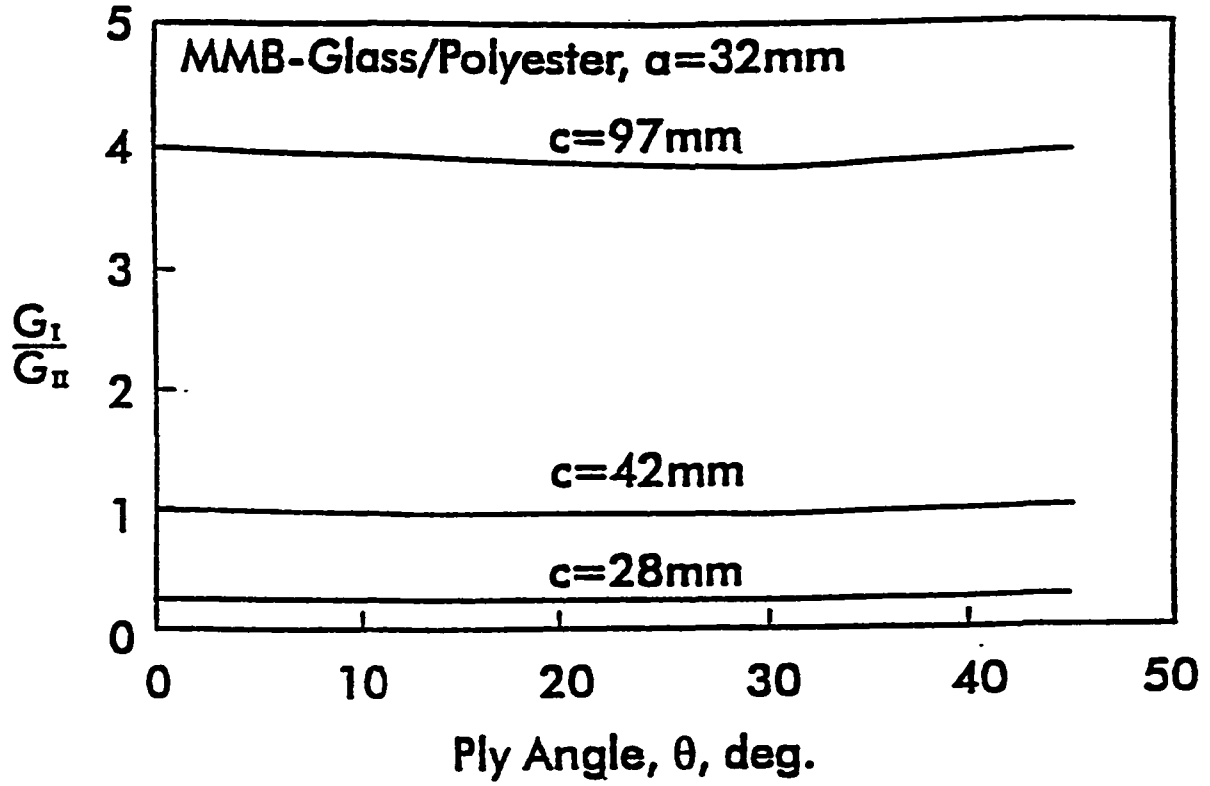

Fig. 3.11 Mode ratio G_I/G_{II} vs. ply angle for $[\pm\theta]_5$ glass/polyester laminate MMB specimens at various load positions (c) (a = 32 mm).

Figure 3.12 illustrates the dependence of mode ratio on crack length for the glass/polyester unidirectional and angle-ply laminates. G_I/G_{II} shows a small dependency of crack length, which is an advantage for experimental fracture testing. The ratio G_I/G_{II} is least for the $[\pm 30]_5$ laminate, consistent with the results in Fig. 3.11.

3.2 Bending Analysis of Cylinder Specimens

In this section, analysis of specimens cut from the filament-wound composite cylinders, see Fig. 3.13, will be developed. A complication in the analysis of the composite cylinder beam specimens is their curved cross-section. This has the consequence, as will be shown, that the sub-laminates possess dissimilar bending rigidities. Additionally, sometimes the sub-laminates of the cracked region are of unequal thickness as a result of processing, see Fig. 3.13. Furthermore, the cylinders were processed at elevated temperatures which induce residual stresses upon cool-down to room temperature. Such stresses are partly released upon crack propagation which may contribute to the energy release rate.

Bending analysis of angle-ply laminate DCB, ENF, and MMB beam specimens machined from composite cylinders is based on the first order laminated shell theory including shear deformation reviewed in Chapter 2. The elastic foundation (EF) model for flat, symmetric angle-ply beam specimens is modified to account for the curvature of the cross-section and asymmetry in lay-up and specimen geometry. The beam displacements derived from these models are used to calculate the compliance and energy release rate of the fracture specimens.

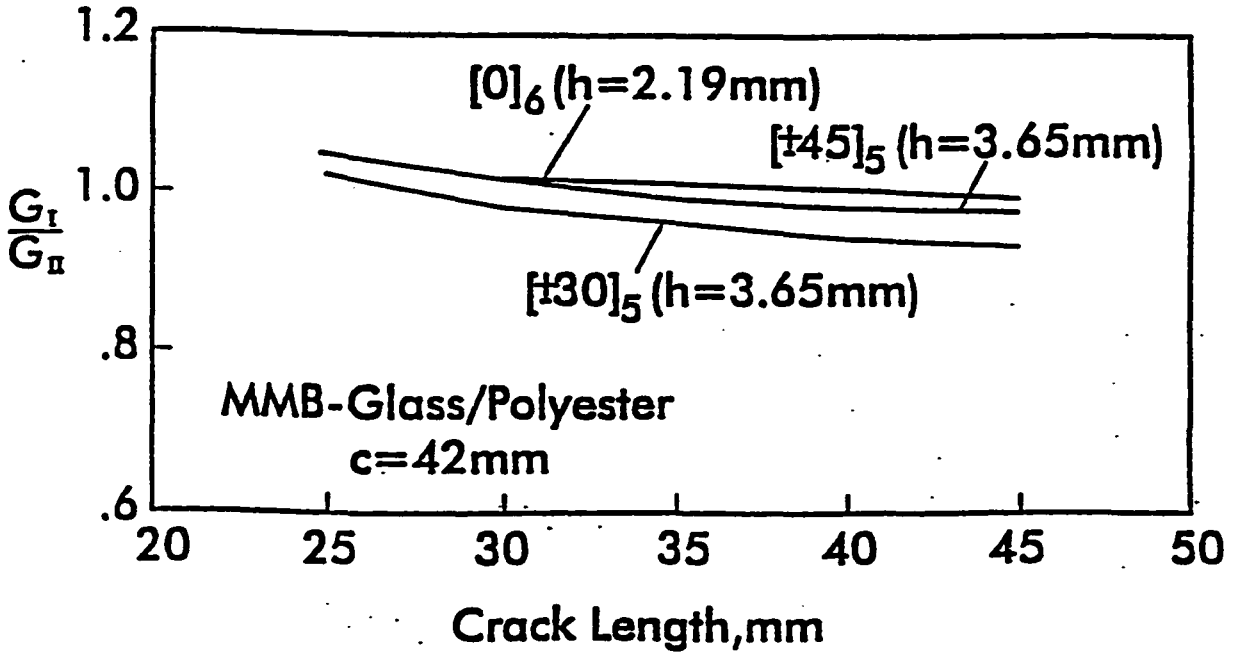

Fig. 3.12 Mode ratio G_I/G_{II} vs. crack length for various glass/polyester laminate MMB specimens (c = 42 mm).

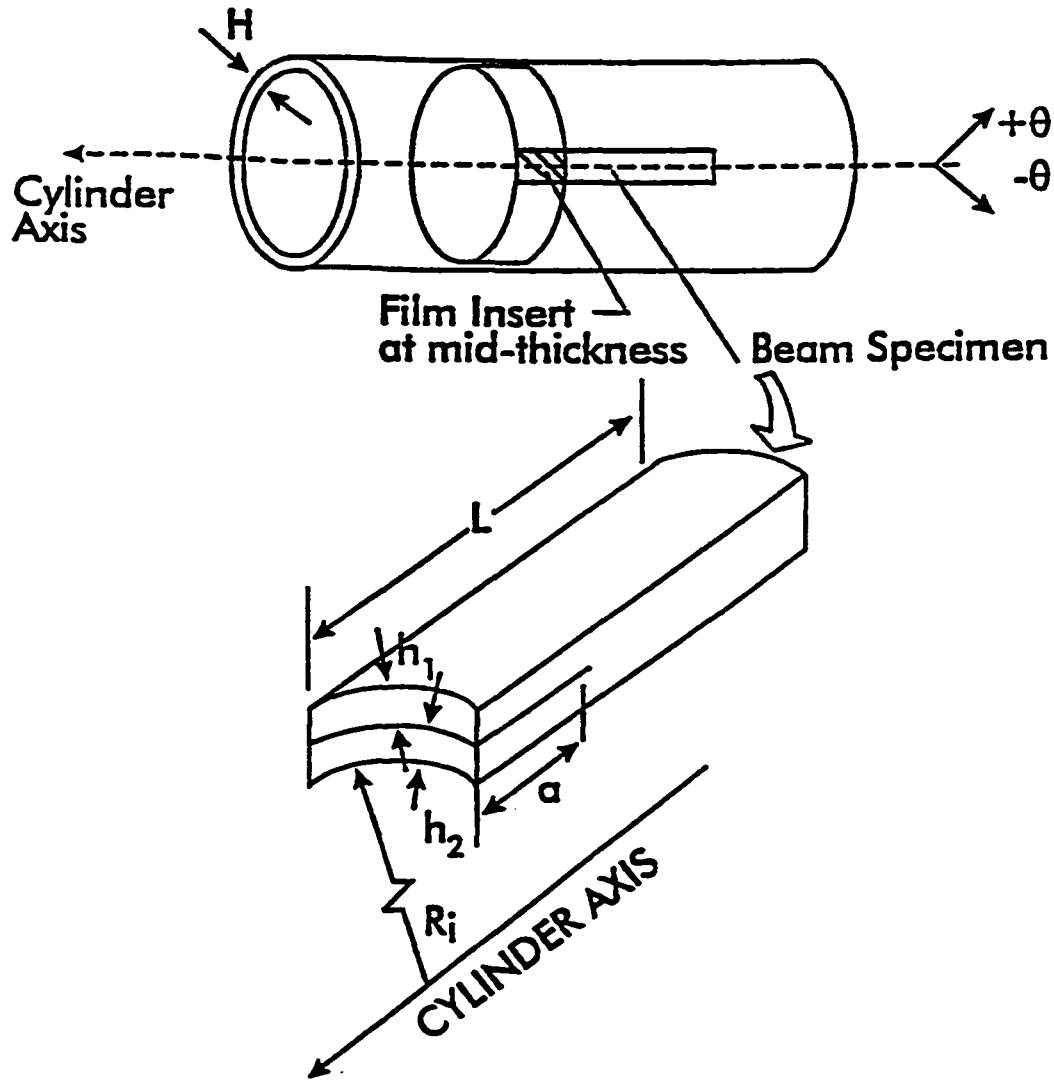

Fig. 3.13 Beam fracture specimens machined from angle-ply, filament wound cylinders.

We will specifically consider the $[\pm\theta]_n$ (n = 6,12) lay-ups used in the test specimens, but the analysis may be extended to more general lay-ups. Consideration of the stiffness matrices for the anti-symmetric $[\pm\theta]_n$ (n = 6,12) lay-ups (eq. (2.39)) reveals that the full laminate (undelaminated region) and the sub-beams of the delaminated region are unsymmetric for both n = 6 and n = 12, and hence, possess extension/twist coupling through the non-zero B_{16} and B_{26} terms. There is, however, no bending/twist coupling in the full and sub-laminates by virtue of $D_{16} = D_{26} = 0$, which is an advantage for testing and analysis of the beam fracture specimens. Due to unsymmetry, however, such laminates tested at a temperature different than the cure temperature would experience release of residual thermal stresses during crack extension which must be accounted for in the fracture energy balance. This feature will be considered in detail next.

3.2.1 Analysis of Residual Thermal Stresses on Energy Release Rate

As mentioned above, the curved glass/epoxy laminates considered in the present analysis and experiments, Chapter 4, are unsymmetric by virtue of non-zero B_{16} and B_{26} terms. The cylinders were cured at a temperature of 160 °C. Because of the elevated processing temperature, residual thermal stresses will develop when such laminates are cooled down to room temperature after cure. During propagation of a crack at the mid-surface, the residual thermal stresses relax and contribute to the release of strain energy that drives crack propagation [46].

Figure 3.14 shows the laminate model of the lay-ups considered herein. The model contains a delamination at the mid-plane as for the laminates considered, but neglects the curvature of the cross-section. Since the shell is relatively flat, we expect that this simple analysis will provide a reasonable estimate of the release of strain energy due to residual thermal stresses upon crack growth.

The potential energy available for crack growth is [33]

$$H = W - U \tag{3.38}$$

where W is the work done by the movement of external forces and U is the elastic strain energy stored in the body. Since we are interested in release of strain energy associated with residual stresses, we will assume that the body is free from external tractions, i.e., W = 0. G becomes [33],

$$G = \frac{\partial H}{\partial A} = -\frac{\partial U}{\partial a} \tag{3.39}$$

where A (A= ba) is the cracked area, b is the laminate width, and a is the crack length. The elastic energy U is defined as [47],

$$U = \int_V \Psi dV \tag{3.40}$$

where ψ is the strain energy density including the effects of thermal expansion given by [47],

$$\Psi = C_{ij}^{\cdot}(\frac{1}{2}\varepsilon_i\varepsilon_j - \alpha_i\varepsilon_j\Delta T) \qquad (i,j = 1,2,...6) \tag{3.41}$$

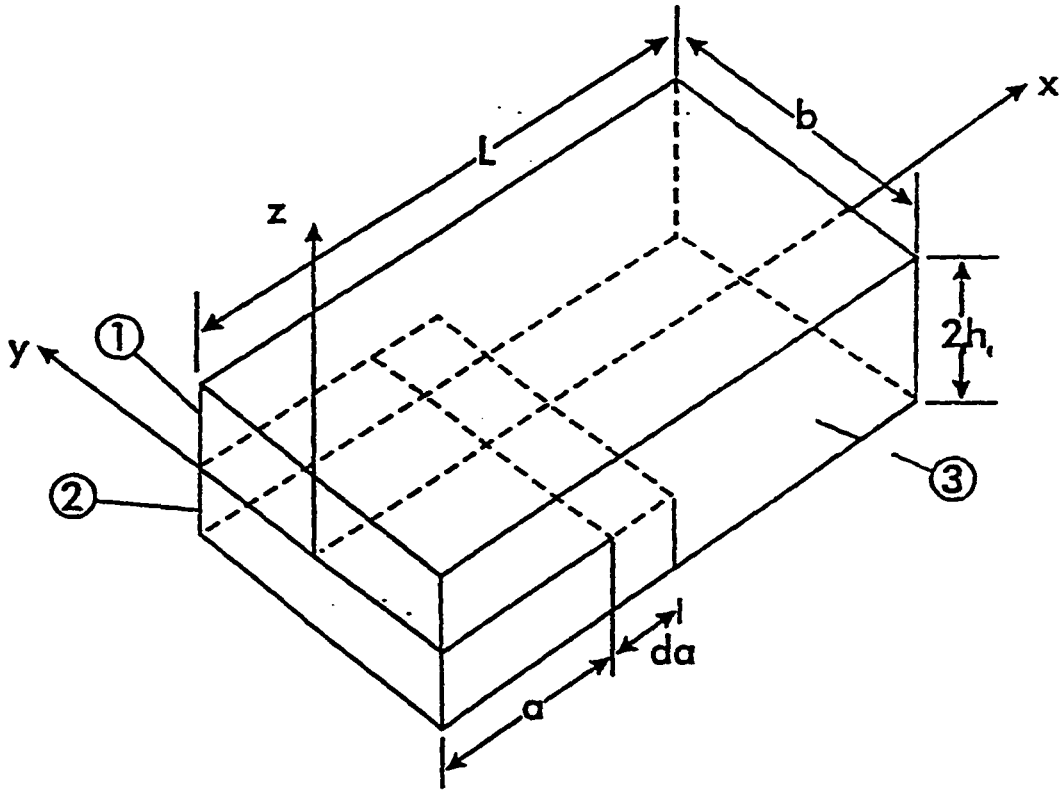

Fig. 3.14 Cracked laminate element.

where C_{ij}' are the anisotropic stiffnesses, eq. (2.5), ε_i are components of strain tensor of linear elasticity, and α_i are the material's linear coefficients of thermal expansion. ΔT is the temperature change defined positive for a temperature increase. C_{ij}' and α_i will be assumed to be independent of temperature although this is not a restriction in the analysis. The analysis assumes that Kirchhoff's hypothesis employed in CLPT, Chapter 2, is valid and that each ply is in a state of plane stress. Because of the latter assumption the only strain components in eq. (3.41) that contribute to the strain energy density are ε_1 ($= \varepsilon_x$), ε_2 ($= \varepsilon_y$) and γ_{12} ($= \gamma_{xy}$) given by eq. (2.11). For plane stress, C_{ij}' in eq. (3.41) are replaced by reduced stiffness matrix Q_{ij}' defined in Ref. [18]. Hence, the strain energy density ψ becomes,

$$\Psi = Q_{ij}'\left(\frac{1}{2}\varepsilon_i\varepsilon_j - \alpha_i\varepsilon_j\Delta T\right) \qquad (i,j = 1,2,6) \tag{3.42}$$

The total strain energy U of the laminate in Fig. 3.14 is obtained by adding the contributions from each of its regions 1, 2, 3,

$$U = \int_0^a \int_{-b/2}^{b/2} \int_0^h \Psi_1 dV_1 + \int_0^a \int_{-b/2}^{b/2} \int_{-h}^0 \Psi_2 dV_2 + \int_a^L \int_{-b/2}^{b/2} \int_{-h}^h \Psi_3 dV_3 \tag{3.43}$$

For the $[\pm\theta]_n$ (n = 6,12) laminates considered herein, the sub-laminate regions 1 and 2 of the laminate in Fig. 3.14 have identical lay-ups, i.e., $[\pm\theta]_{n/2}$ (n = 6,12), hence the first two integrals in eq. (3.43) are identical. In addition, we will neglect the local disturbances in the strain field around the crack front and assume that the strains ε_1, ε_2, and γ_{12} do not vary across the width and along the length for each region. Using eqs. (3.43) and (3.39) and rearranging, the energy release rate due to thermal residual stresses can be expressed as,

$$G = \int_{-h}^{h} \Psi_3 \, dz - 2 \int_{-h/2}^{h/2} \Psi_1 \, dz \tag{3.44}$$

Note that the integrals in eq. (3.44) must be computed ply by ply. Analysis of the sub-laminates (regions 1 and 2) and full laminate (region 3) using CLPT gives $\gamma_{xy}^{\circ} = \kappa_x = \kappa_y = \alpha_{xy} = 0$. Hence, the strains ε_1, ε_2, and γ_{12} become,

$$\begin{aligned} \varepsilon_1 &= \varepsilon_x^{\circ} \\ \varepsilon_2 &= \varepsilon_y^{\circ} \\ \gamma_{12} &= z\kappa_{xy} \end{aligned} \tag{3.45}$$

The calculation of G due to thermal residual stresses is straightforward with the aid of a computer program. The reduced stiffnesses Q_{ij}' are computed using basic ply properties. Then, the strains ε_1, ε_2, and γ_{12} are calculated from CLPT using eq. (3.45). The calculation of ψ for regions 1 and 3, Fig. 3.14, of the cracked laminate follows next according to eq. (3.42). Finally, G is computed using eq. (3.44).

3.2.2 Bending Analysis of Cylinder DCB Specimen

Figure 3.15 shows the geometry and loading of a DCB specimen with a curved cross-section machined from the wall of a filament wound cylinder, Fig. 3.13. The analysis presented in Sect. 3.1.1 for flat, symmetric ($h_1=h_2$), angle-ply laminate DCB specimens will here be modified to analyze curved DCB specimens machined from composite cylinders.

The beam model for the unsymmetric ($h_1 \neq h_2$) DCB specimen considered herein is illustrated in Fig. 3.16. The cracked region is considered as two free beams of length "a"

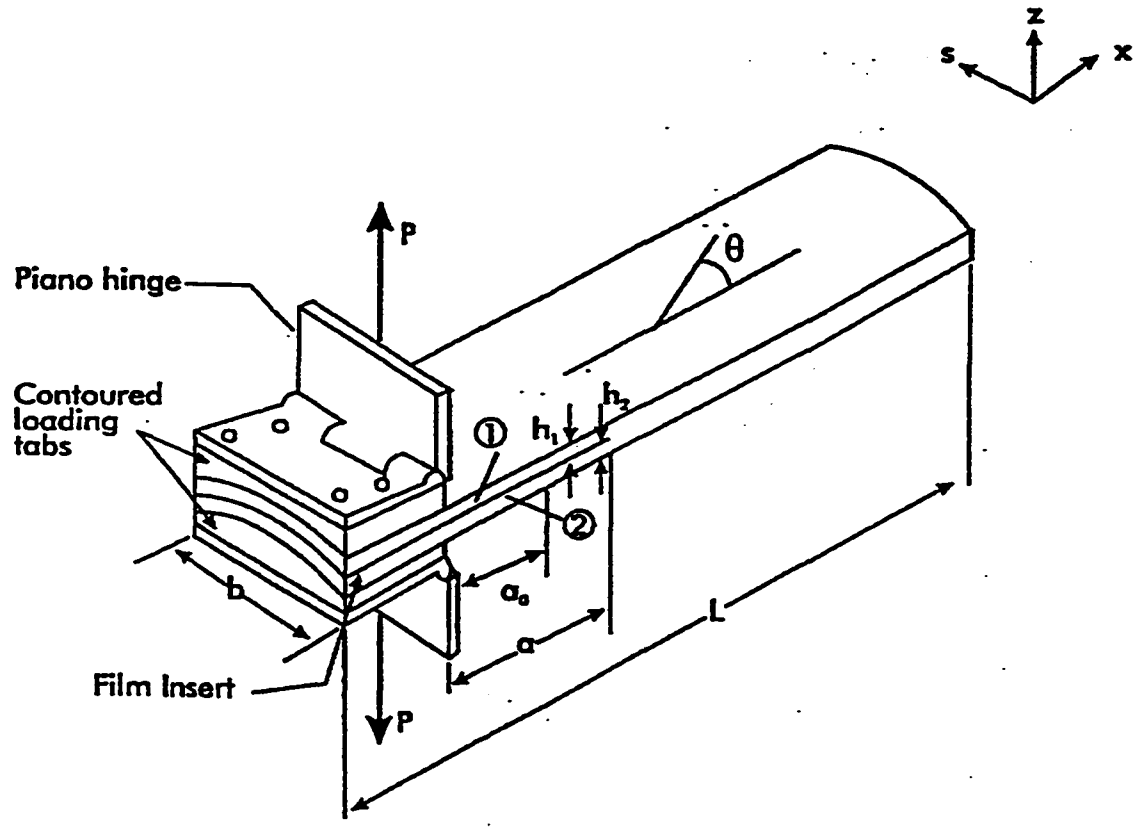

Fig. 3.15 Geometry and loading of angle-ply laminate DCB specimen with curved cross-section. 1 and 2 denote upper and lower sub-beams of the delaminated region.

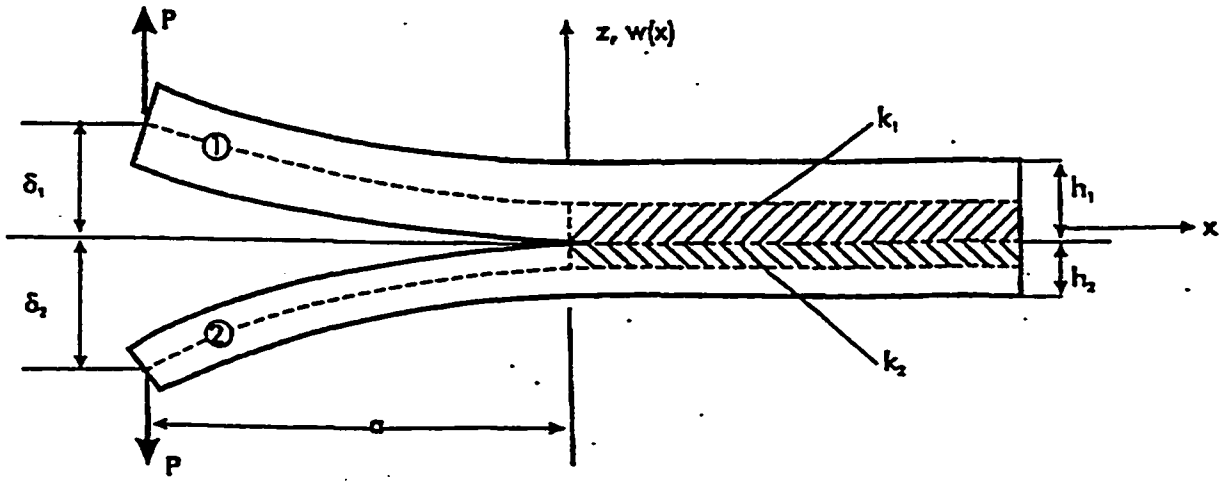

Fig. 3.16 Elastic foundation model for the unsymmetric DCB specimen.

loaded with concentrated loads of magnitude P at their ends. The uncracked beam sections beyond the crack tip are modeled as Winkler type elastic foundations with moduli k_1 and k_2.

A beam analysis of the angle-ply DCB specimen may conveniently be formulated using the compliance form of the shell constitutive relations, eqs. (2.40). For analysis of the beam specimen under bending moment M_x, eqs. (2.40) yield,

$$\kappa_x = d_{11} M_x \tag{3.46}$$

where d_{11} is the i = j = 1 element of the bending compliance matrix [d] given by eqs. (2.41). The curvature κ_x is given by,

$$K_x = \frac{d\psi_x}{dx} \tag{3.47}$$

Equations (3.46) and (3.47) combined constitute the basic differential equation for bending analysis of a laminated beam with curved cross-section. Equation (3.45) corresponds to the familiar equation of elementary beam theory [41],

$$\kappa_x = \frac{M}{EI} \tag{3.48}$$

To proceed, we identify M in eq. (3.48) as, $M = M_x b$, where b is the width of the DCB specimen, Fig. 3.15. An expression for the area moment of inertia for a beam with curved cross-section is derived in Appendix C. Comparison of eqs. (3.46) and (3.48) indicates that, for the curved cross-section beams considered, $d_{11} = b/(EI)$, where the modulus E is the effective bending modulus, E_x^b, which may be different than the extensional modulus, E_x. For the anti-symmetric angle-ply laminates under consideration, however,

calculations using ply data listed in Table 3.2 reveal insignificant differences, see Table 3.3.

The governing differential equation for the deflection $w_i(x)$ of each arm (sub-laminate) (i = 1,2), Fig. 3.16, may be written as,

$$\frac{d^4 w_i(x)}{dx^4} + 4\lambda_i^4 H(x)\, w_i(x) = 0 \tag{3.49}$$

where

$$H(x) = \begin{cases} 1 & x > 0 \\ 0 & x < 0 \end{cases} \tag{3.50a}$$

and

$$\lambda_i^4 = \frac{k_i}{4 E_{x,i} I_i} \tag{3.50b}$$

in which k_i is the foundation modulus, $E_{x,i}$ is the effective modulus, and I_i is the area moment of inertia for each sub-beam. Notice that for the curved angle-ply laminate specimens considered E_x is the same for both sublaminates because of their anti-symmetric angle-ply lay-ups, i.e., $E_{x,1} = E_{x,2} = E_x$.

The foundation modulus for each sub-laminate may be related to the out-of-plane extensional modulus (E_z) of the laminate using eq. (3.6),

$$k_i = \frac{2 E_z\, b}{h_i} \tag{3.51}$$

Table 3.2 Mechanical properties and coefficients of thermal expansion of unidirectional E-glass/epoxy.

E_1, GPa	E_2, GPa	ν_{12}	G_{12}, GPa	α_1, 10^{-6}/°C	α_2, 10^{-6}/°C
39.4	8.0	0.3	4.0	6.3	23.3

Table 3.3 Extensional and bending moduli, E_x and E_x^b, of glass/epoxy angle-ply laminates with curved cross-section.

Lay-up	$[\pm 30]_6$	$[\pm 55]_6$	$[\pm 85]_6$	$[\pm 30]_{12}$	$[\pm 55]_{12}$	$[\pm 85]_{12}$
E_x, GPa	21.40	9.52	8.01	21.70	9.58	8.01
E_x^b, GPa	21.30	9.54	8.01	21.70	9.56	8.01

where subscript i denotes the sub-laminates 1 and 2 in Fig. 3.16. E_z is estimated using the laminate homogenization method of Hyer and Knott [40], Appendix A. Then, from eqs. (3.50b) and (3.51),

$$\lambda_i = \left(\frac{b}{2 h_i I_i} \frac{E_z}{E_x} \right)^{\frac{1}{4}} \tag{3.52}$$

Once the parameters λ_i have been established, eq. (3.49) may be integrated yielding the displacements δ_1 and δ_2 at the ends of the beams, see Fig. 3.16. The total separation, δ, of the two ends is calculated using simple superposition, i.e.,

$$\delta = \delta_1 + \delta_2 \tag{3.53}$$

This analysis assumes that the beams are horizontal far away from their loaded ends (Fig. 3.16) and neglects possible geometrical nonlinearity effects due to rotation of the intact region of the beam as discussed by Sundararaman et al. [20]. The analysis should thus be limited to DCB specimens with relatively small asymmetry in specimen geometry. According to the detailed nonlinear finite element analysis of unsymmetric DCB specimens performed by Sundararaman et al. [20], the nonlinear effects on the beam displacements, δ, and the mixed mode effects due to asymmetry can be neglected for DCB specimen with thickness ratio h_1/h_2 (or h_2/h_1) < 2. For the particular laminates examined in our experiments, the ratio h_1/h_2 ranges from 0.9 to 1.6. Thus, the effects of asymmetry on beam displacement, δ, and mode mixity may be neglected.

Following the solution procedure for the flat DCB specimen outlined in Sect. 3.1.1, the DCB specimen compliance, $C = \delta/P$, can be written as,

$$C=\frac{a^3}{3E_x}\left\{\begin{array}{l}\frac{1}{I_1}\left[1+\frac{3.57}{a}\left(\frac{E_x}{E_z}\frac{h_1 I_1}{b}\right)^{1/4}+\frac{4.24}{a^2}\left(\frac{E_x}{E_z}\frac{h_1 I_1}{b}\right)^{1/2}+\frac{2.52}{a^3}\left(\frac{E_x}{E_z}\frac{h_1 I_1}{b}\right)^{3/4}\right] \\ +\frac{1}{I_2}\left[1+\frac{3.57}{a}\left(\frac{E_x}{E_z}\frac{h_2 I_2}{b}\right)^{1/4}+\frac{4.24}{a^2}\left(\frac{E_x}{E_z}\frac{h_2 I_2}{b}\right)^{1/2}+\frac{2.52}{a^3}\left(\frac{E_x}{E_z}\frac{h_2 I_2}{b}\right)^{3/4}\right]\end{array}\right\} \tag{3.54}$$

The energy release rate, G, available for propagating the crack is obtained using eq. (2.44). Combination of eqs. (3.54) and (2.44) yields,

$$G=\frac{P^2 a^2}{2bE_x}\left\{\begin{array}{l}\frac{1}{I_1}\left[1+\frac{2.38}{a}\left(\frac{E_x}{E_z}\frac{h_1 I_1}{b}\right)^{1/4}+\frac{1.41}{a^2}\left(\frac{E_x}{E_z}\frac{h_1 I_1}{b}\right)^{1/2}\right] \\ +\frac{1}{I_2}\left[1+\frac{2.38}{a}\left(\frac{E_x}{E_z}\frac{h_2 I_2}{b}\right)^{1/4}+\frac{1.41}{a^2}\left(\frac{E_x}{E_z}\frac{h_2 I_2}{b}\right)^{1/2}\right]\end{array}\right\} \tag{3.55}$$

The energy release rate for the unsymmetric DCB specimen given by classical beam theory [41] is,

$$G=\frac{P^2 a^2}{2bE_x}\left(\frac{1}{I_1}+\frac{1}{I_2}\right) \tag{3.56}$$

This expression is strictly valid only for infinitely long crack lengths. The terms inside the parentheses in eq. (3.55) are elastic foundation correction factors that account for finite crack lengths and transverse elasticity of the uncracked region of the specimen.

The beam analysis presented here may be applied for prediction of compliance and overall energy release rate of laminated DCB specimens with curved cross-section,

but does not provide local mode mixity at the crack front. A three-dimensional finite element analysis of flat DCB specimens with anti-symmetric lay-ups [16] indicates that the mode II and mode III contributions to G are negligible (<1%). It is clear, however, that contribution from other modes may occur in testing of curved DCB specimens. In the extreme case of a semi-circular DCB specimen, the edges of the specimen will be predominantly in mode III [48]. Davies and Rannou [48] examined DCB specimens similar to ours. Using a simple kinematic model, they estimated the mode I component in the shallow shell specimens, and found that the crack tip loading at the specimen edges is more than 99% mode I. Therefore, the fracture toughness evaluated from the DCB specimens examined herein is expected to represent close to pure mode I conditions at the crack front.

3.2.3 Bending Analysis of Cylinder ENF Specimen

Figure 3.17 shows an angle-ply laminate ENF specimen with curved cross-section machined from the wall of a filament wound cylinder. The cross-sectional geometry and the loading of the curved ENF specimen is illustrated in Fig. 3.18. A beam analysis of the curved, angle-ply laminate ENF specimen may be formulated using the compliance forms of the constitutive relations for bending and shear of the curved shell, eqs. (2.39) and (2.43). The moment-curvature relation is given by eq. (3.46) presented earlier. In addition to bending, the ENF beam may undergo shear deformation. This influence may be examined using the one-dimensional versions of eqs. (2.34) and (2.37),

$$\begin{aligned} u &= u(x,z) = u^{\circ}(x) + z\psi_x(x) \\ \psi_x(x) &= \gamma_{xz} - \frac{dw}{dx} \end{aligned} \tag{3.57}$$

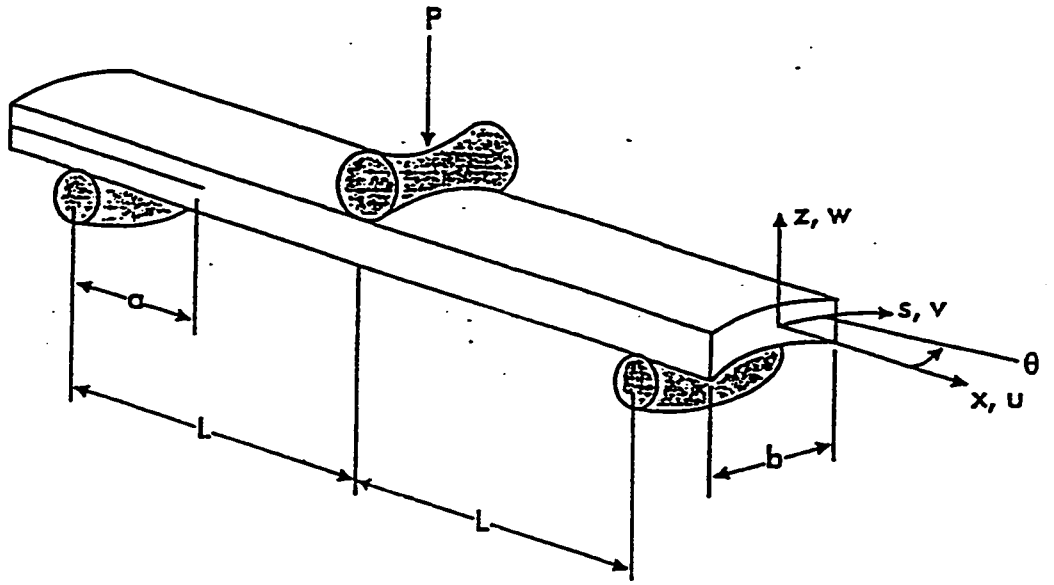

Fig. 3.17 Geometry and loading of angle-ply laminate ENF specimen with curved cross-section. 1 and 2 denote upper and lower sub-beams of the delaminated region.

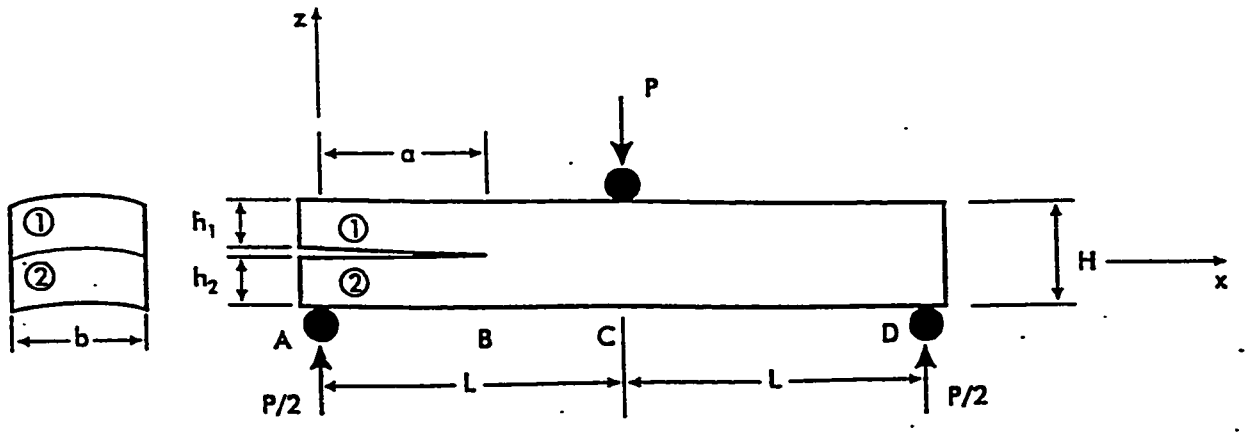

Fig. 3.18 Definition of delaminated (A-B) and intact (B-C-D) sections of the curved ENF specimen. 1 and 2 denote upper and lower sub-beams of the delaminated region.

The compliance form of the constitutive relation for shear of the curved shell, eq. (2.43), is,

$$\begin{bmatrix} \gamma_{sz} \\ \gamma_{xz} \end{bmatrix} = \frac{1}{k} \begin{bmatrix} a_{44} & a_{45} \\ a_{45} & a_{55} \end{bmatrix} \begin{bmatrix} Q_s \\ Q_x \end{bmatrix} \tag{3.58}$$

which yields,

$$\gamma_{xz} = \frac{a_{55} Q_x}{k} \tag{3.59}$$

where a_{55} is given in eq. (3.26). The A_{ij} terms in eq. (3.26) are calculated for the curved ENF specimens using eq. (2.32).

Once the basic bending and shear deformation equations have been established, we may proceed to solve for the beam deflection for the angle-ply laminate ENF specimen with curved cross-section. The solution is equivalent to that for flat, angle-ply laminate ENF specimens presented earlier, sect. 3.1.2, with d_{11} replaced here by $d_{11} = b/(E_x I)$, where E_x is the effective bending modulus. The beam compliance is thus given by,

$$C = \frac{L^3 (d_{11})_{BC}}{6b} + \frac{L (a_{55})_{BC}}{2bk} + \frac{a^3 \left[(d_{11})_{AB} - (d_{11})_{BC} \right]}{12b} + \frac{a \left[(a_{55})_{AB} - (a_{55})_{BC} \right]}{4bk} \tag{3.60}$$

where a is the crack length, $(d_{11})_{AB}$ and $(d_{11})_{BC}$ are the effective bending compliances of the delaminated region AB and undelaminated region BC, Fig. 3.18, $(a_{55})_{AB}$ and $(a_{55})_{BC}$

are the effective shear compliances of regions AB and BC, and k is the shear correction factor (k = 5/6).

The effective bending and shear compliances of the delaminated region AB are defined by eq. (3.23). It is recognized that the sub-laminates of the delaminated region in general have different moments of inertia (I) because of their curved geometry and dissimilar thicknesses h_1 and h_2 (Figs. 3.14 and 3.18). Consequently,

$$(d_{11})_1 \neq (d_{11})_2 \tag{3.61}$$

and

$$(a_{55})_1 \neq (a_{55})_2 \tag{3.62}$$

As a result, the sub-laminates in the delaminated region do not carry equal load (P/4) as in the case of a flat ENF specimen with mid-plane delamination, Sect. 3.1.2. With $d_{11} = b/(E_x I)$, the effective bending compliance of the delaminated region AB, $(d_{11})_{AB}$, becomes,

$$(d_{11})_{AB} = \frac{b}{E_x(I_1 + I_2)} \tag{3.63}$$

where I_1 and I_2 are the moment of inertia of the upper and lower sub-laminates of the delamination region, respectively, see Fig. 3.18. The effective shear compliance of the delaminated region, $(a_{55})_{AB}$, is calculated using eq. (3.23b) with the shear compliance a_{55} given in eq. (3.26).

The energy release rate, G, available for propagating the crack is obtained by substitution of eq. (3.59) into eq. (2.44),

$$G=\frac{P^2}{8b^2}\left\{ a^2\left[(d_{11})_{AB}-(d_{11})_{BC}\right]+\frac{(a_{55})_{AB}-(a_{55})_{BC}}{k} \right\} \tag{3.64}$$

For the curved angle-ply laminates considered, it may be shown that $(a_{55})_{AB}\approx(a_{55})_{BC}$, since A_{45} is small in comparison to A_{44} and A_{55}. Hence, although shear deformation contributes to the ENF specimen compliance, there is no or very small contribution from shear deformation to the energy release rate for the laminates considered.

In the case of unequal thicknesses of the upper and lower sub-laminates ($h_1 \neq h_2$ in Fig. 3.18), the sub-laminate with the larger bending rigidity will carry most load and govern the response of the delaminated region and the load transfer between the sub-laminates. A thicker sub-laminate on the bottom will lead to crack face contact over the majority of the crack length which may require contact analysis [20]. Thus, to avoid the complications due to crack surface contact, the analysis and the experiments consider only geometries where the thicker sub-laminate of the beam specimen is on top. Apart from the contact problem, asymmetry in specimen geometry with respect to the crack interface may also induce local mixed mode effects [19,20]. Finite element analysis performed by Sundararaman et al. [20] for a flat, unsymmetric ENF specimen, however, shows that a large asymmetry ratio (h_1/h_2) is required, $h_1/h_2 \geq 2$ before the mode mix is significantly altered. The h_1/h_2 ratio for the specimens considered in the experiments,

Chapter 4, ranges from 1.1 to 1.6. Thus, the effect of asymmetry on mode mixity may be neglected.

3.2.4 Analysis of Cylinder MMB Specimen

Beam models developed above for angle-ply laminate DCB and ENF specimens with curved cross-section will be utilized here to analyze MMB fracture specimens, Fig. 3.7, machined from composite cylinders. Figure 3.19 shows the geometry and test configuration of a MMB specimen with curved cross-section.

As discussed in Sect. 3.1.3, the MMB loading can be represented by a superposition of mode I opening and mode II sliding equivalent to a combination of the DCB and ENF tests [35]. Thus, compliance and strain energy release rate equations from the DCB and ENF tests of angle-ply laminates with curved cross-section, Sect. 3.2.2 and 3.2.3, are combined to obtain the desired equations for the MMB test. It has to be recognized, however, that the MMB specimens machined from composite cylinders may possess asymmetry, which influences the load transfer. Figure 3.20 (top) illustrates a free body diagram for the MMB specimen obtained by static equilibrium considerations of the test geometry. Figure 3.20 also shows how the reactions may be partitioned into mode I (DCB) and mode II (ENF) contributions. Such a partitioning derived from static equilibrium is valid for asymmetric MMB specimens with different bending rigidities of the sub-laminates. The mode I and mode II "components" of the applied load, Fig. 3.20 (middle and bottom), are given by eq. (3.29). The analysis inherently assumes that the DCB and ENF specimens are pure mode I and pure mode II. Such an assumption seems

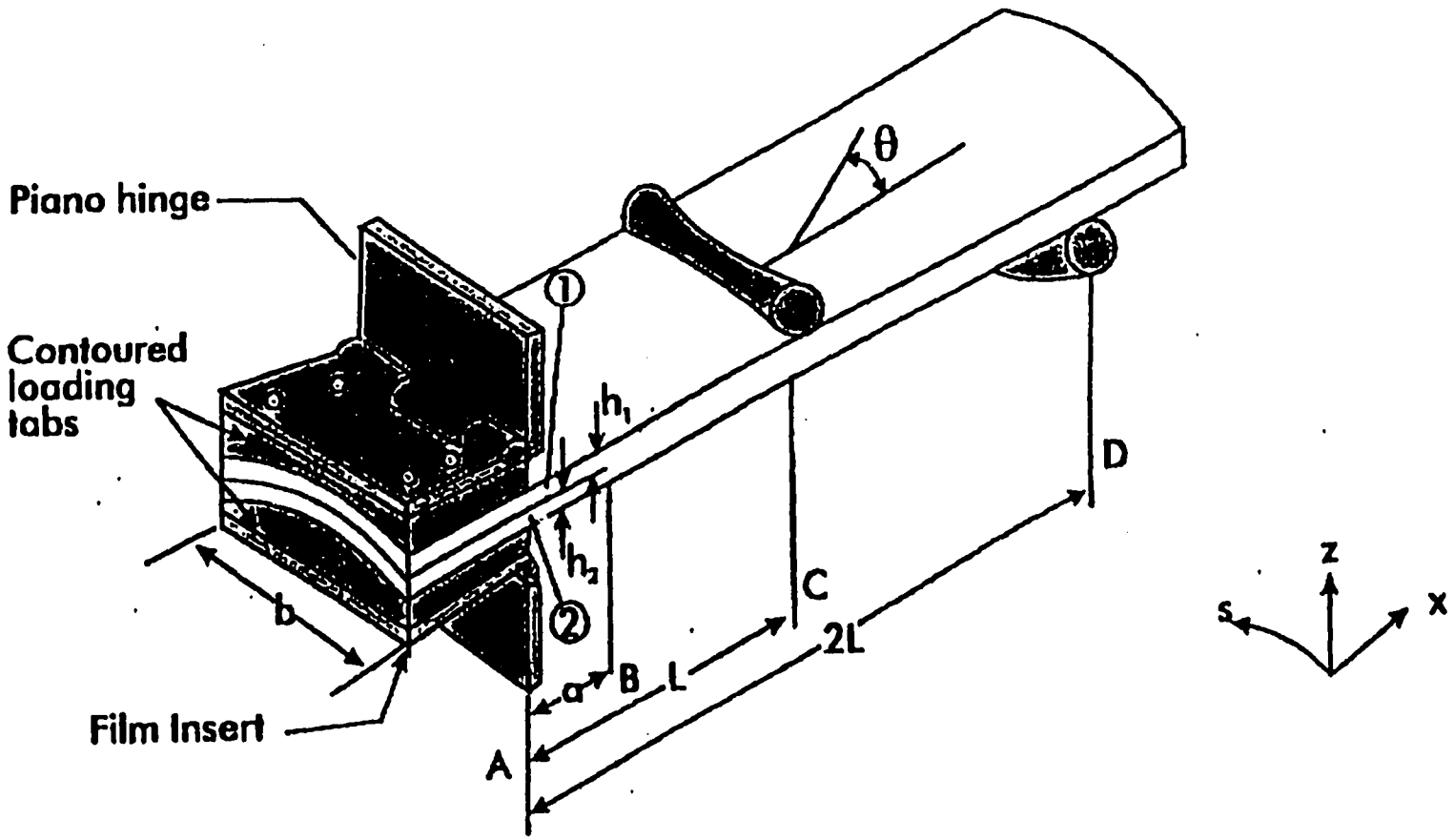

Fig. 3.19 Geometry and loading of angle-ply laminate MMB specimen with curved cross-section. 1 and 2 denote upper and lower sub-beams of the delaminated region.

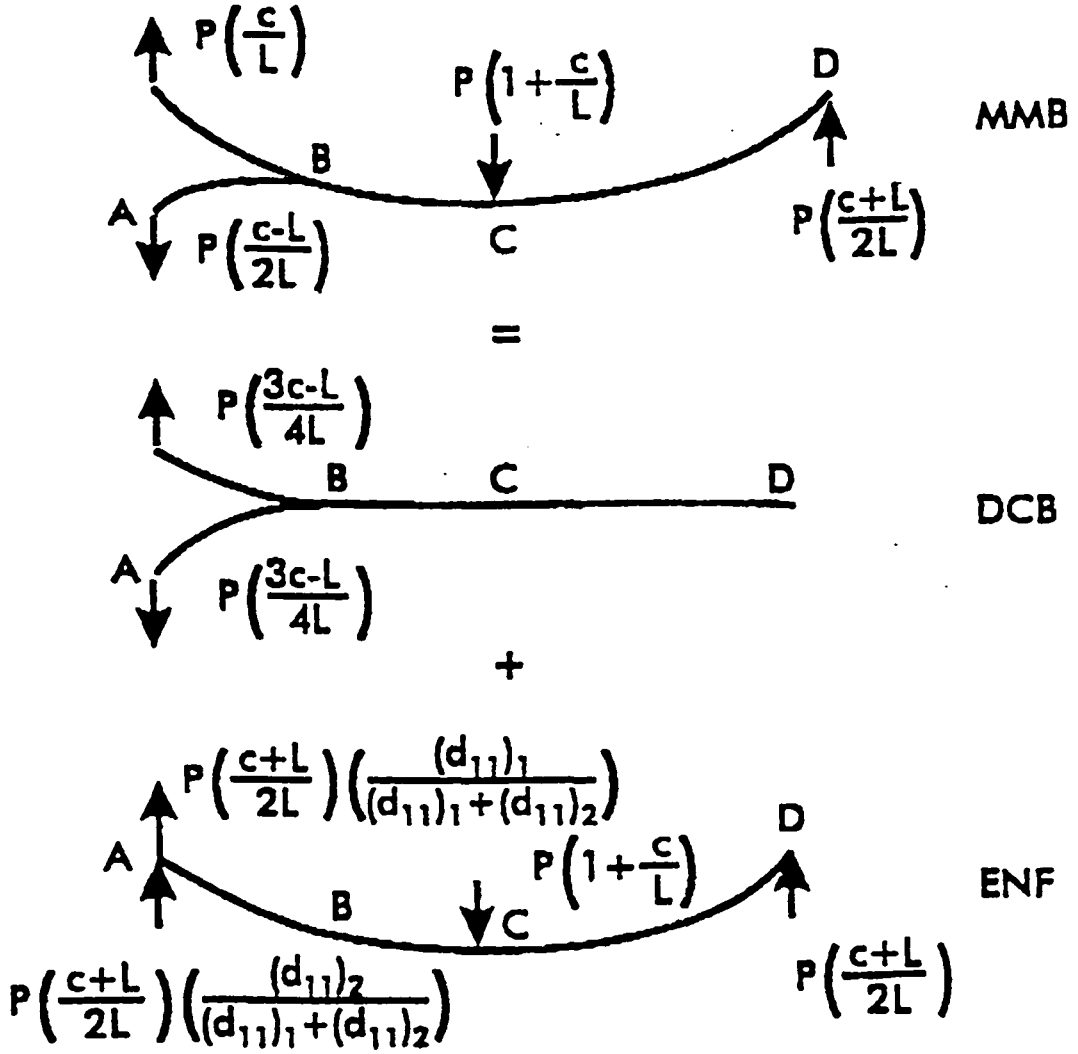

Fig. 3.20 Partitioning of load applied to the MMB specimen with curved cross-section into mode I and mode II contributions.

to be justified in a global sense although detailed numerical analysis is required to further examine this issue.

Substitution of the loads P_I and P_{II} given by eqs. (3.29) into the mode I (DCB) and mode II (ENF) energy release rate expressions, eqs. (3.55) and (3.64), gives the MMB energy release rate, $G = G_{DCB} + G_{ENF}$,

$$G=\left(\frac{Pa}{b}\right)^2\left[\frac{b}{2E_x}\left(\frac{3c-L}{4L}\right)^2\left\{\begin{array}{l}\dfrac{1}{I_1}\left[1+\dfrac{2.38}{a}\left(\dfrac{E_x}{E_z}\dfrac{h_1 I_1}{b}\right)^{1/4}+\dfrac{1.41}{a^2}\left(\dfrac{E_x}{E_z}\dfrac{h_1 I_1}{b}\right)^{1/2}\right] \\ +\dfrac{1}{I_2}\left[1+\dfrac{2.38}{a}\left(\dfrac{E_x}{E_z}\dfrac{h_2 I_2}{b}\right)^{1/4}+\dfrac{1.41}{a^2}\left(\dfrac{E_x}{E_z}\dfrac{h_2 I_2}{b}\right)^{1/2}\right]\end{array}\right\}\right. \tag{3.65}$$
$$\left.+\frac{1}{8}\left(\frac{c+L}{L}\right)^2\left[(d_{11})_{AB}-(d_{11})_{BC}\right]\right]$$

From a kinematics consideration of the deformation of the MMB test fixture and specimen, Figs. 3.7 and 3.19, the deflection, δ, at the point of load application can be obtained as,

$$\delta=\delta_c+\left(\frac{c}{L}\right)(\delta_l+\delta_c) \tag{3.66}$$

where δ_l is the opening deflection at point A in Fig. 3.19 and δ_c is the specimen's center point (fulcrum) deflection. Figure 3.21 describes the kinematics of the deformation of the MMB specimen. The bold line outlines the deformed specimen with the lower surface of

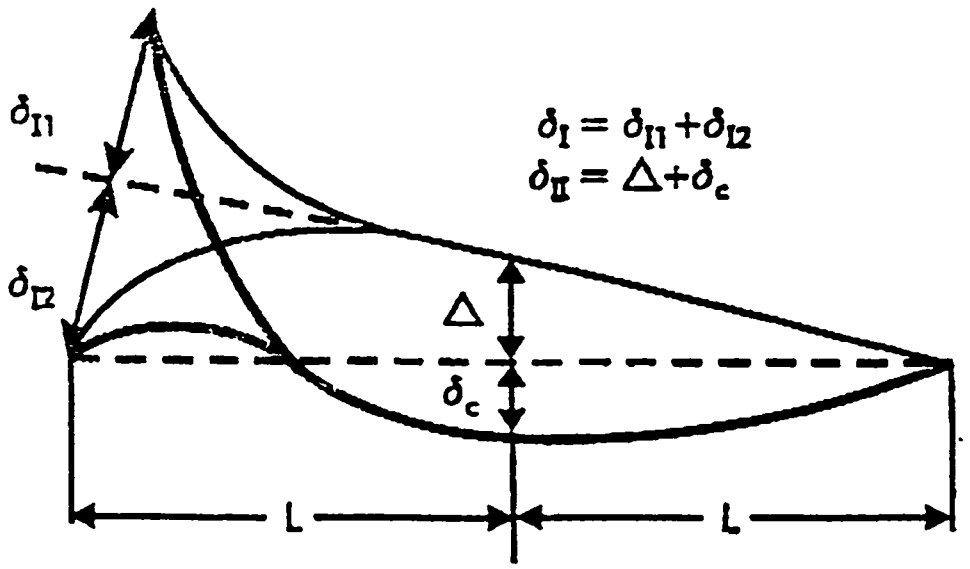

Fig. 3.21 Kinematics of deformation of unsymmetric MMB specimen.

the specimen fixed at points A and D. δ_{I1} and δ_{I2} are the opening displacements of the upper and lower cracked arms of the MMB specimen associated with the mode I opening load P_I. The thin line indicates the deformed specimen if only loads P_I are acting. $\Delta+\delta_c$ is the displacement at point C due to the mode II flexural load P_{II} with reference to the pure mode I configuration, see Fig. 3.21. The loads P_I and P_{II} are indicated in Fig. 3.21 and given in eqs. (3.29). The displacement Δ is determined from the geometry of Fig. 3.21 by using the method of similar triangles,

$$\Delta = \frac{L\,\delta_{I2}}{\sqrt{4L^2 - \delta_{I2}^{\,2}}} \tag{3.67}$$

Since $\delta_{I2}^{\,2} << 4L^2$, the expression for Δ may be approximated by

$$\Delta \approx \frac{\delta_{I2}}{2} \tag{3.68}$$

The mode II displacement δ_{II}, Fig. 3.21, becomes,

$$\delta_{II} = \delta_c + \Delta = \delta_c + \frac{\delta_{I2}}{2} \tag{3.69}$$

Substituting eq. (3.69) into eq. (3.66) and noting that $\delta_I = \delta_{I1} + \delta_{I2}$, we get,

$$\delta = \left(\frac{c}{L}\right)\delta_{I1} + \left(\frac{c-L}{2L}\right)\delta_{I2} + \left(1+\frac{c}{L}\right)\delta_{II} \tag{3.70}$$

The mode I (DCB) and mode II (ENF) components of the specimen compliance may be expressed as,

$$C_{DCB} = \frac{\delta_I}{P_I} = \frac{\delta_{I1}}{P_I} + \frac{\delta_{I2}}{P_I} = C_{DCB,1} + C_{DCB,2} \tag{3.71a}$$

$$C_{ENF} = \frac{\delta_{II}}{P_{II}} \tag{3.71b}$$

where expressions for $C_{DCB,1}$ and $C_{DCB,2}$ can be obtained from eq. (3.54) noting eq. (3.71a), and C_{ENF} is given in eq. (3.60). Substituting eqs. (3.71) and (3.29) in eq. (3.70) and dividing by the applied load P yields the MMB specimen compliance C,

$$C = \frac{c\,(3c-L)}{4L^2} C_{DCB,1} + \frac{(c-L)\,(3c-L)}{8L^2} C_{DCB,2} + \left(\frac{c+L}{L}\right)^2 C_{ENF} \tag{3.72}$$

Equations (3.65) and (3.72) incorporate the influence of transverse extensional deformation of the uncracked region of the specimen and transverse shear deformation. It also accommodates sublaminates of different bending rigidities. The fracture mode ratio, G_I/G_{II}, for the MMB test may thus be approximated as,

$$\frac{G_I}{G_{II}} = \frac{b}{4E_x\gamma}\left(\frac{\alpha}{I_1} + \frac{\beta}{I_2}\right)\left(\frac{3c-L}{c+L}\right)^2 \qquad c \geq \frac{L}{3} \tag{3.73}$$

where

$$\alpha = 1 + \frac{2.38}{a}\left(\frac{E_x}{E_z}\frac{h_1 I_1}{b}\right)^{1/4} + \frac{1.41}{a^2}\left(\frac{E_x}{E_z}\frac{h_1 I_1}{b}\right)^{1/2} \tag{3.74a}$$

$$\beta = 1 + \frac{2.38}{a}\left(\frac{E_x}{E_z}\frac{h_2 I_2}{b}\right)^{1/4} + \frac{1.41}{a^2}\left(\frac{E_x}{E_z}\frac{h_2 I_2}{b}\right)^{1/2} \tag{3.74b}$$

$$\gamma = (d_{11})_{AB} - (d_{11})_{BC} \tag{3.74c}$$

3.2.5 Numerical Illustrations for Cylinder DCB, ENF, and MMB Specimens

A computer program in MATLAB™ [49] was written and run, see Appendix D, to perform computations based on ply material properties listed in Table 3.2 and a temperature change, ΔT = Test temperature (T_{test}) – glass transition temperature (T_g), where T_{test}= 20°C and T_g = 120°C [50]. The results are listed in Table 3.4. Inspection of the data in Table 3.4 reveals that the thermal contribution G^{Th} to the energy release rate is very small compared to the critical value, G_c, for all lay-ups considered in the experiments. Consequently, we considered only the mechanical contribution to the energy release rate in the analysis and data reduction for fracture toughness of the DCB, ENF, and MMB specimens.

A parametric analysis was performed to examine the influences of elastic restraint and curvature ($1/R_i$) on C and G for 18 mm wide $[\pm 30]_n$ (n = 6,12) specimens assuming $h_1 = h_2 = H/2$ and a crack length of 30 mm. R_i is the internal radius of the cylinder, Fig. 3.13. The range of $1/R_i$ values in Table 3.5 covers the range from flat ($R_i = \infty$) to the curved DCB specimens (R_i = 80 mm) considered herein. The results in Table 3.5 show that the elastic restraint effect increases steeply with laminate thickness and is more significant for C than G. Table 3.5 also indicates that the influence of curvature on C and G is small for the range of curvatures examined and decreases with laminate thickness.

Table 3.4 Strain energy release rate due to residual thermal stresses, G^{Th}, for glass/epoxy laminates ($\Delta T = -100$ °C). H is the nominal total laminate thickness.

Lay-up	$[\pm 30]_6$	$[\pm 55]_6$	$[\pm 85]_6$	$[\pm 30]_{12}$	$[\pm 55]_{12}$	$[\pm 85]_{12}$
H, mm	6	6	6	12	12	12
G^{Th}, J/m^2	0.5	3.6	0.3	0.4	2.0	0.2

Table 3.5 Influence of curvature ($1/R_i$) on compliance and energy release rate for a $[\pm 30]_n$ laminate (n = 6,12). H is the total laminate thickness. C_∞ and G_∞ are the compliance and energy release rate given by the classical beam theory.

Specimen	H, mm	$1/R_i$, mm^{-1}	C/C_∞	G/G_∞
Flat	6	0	1.258	1.165
Curved	6	0.0125	1.271	1.173
Flat	12	0	1.562	1.345
Curved	12	0.0125	1.571	1.350

To examine the mode mixity for the cylinder laminates studied herein, calculations using ply properties in Table 3.2 and typical measured geometry parameters were performed on the glass/epoxy laminates considered in the experiments described in Chapter 4. Table 3.6 lists fracture mode ratios G_I/G_{II} for various ply angles and loading lever positions (c). For a given loading lever position and laminate thickness, the variation of G_I/G_{II} with ply angle is relatively small. Figure 3.22 illustrates the dependence of the dependence of mode ratio on crack length for the glass/epoxy angle-ply laminates. G_I/G_{II} remains almost constant when c = 28 mm. At larger values of c (c = 97 mm), the ratio G_I/G_{II} depends on thickness and lay-up, and decreases slowly with increased crack length.

Table 3.6 Dependence of mixed mode ratio G_I/G_{II} on ply angle θ at some fixed loading positions, c. H is the nominal total laminate thickness (a = 30 mm, b = 18 mm, $h_1 = h_2 = H/2$).

H, mm	6						12					
c, mm	28			97			28			97		
θ, deg.	30	55	85	30	55	85	30	55	85	30	55	85
G_I/G_{II}	0.31	0.30	0.30	4.40	4.27	4.26	0.35	0.33	0.33	4.90	4.64	4.63

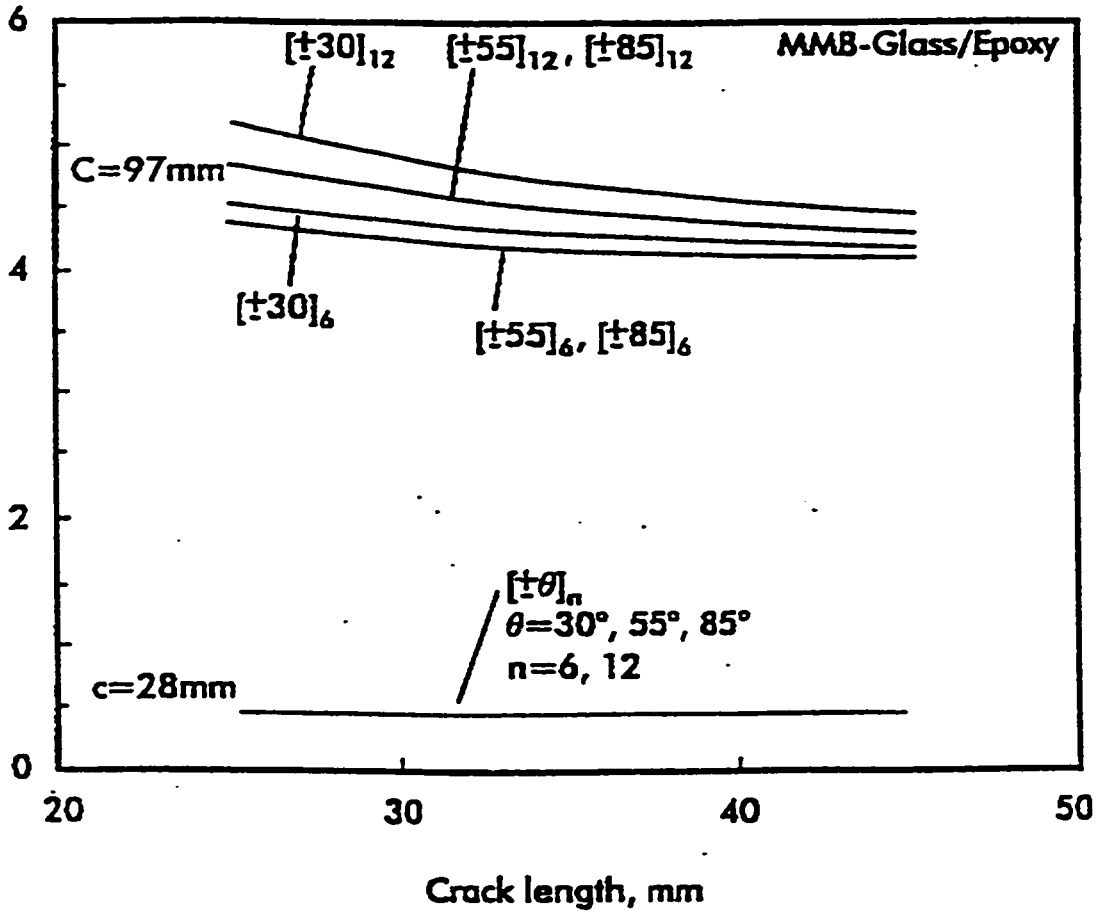

Fig. 3.22 Mode ratio G_I/G_{II} vs. crack length for glass/epoxy laminate MMB specimens with curved cross-section at two load positions (c = 28 and 97 mm).

Chapter 4 EXPERIMENTAL

4.1 Fracture Tests of Flat Glass/Polyester Laminate Beam Specimens

4.1.1 Materials and Specimens

Flat glass/polyester panels of $[0]_6$, $[\pm30]_5$, and $[\pm45]_5$ lay-ups were manufactured at the French Oceanographic Research Organization (IFREMER) using hand lay-up. A 58 mm long and 8 μm thick polypropylene film was inserted at the mid-plane of the panels during the lay-up process to define a starter delamination crack. Isophthalic polyester resin of density 1.18 g/cm^3 was obtained from Scott Bader (Ref. 489). E-glass fibers of density of 2.60 g/cm^3 in the form of quasi-unidirectional plies with 5% of fibers in the 90° direction were obtained from Vetrotex. The panels were cured at room temperature, and subsequently postcured at 90 °C for 3 hours to stabilize the resin. Measured fiber volume fraction was 45% from the burn-off test (ASTM D2584). The cured laminate thicknesses were nominally 4.4 and 7.3 mm for the quasi-unidirectional and angle-ply laminates, respectively. DCB, ENF, and MMB specimens of a nominal width of 20 mm were cut from the panels. Hinge load tabs were adhesively bonded to the DCB and MMB specimens following ASTM D5528. The initial crack lengths, a_o, of the DCB and MMB specimens, Figs. 3.3 and 3.7, were 33 ± 1 and 32 ± 1 mm, respectively. A crack length of 25 mm was used for the ENF specimens, Fig. 3.5.

Prior to fracture testing, basic mechanical property characterization of the quasi-unidirectional glass/polyester composite was performed by testing of 0° and 90° coupons according to standard test procedures [44]. Furthermore, three-point flexure testing [44] employing a linear voltage displacement transducer (LVDT) was conducted at various span lengths to obtain the flexural modulus E_{1f}. Mechanical ply properties are summarized in Table 3.1. The flexural modulus E_x and out-of-plane extensional modulus E_z for each lay-up were calculated from basic ply properties in Table 3.1 following the procedures outlined in Chapter 3; and the results are listed in Table 4.1. Notice that the full laminate has a flexural modulus different than that of the sub-laminates due to coupling effects. Table 4.1 also indicates that E_z increases slightly with lay-up angle.

4.1.2 Fracture Testing

Prior to fracture testing, one edge of the specimen was painted with white "liquid paper" to facilitate visual observation of crack initiation and crack length measurements. The initial crack tip position was also marked on the painted specimen edge.

The issue of precracking has, despite much research, not yet been fully resolved. While precracked specimens tend to produce more conservative toughness data than non-precracked [51,52], there remain unresolved problems with precracked specimens such as fiber bridging and the possibility for nonuniform crack fronts [20,21]. In the author's opinion, the most well defined and realistic situation corresponds to non-precracked specimens with thin insert films. Davies et al. [52], using the same insert thickness (13 μm) as in the present study, found an increase in G_{IIc} for unidirectional carbon/epoxy of

Table 4.1 Flexural and out-of-plane moduli, E_x and E_z, for glass/polyester laminates.

Lay-up	$[0]_6$	$[\pm 30]_5$	$[\pm 45]_5$
h, mm	2.19	3.65	3.65
E_z(full), GPa	8.5	9.37	9.85
E_x(full), GPa	34.7	20.8	12.8
E_x(sub), GPa	34.7	19.2	12.3

about 8% when non-precracked versus precracked specimens were used. The corresponding difference in fracture load is 4%. All fracture tests herein were performed from the end of the (straight) insert without precracking the specimen.

A minimum of three replicate specimens per each lay-up were successfully tested. All testing was performed in a displacement controlled Tinius-Olsen DS-50 test frame, Fig. 4.1. Figure 4.2 shows fracture testing of a glass/polyester DCB specimen. The ENF specimens were positioned in a standard three-point flexure fixture to achieve a span length, 2L, of 100 mm between the supports, Fig. 3.5, and a crack length, a, of 25 mm. The MMB specimens were loaded in a MMB test fixture, Fig. 3.7. Load positions, c, of 28, 42, and 97 mm, see Fig. 3.7, were employed. The corresponding mixed mode G_I/G_{II} ratios are listed in Table 4.2. A cross-head speed of 0.76 mm/min allowed visual monitoring of crack propagation. Displacement of the cross-head was measured with a linear voltage differential transducer (LVDT), and the real-time load (P) versus displacement (δ) response was recorded on a x-y plotter. The onset of crack growth from the starter insert was determined by inspection of the specimen edge with a Wild 820 travelling microscope of 20x magnification, Fig. 4.1, and by observation of the P-δ curve. As observed in fracture testing of multi-directional laminates by previous researchers [32-34,53,54], the crack may not remain at the interface defined by the insert after onset of crack propagation. Such behavior will influence the fracture resistance and invalidate fracture mechanics and invalidate fracture mechanics analysis based on the assumption of collinear crack growth.

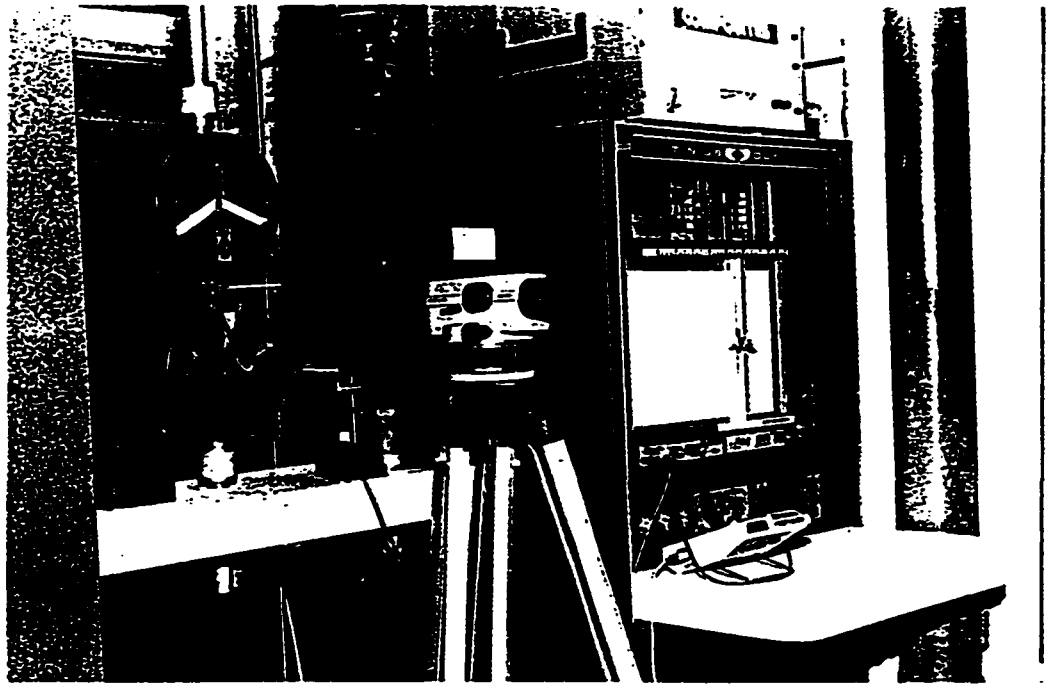

Fig. 4.1 Fracture testing set-up.

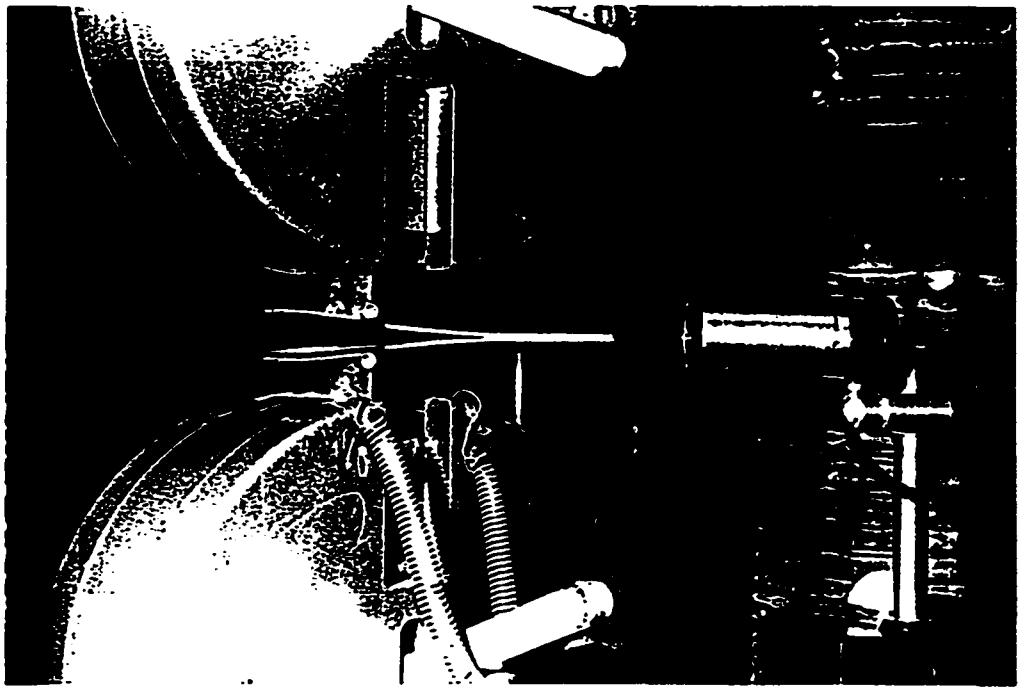

Fig. 4.2 Fracture testing of a glass/polyester DCB specimen.

Table 4.2 Mixed-mode ratios considered in the analysis and experiments with glass/polyester MMB specimens (L = 50 mm, b = 20 mm, a = 32 mm).

Parameter	$[0]_6$			$[\pm30]_5$			$[\pm45]_5$		
h,mm	2.19			3.65			3.65		
β, Nmm	9.05×10^4			24.1×10^4			15.3×10^4		
Load position c, mm	28	42	97	28	42	97	28	42	97
G_I/G_{II}	.28	1.02	4.01	.27	.97	3.84	.28	1.01	3.97

Therefore, the crack growth behavior was continuously monitored during the DCB, ENF, and MMB fracture tests using the traveling microscope to detect any crack jumping from the initial mid-plane and to identify and examine the fracture mechanisms.

Fracture testing of the DCB specimen was performed using an incremental test method. Each DCB specimen was loaded at a constant displacement rate until the crack propagated between 5 to 10 mm. The cross-head was then stopped. After the crack growth arrested completely, the new crack tip was marked on the specimen edge with the aid of the travelling microscope, and crack length was measured directly with a high resolution ruler and recorded on the x-y chart. The specimen was then unloaded and loaded again, and the onset of crack growth was marked with a circle on the load-displacement chart to indicate the corresponding critical load and displacement values for the previously measured crack length. The crack extension process was then repeated in about 10 mm increments until the final crack length reached approximately 80 mm beyond the load application point. This procedure yields several fracture toughness values for each specimen, and reliable compliance data for each crack length.

4.1.3 DCB Tests of Flat Glass/Polyester Laminate Beam Specimens

4.1.3.1 Data Reduction for Fracture Toughness

The elastic foundation (EF) model analysis developed in Chapter 3 will be employed to reduce the fracture toughness defined as the critical energy release rate, G_c, from the experimental data. Prior to fracture testing, basic ply properties (Table 3.1) and DCB specimen dimensions (length, width and thickness) were measured. Then, following

the procedures outlined in detail in Chapter 3, the moduli, E_x and E_z, were calculated from basic ply properties. Then, energy release rate per square of applied load, G/P^2, was calculated for each specimen as a function of crack length using eq. (3.12). To determine fracture toughness at any given crack length, the critical load P_c corresponding to the onset of crack growth was measured in a DCB fracture test and substituted in the G/P^2 relation at that crack length.

In addition to the evaluation of fracture toughness, G_c, from the EFM, the experimental compliance method [12] was used. Compliance of the DCB specimen was measured at various discrete crack lengths. The compliance was evaluated from the slope of the initial linear region of the load-displacement (P-δ) curve. The method of least squares was used to curve fit the compliance versus crack length data to a power function so as to obtain the parameters R and n in the expression proposed by Berry [55]:

$$C = R a^n \tag{4.1}$$

The energy release rate, G, is obtained by substituting eq. (4.1) into eq. (2.44). G_c is obtained by substitution of the measured critical load P_c at the onset of crack advance into the expression,

$$G_c = \frac{P_c^{\,2}\, n\, R\, a^{n-1}}{2b} \tag{4.2}$$

4.1.3.2 Compliance Predictions

To examine the validity of the compliance predictions from the elastic foundation model, eq. (3.11), a comparison was made with experimental results on the quasi-unidirectional and angle-ply glass/polyester laminates under consideration. The basic extensional ply properties listed in Table 3.1 and test geometry parameters measured prior to fracture tests were used in the compliance calculation. Calculated E_x and E_z values are listed in Table 4.1. Compliance of the DCB specimen was evaluated from experimental load-displacement (P-δ) curves at various crack lengths. Figure 4.3 shows representative experimental data and predicted ("EFM") compliances for the unidirectional and angle-ply laminate DCB specimens. The predictions are overall in good agreement with the experimental data although the EFM predicts less compliance than measured experimentally for the $[\pm 45]_5$ laminate, Fig. 4.3c. Such a discrepancy may possibly be due to matrix yielding and/or matrix cracking in the flexure loaded arms of the relatively weak $[\pm 45]_5$ laminate. Overall, predictions are in agreement with experimental results, which supports the viability of the beam model for analysis of laminate DCB specimens.

4.1.3.3 Fracture Test Results

Figure 4.4 shows representative load-displacement (P-δ) curves for the $[0]_6$, $[\pm 30]_5$, and $[\pm 45]_5$ DCB specimens. It should be pointed out that the first P-δ curve in each case represents crack growth directly from the insert film. The circles on the graphs

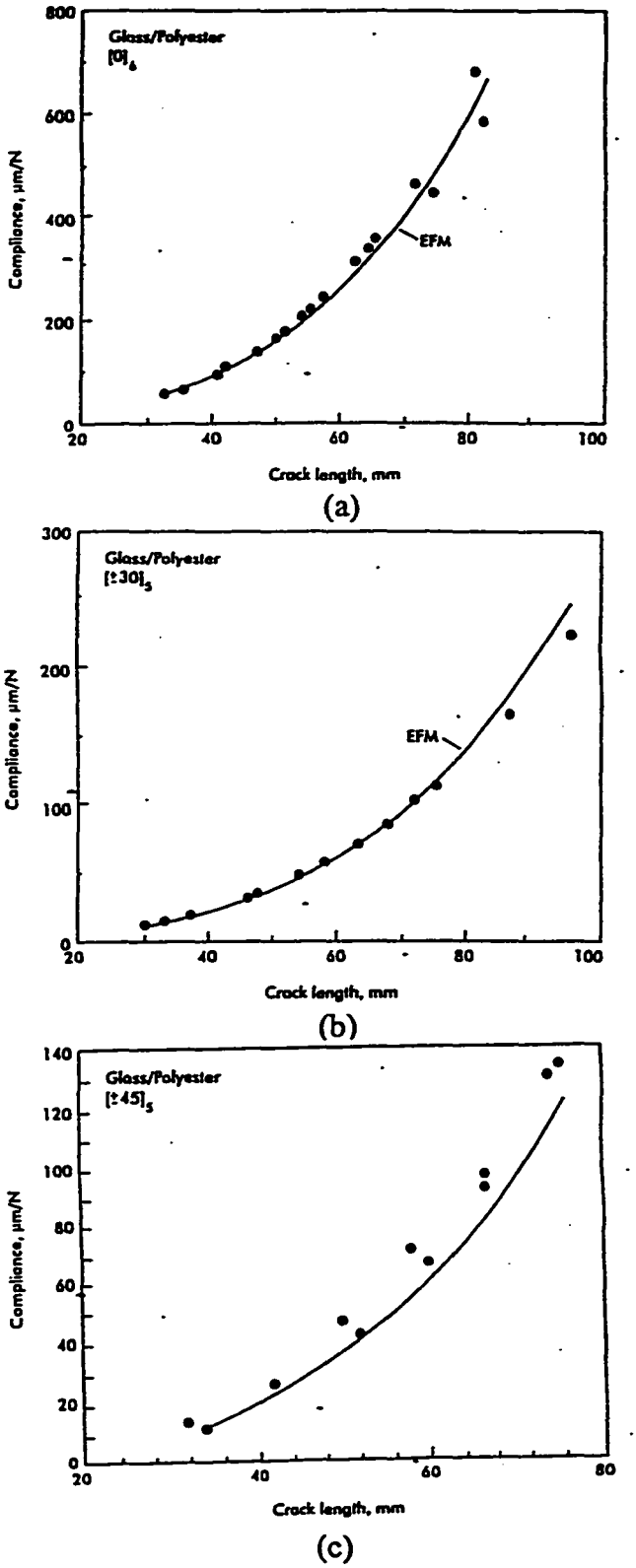

Fig. 4.3 Calculated (EFM) and experimental compliance versus crack length curves for glass/polyester DCB specimens, a) $[0]_6$, b) $[\pm 30]_5$, c) $[\pm 45]_5$.

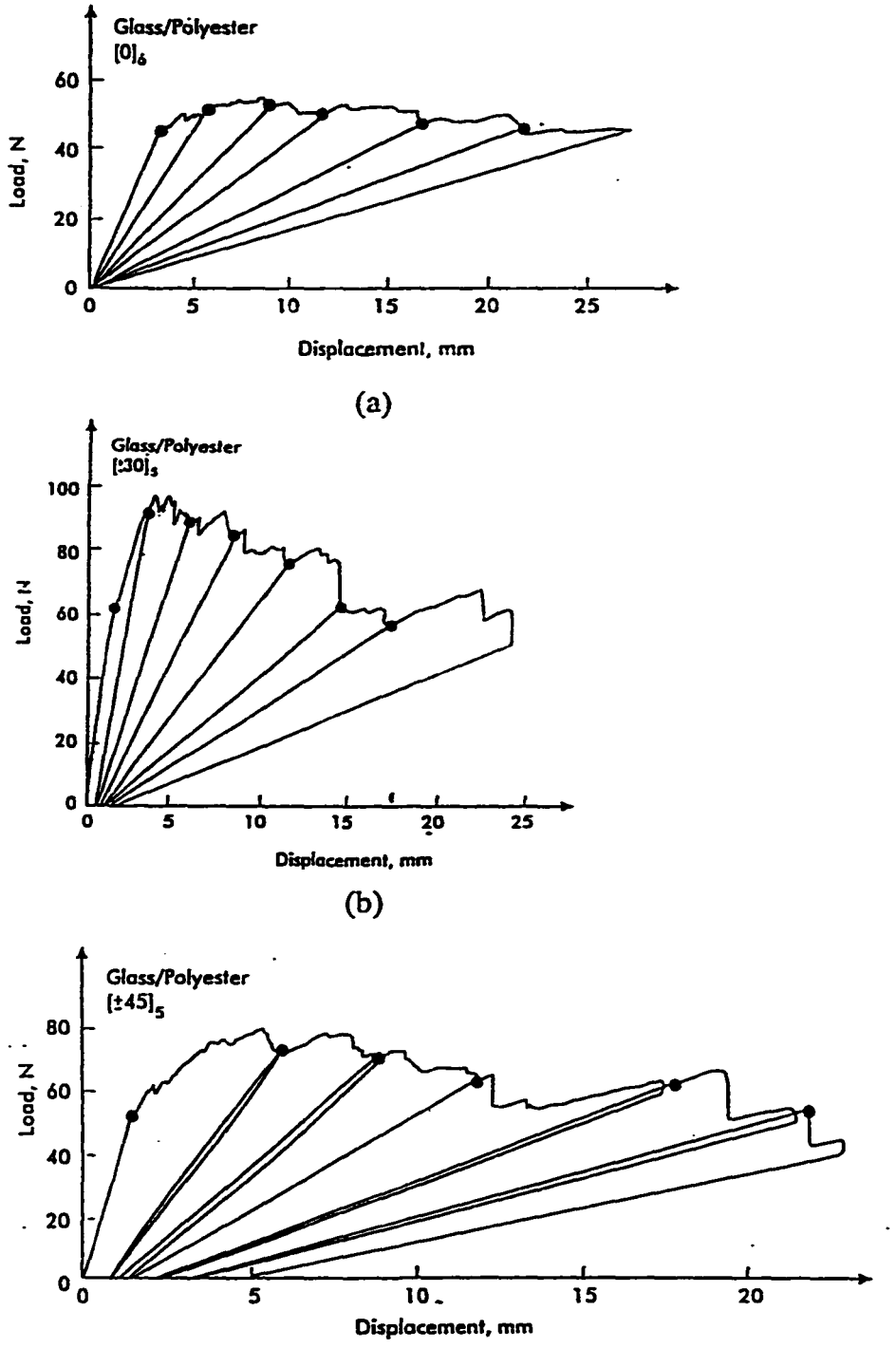

Fig. 4.4 Representative load-displacement (P-δ) curves for glass/polyester DCB specimens, a) $[0]_6$, b) $[\pm 30]_5$, c) $[\pm 45]_5$.

indicate the onset of crack propagation as observed from the edge with a travelling microscope. For the $[0]_6$ laminate, Fig. 4.4a, it is observed that the onset of crack growth occurred close to or at the maximum load for each crack growth increment after the first increment. The response is essentially linear elastic as also evidenced by the negligible permanent deformation upon unloading. The crack propagated in a stable manner during the displacement controlled fracture testing. For the angle-ply laminates, Figs. 4.4b and 4.4c, the P-δ curves indicate oscillations in the fracture load and occasional stick-slip crack growth that are attributed to the fracture resistance associated with crack growth around the transverse bundles. When the crack intersected a transverse fiber yarn, it was observed to partially debond, corresponding to crack branching, and ends of the fiber yarns bridged the sub-laminates as illustrated in Fig. 4.5. Similar behavior was also observed in mode I delamination fracture of orthogonal woven fabric carbon/epoxy composites [56]. Comparison of the load levels at a given displacement shows that crack propagation in the angle-ply laminates occurred at larger loads than in the quasi-unidirectional laminate, but it should be kept in mind that the angle-ply laminates are substantially thicker than the quasi-unidirectional laminate (7.3 vs. 4.4 mm). Figure 4.4 also shows that the angle-ply laminates showed quite linear P-δ response prior to crack propagation, although the permanent deformation remaining after unloading reveals that plastic yielding or possibly matrix cracking occurred, especially for the $[\pm 45]_5$ laminate.

For all laminates, the crack growth initiated and remained at the specimen mid-plane corresponding to the $\pm\theta$ interface. This is in contrast to previous reports on DCB

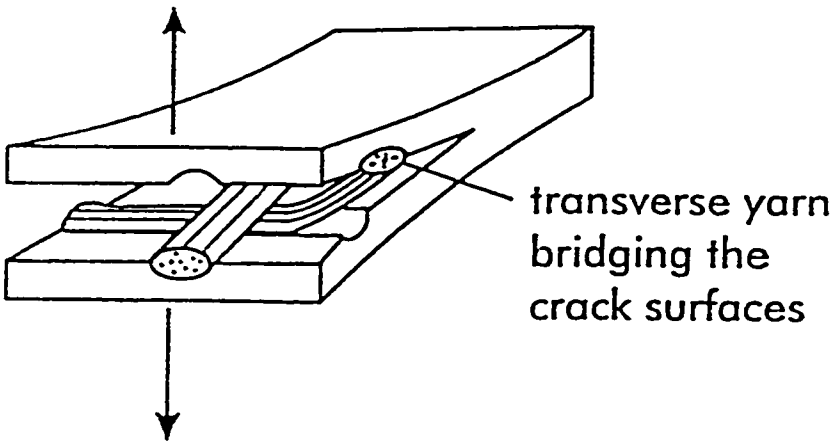

Fig. 4.5 Schematic illustration of transverse yarn debonding and bridging during DCB testing of glass/polyester laminates.

testing of multidirectional laminates. Robinson and Song [34], for example, reported that the crack propagated along the intended specimen mid-plane only in unidirectional laminates (θ=0°). For other values of θ the crack jumped to other interfaces after some increment of crack growth. In addition, fiber pull-out and fiber breakage are commonly observed in such laminates [34,57].

Because of plasticity influence, linear elastic fracture mechanics (LEFM) is not strictly applicable to the $[\pm 45]_5$ laminate specimens. However, since the response prior to crack propagation is essentially linear, the fracture toughness values were determined from the compliance and critical load recorded at each crack length. This procedure thus considers only the updated linear response at each crack length and neglects accumulated plasticity effects. Such an approach is expected to provide more conservative fracture toughness than nonlinear methods such as the J-integral approach [58-60]. Fracture toughness, G_C, was reduced at each crack length from the P-δ curves using the EFM and experimental compliance method. Figure 4.6 shows representative resistance curves (R-curves) for the quasi-unidirectional and angle-ply laminates. The EFM produces similar resistance curves as the empirical Berry compliance calibration method as would be expected from the previously reported accurate compliance predictions, Fig. 4.3. All laminates display rising R-curve behavior. The rising R-curves are attributed to toughening caused by debonding of transversely oriented yarns in the quasi-unidirectional plies, see Fig. 4.5, and fracture of bridged fibers. For the $[0]_6$ laminate, the propagation toughness continuously increased with crack length, Fig. 4.6a, whereas, for

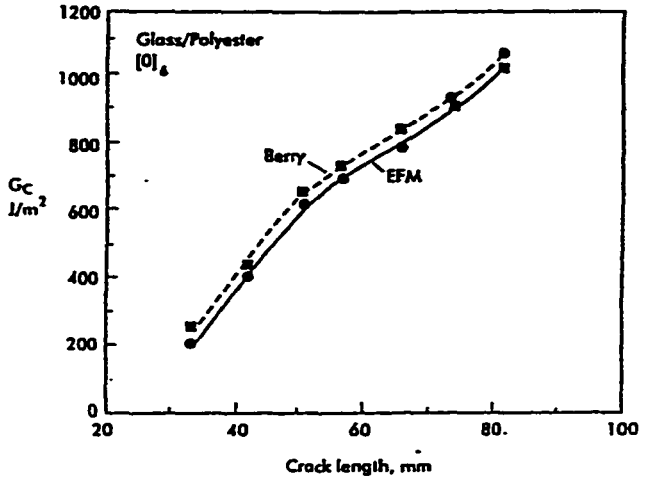

(a)

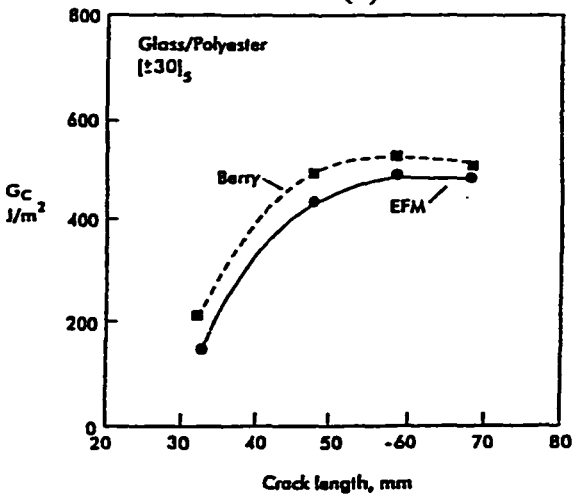

(b)

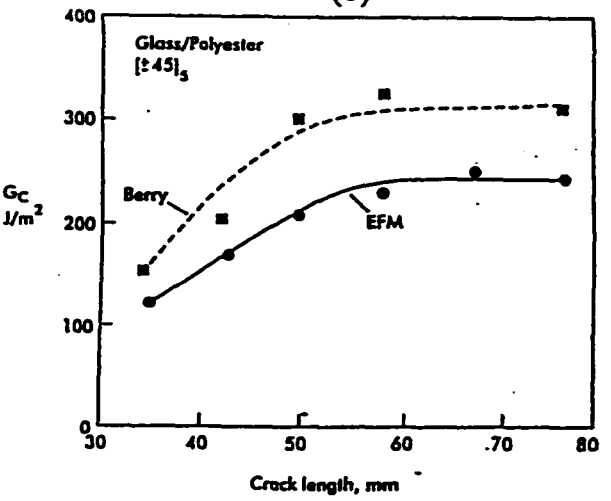

(c)

Fig. 4.6 Fracture resistance curves for glass/polyester DCB specimens, a) $[0]_6$, b) $[\pm 30]_5$, c) $[\pm 45]_5$.

the angle-ply laminates, steady-state crack growth occurred after a crack length of about 50-60 mm, Figs. 4.6b and 4.6c.

The mechanics of fiber bridging in DCB specimens have been demonstrated theoretically by Suo et al. [45] and experimentally by Spearing and Evans [61]. They demonstrated that the relatively weak pull-out tractions from the bridged debonded fibers may substantially elevate the fracture resistance for a propagating crack. The shape of the resistance curve is influenced by two major factors, viz. the traction law exerted by the bridging fibers and the crack opening behind the crack tip which in turn is governed by the flexural stiffness of the arms of the DCB specimen. The shapes of the resistance curves for the composites examined herein, Fig. 4.6, indicate a mechanism where fibers and/or fiber bundles break away from the crack plane and subsequently pull out from the matrix resembling "strain softening" [45,61]. The R-curves, however, do not represent a material property because of the thickness effect. Thick composites would require longer crack lengths to attain a steady state resistance. This effect makes comparison between the resistance curves for the DCB specimens examined herein cumbersome because of their different bending rigidities.

The initiation and steady-state fracture toughness values obtained using experimental compliance calibration are listed in Table 4.3. It is noted that the initiation toughness decreases with ply angle θ. The $[\pm 45]_5$ laminate showed the smallest initiation and propagation toughnesses. Polaha et al. [53] performed DCB tests on graphite/epoxy

Table 4.3 Initiation and steady-state values of fracture toughness.

	$[0]_6$	$[\pm 30]_5$	$[\pm 45]_5$
G_C (init.) J/m^2	282 ± 42	214 ± 14	176 ± 32
G_C (SS) J/m^2	N/A	500	300

laminates and examined the delamination resistance of 0°/0°, 15°/15°, ±15°, 30°/30°, and ±30° ply interfaces. They also found that the R-curves became steeper and that initiation and propagation values of G_c decreased with increased lay-up angle.

To examine the possibility of nonuniform crack extension, the non-dimensional parameters, d_c and s, defined in Chapter 2, eqs. (2.45) and (2.46), were calculated for the sub-laminates of the cracked region of the DCB specimen from measured ply properties, Table 3.1. The results are summarized in Table 4.4. d_c and s increase with increasing off-axis angle indicating tendency for nonuniform crack extension. For all lay-ups considered, however, d_c is below the "upper bound" limit of 0.25 for mode I dominated crack growth as suggested by Davidson et al. [26]. The skewness parameter, s, is non-zero for the angle-ply laminates indicating that the crack may propagate in a skewed manner [21]. In order to monitor the interlaminar crack front during fracture testing, some DCB specimens were unloaded, removed from the grips, and black India ink was injected into the crack between the two sub-laminates. Then the specimen was examined under an intense light source and the crack front was marked. The specimen was reloaded and the same procedure was repeated after each crack increment. Figure 4.7 shows representative crack front shapes for the various lay-ups examined. As predicted from Table 4.4, all fracture specimens exhibited nonuniform crack fronts after growth from the straight insert. The larger energy release rate at the center of a DCB specimen [21,26] is reflected by further crack extension at the center than at the edges. The crack front shape remained approximately independent of the crack length. This behavior is

Table 4.4 Laminate parameters characterizing nonuniform distribution of energy release rate and interlaminar crack growth.

Lay-up	Sub $[0]_6$	Sub $[\pm 30]_5$	Sub $[\pm 45]_5$
d_c	0.018	0.151	0.225
s	0	0.194	0.236

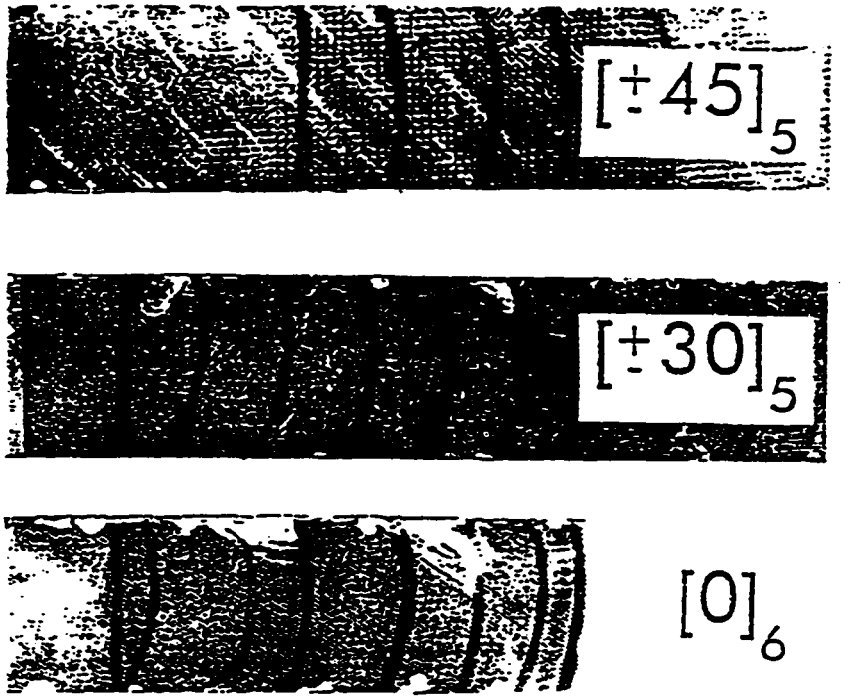

Fig. 4.7 Crack front shapes for glass/polyester DCB specimens. Crack propagated from the initial straight front on the left.

expected since the parameters, d_c and s, are dependent only on sub-laminate elastic stiffnesses and, furthermore, the crack remained at the mid-plane. Although the parameters d_c and s are quite dispersed for the lay-ups considered, Table 4.4, the crack front shapes appear quite similar. More accurate experiments and detailed modeling are required to examine this feature in more detail.

4.1.4 ENF Tests of Flat Glass/Polyester Laminate Beam Specimens

4.1.4.1 Compliance Predictions

To examine the validity of the compliance predictions from eq. (3.27), a comparison was made with experimental results on the unidirectional and angle-ply E-glass/polyester laminates under consideration. The basic extensional ply properties listed in Table 3.1 and test geometry parameters (laminate thickness (h), width (b), crack length (a)) were used in the calculations. Experimental details are provided in the next section. Table 4.5 presents experimental and predicted compliances for the ENF specimens considered. The predictions are overall in good agreement with experimental data. The discrepancies between predicted and measured compliances of the specimens may be due to a nonuniform distribution of fiber volume fraction through the thickness that would influence the flexural properties. This explanation is supported by the lower flexural modulus than extensional modulus of the unidirectional laminate, see Table 3.1. The thickness-to-span length ratio (h/L) is 0.073 or less for the laminates examined experimentally. For such laminates the classical plate theory (CPT) prediction of the ENF specimen compliance [26] would be only slightly less (< 5%) than the current SBT predictions, eq. (3.27), but this difference would remove the CPT predictions further from

Table 4.5 Comparison of predicted (SBT) and experimental compliances for glass/polyester ENF specimens (a=25mm, L=50mm, b=20mm).

Lay-up	C^{SBT} (10^{-6} m/N)	C^{exp} (10^{-6} m/N)
$[0]_6$	5.13	5.90±0.24
$[\pm 30]_5$	1.92	2.20±0.05
$[\pm 45]_5$	3.07	2.90±0.20

the experimental data. The data in Table 4.4, however limited, tends to support the applicability of the SBT formulation for evaluation of experimental fracture toughness data from laminate ENF specimen tests.

4.1.4.2 Fracture Test Results

Representative load-displacement curves for the quasi-unidirectional and angle-ply ENF specimens are shown in Figs. 4.8. The filled circle on the graphs marks the point where onset of crack propagation was visually observed. For some specimens both edges were observed after some small increment of stable crack growth was detected on the front edge. The load-displacement (P-δ) record for the quasi-unidirectional $[0]_6$ laminate is linear until very close to fracture, Fig. 4.8a. It was observed that the unstable crack growth, inherent of the ENF geometry, was arrested when the crack intersected a transversely oriented fiber yarn located at the crack interface in the quasi-unidirectional lay-up. At this point, the fiber yarn was observed to partially debond, corresponding to crack branching and fiber yarn bridging of the sub-laminates. The angle-ply $[\pm 30]_5$ laminates also showed quite linear P-δ response during loading, see Fig. 4.8b, although permanent deformation remaining after unloading indicates that some plastic yielding occurred. Similar to the $[0]_6$ specimens, the unstable crack growth in the $[\pm 30]_5$ laminate was arrested by large-scale transverse fiber yarn debonding, Fig. 4.5, which reduced the tendency for unstable delamination growth.

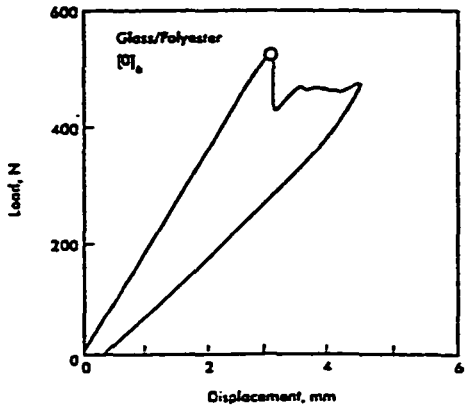

(a)

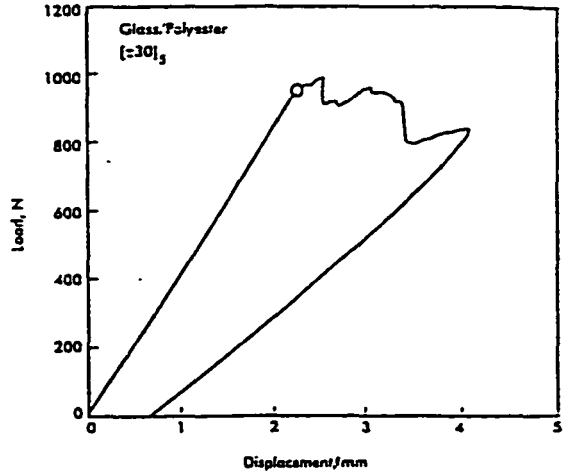

(b)

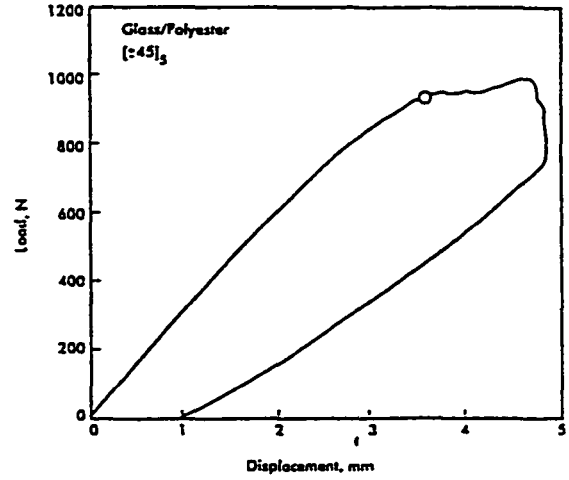

(c)

Fig. 4.8 Representative load-displacement (P-δ) curves for glass/polyester ENF specimens, a) $[0]_6$, b) $[\pm 30]_5$, c) $[\pm 45]_5$.

Significant nonlinearity of the load-displacement behavior was observed during loading, and a large permanent deformation was observed after unloading of the $[\pm 45]_5$ specimens, see Fig. 4.8c. These observations are attributed to plastic deformation of the specimen due to matrix shear yielding. Due to this large-scale plasticity, the application of linear elastic fracture mechanics (LEFM) to the $[\pm 45]_5$ laminates is questionable. Although there are other more appropriate methods to calculate the fracture toughness for cases where nonlinearities are present [58-60], such methods are considered outside the scope of this research. The LEFM approach should provide a conservative estimate of fracture toughness.

The shear deformation laminated beam theory (SBT) analysis will be employed to reduce the fracture toughness, G_c, from the experimental data. Prior to fracture testing, basic material properties (Table 3.1) and specimens dimensions (length, width, thickness, and crack length) were measured. Following the procedure outlined in detail in Chapter 3, the effective bending compliance, d_{11}, for the cracked and uncracked regions of each specimen were calculated from basic ply properties. Hence, energy release rate per square of applied load, G/P^2, was determined from eq. (3.28) for each specimen prior to fracture testing. To determine G_c, the critical load P_c corresponding to the onset of crack growth was measured in an ENF fracture test and substituted in the G/P^2 relation. Table 4.6 lists fracture toughness data obtained from the ENF tests. The large scatter in G_c may be due to the influence of transverse reinforcements on the critical load. When the crack tip intersects a transverse fiber bundle, the crack branches into paths around the bundle that

Table 4.6 Fracture toughness values of glass/polyester ENF specimens.

Lay-up	G_c (J/m^2)
$[0]_6$	496±135
$[\pm30]_5$	976±71
$[\pm45]_5$	1485±158

would increase the crack growth resistance over that of a truly unidirectional composite. The angle-ply laminates showed much higher crack growth resistance than the unidirectional laminates. This trend is in contrast to the minor variations of apparent mode II fracture toughness for non-precracked graphite/epoxy ENF specimens with 0°/0°, ±15° and ±30° interfaces found by Polaha et al. [53]. Shi et al. [62] examined the mode II fracture of carbon/epoxy and glass/epoxy composite with ±θ interface plies. Similar to Polaha et al. [53], they found that the fracture toughness did not show much dependence on the interply angle. It is believed that the present increasing trend is largely explained by the toughening caused by debonding of transversely oriented yarns in the quasi-unidirectional plies. The angle-ply laminates displayed more yarn debonding than the quasi-unidirectional laminate.

As discussed in Chapter 1, the laminates examined may display nonuniform crack propagation. In order to monitor the interlaminar crack front after a fracture test, black India ink was injected into the crack between the two sub-laminates. Then the specimen was examined under an intense light source and the crack front was marked. As predicted from Table 4.4 the initially straight crack grew non-uniformly, see Fig. 4.9. The larger energy release rate at the edges of an ENF specimen as predicted by Davidson et al. [26] is reflected by further crack extension at the edges than at the center.

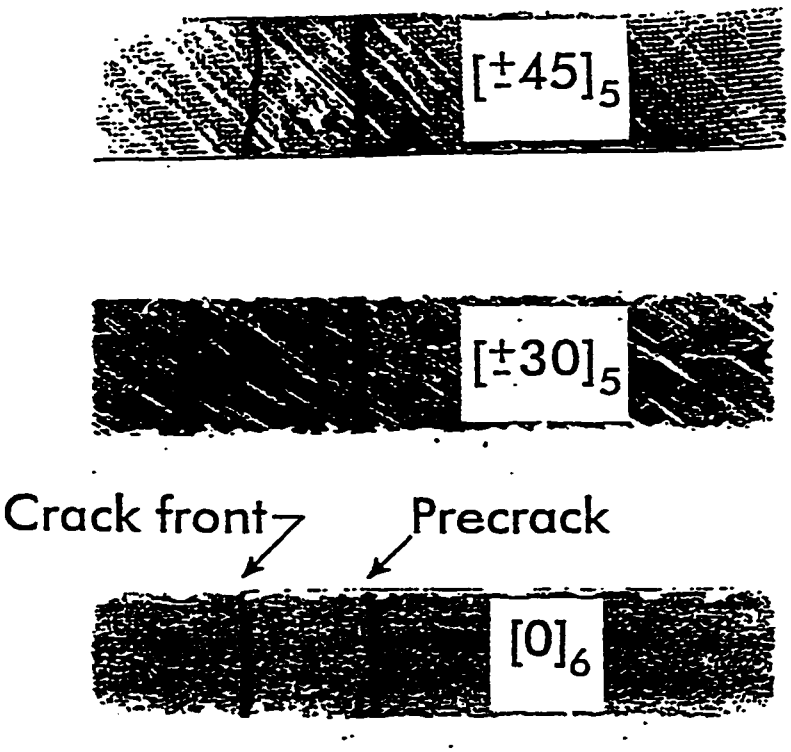

Fig. 4.9 Photographs of initial crack front defined by insert film and crack front after propagation for glass/polyester ENF specimens. Crack propagated from right to left.

4.1.5 MMB Tests of Flat Glass/Polyester Laminate Beam Specimens

4.1.5.1 Compliance Predictions

To examine the validity of the compliance predictions from the beam model, eq. (3.34), a comparison was made with experimental results on the quasi-unidirectional and angle-ply glass/polyester laminates under consideration. The basic extensional ply properties listed in Table 3.1 together with the required geometry parameters were substituted in the MMB compliance expression. The experimental compliance was evaluated from the slope of the initial linear region of the load-displacement (P-δ) curves. Table 4.7 presents experimental and predicted compliances for the quasi-unidirectional and angle-ply laminate MMB specimens. It is noted that the compliance increases with increased ratio G_I/G_{II} for all laminates. The predictions are overall in close agreement with the experiments although the predictions for the quasi-unidirectional laminate are somewhat stiff which may be due to a nonuniform fiber volume fraction in these laminates. As mentioned earlier, such an explanation is supported by the lower flexural modulus than extensional modulus, Table 3.1. The overall agreement with the experimental data, however, supports the viability of the beam model.

4.1.5.2 Fracture Test Results

Figures 4.10 shows representative load-displacement (P-δ) curves for the quasi-unidirectional and angle-ply MMB laminate specimens. The circles on the graphs indicate the onset of crack propagation as observed with a traveling microscope. For the quasi-unidirectional $[0]_6$ laminate, Fig. 4.10a, indicates a slight load decrease after the

Table 4.7 Measured (EXP) and calculated (BT) (a = 32 mm) MMB compliance data.

Lay-up	$[0]_6$			$[\pm30]_5$			$[\pm45]_5$		
G_I/G_{II}	0.28	1.02	4.01	.27	.97	3.84	.28	1.01	3.97
C^{EXP} μm/N	20.3 ±1.0	38.5 ±9.6	135 ±14.3	7.5 ±0.5	11.3 ±0.1	46.2 ±4.7	11.5 ±0.1	17.0 ±2.8	70.2 ±9.6
C^{BT} μm/N	17.2	33.6	123	6.4	11.4	49.0	10.8	18.0	79.3

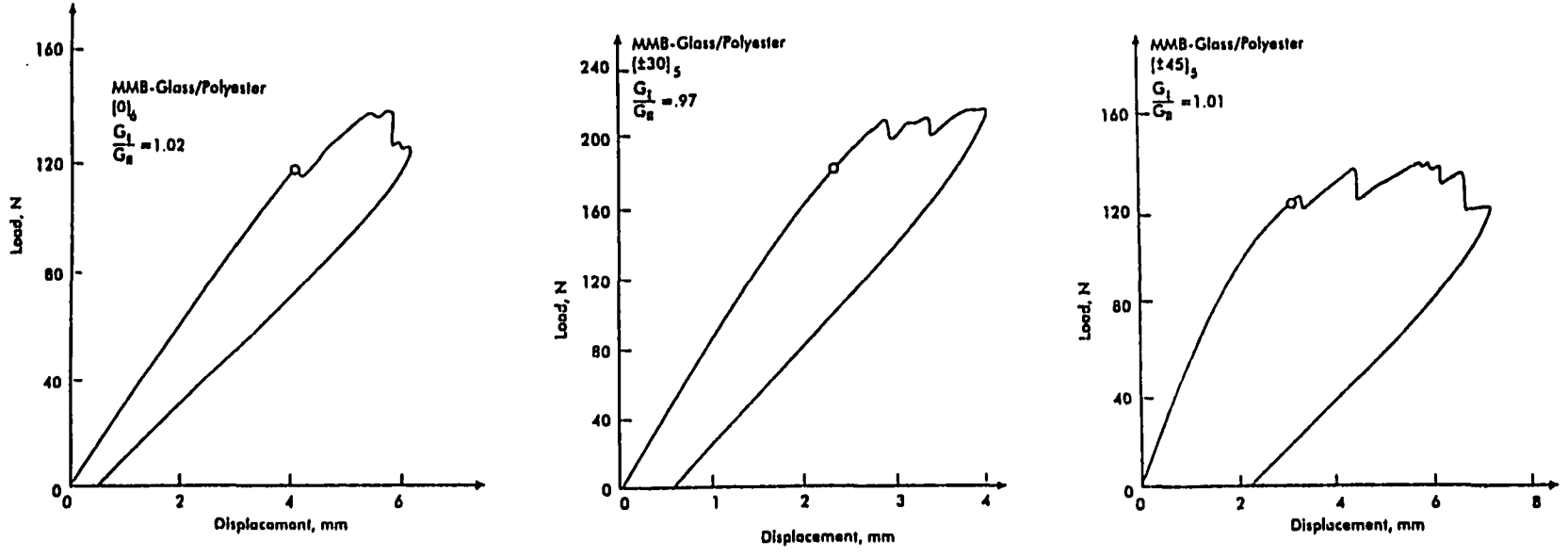

Fig. 4.10 Representative load-displacement (P-δ) curves for glass/polyester MMB specimens, a) $[0]_6$, b) $[\pm 30]_5$, c) $[\pm 45]_5$.

crack began propagating. After this slight decrease in load, the load increased with further crack propagation evidencing stable crack growth and R-curve behavior. Slight nonlinear load-displacement response was noted prior to the onset of crack propagation and a small permanent displacement remained after unloading of the MMB specimen. Fracture tests of the $[0]_6$ laminate at larger mode II fractions (G_{II}/G) revealed increased nonlinear response. Figures 4.10b and 4.10c show that the angle-ply laminates showed nonlinear P-δ response prior to crack propagation. The nonlinearity increased with increased ply angle and decreased ratio G_I/G_{II}. The permanent deformation remaining after unloading indicates that yielding and possibly matrix cracking occurred, especially for the $[\pm 45]_5$ laminate, Fig. 4.10c. Nonlinear P-δ behavior was also observed in the above ENF tests of the $[\pm 45]_5$ laminate. The P-δ curves for all lay-ups show oscillations in the fracture load and occasional stick-slip crack growth after the onset of crack growth. As discussed earlier for the flat DCB specimens, these phenomena are attributed to the fracture resistance associated with crack growth around the transverse bundles, as shown in the schematic in Fig. 4.5. The tendency for unstable crack growth after the onset of delamination increased with decreasing G_I/G_{II} ratio. For all laminates, the interlaminar crack remained at the specimen mid-plane at the $+\theta/-\theta$ interface as was also observed in the ENF and DCB tests of these laminates.

The laminated beam theory analysis will be employed to reduce the mixed mode fracture toughness, G_c, from experimental data. Prior to fracture testing, basic ply properties and MMB specimen dimensions (length, width, thickness, crack length) are

measured. Following the procedures described in Chapter 3, the effective bending compliance, d_{11}, for the cracked and uncracked regions of each specimen, and the out-of-plane extensional modulus, E_z, are calculated from basic (on-axis) ply properties, Table 3.1. Energy release rate per square of applied load, G/P^2, is then calculated from eq. (3.30) for each specimen. To determine G_c, the critical load P_c corresponding to the onset of crack growth is measured in a MMB fracture test and substituted in the G/P^2 relation.

As observed in Fig. 4.10, the P-δ curves displayed substantial nonlinear behavior prior to crack growth, and linear elastic fracture mechanics (LEFM) is not strictly applicable for data reduction of fracture toughness. Since nonlinear fracture mechanics analysis methods are considered outside the scope of this research and for consistency with our previous DCB and ENF tests of these laminates, the fracture toughness was determined from the elastic properties of the laminates and the critical load at onset of crack propagation. Table 4.8 lists the fracture toughness data, G_c, obtained from the MMB tests. For completeness, G_c values measured in the ENF and DCB tests of the glass/polyester laminates are included in Table 4.8. For all lay-ups, G_c increased when G_I/G_{II} decreased. This result was expected since G_{IIc} is much larger than G_{Ic} for these laminates. A very large difference between G_{Ic} and G_{IIc} was also observed for a hand laid-up unidirectional glass/epoxy composite by Ducept et al. [63]. Figure 4.11 shows G_c plotted versus the mode II fraction, G_{II}/G. Overall, G_c increases with increased mode II fraction and ply angle. The G_c curves for all lay-ups increase rapidly when $G_{II}/G > 0.7$ as

Table 4.8 Initiation values of mixed mode fracture toughness for glass/polyester MMB specimens.

Lay-up	$[0]_6$					$[\pm30]_s$					$[\pm45]_s$				
G_I/G_{II}	0 (ENF)	.28	1.02	4.01	∞ (DCB)	0 ENF	.27	.97	3.84	∞ (DCB)	0 (ENF)	.28	1.0 1	3.97	∞ (DCB)
G_c(init.) J/m^2	496 ±135	365 ±22	311 ±45	293 ±38	282 ±42	976 ±71	471 ±55	335 ±18	312 ±68	214 ±14	1485 ±158	500 ±40	386 ±22	348 ±27	176 ±32

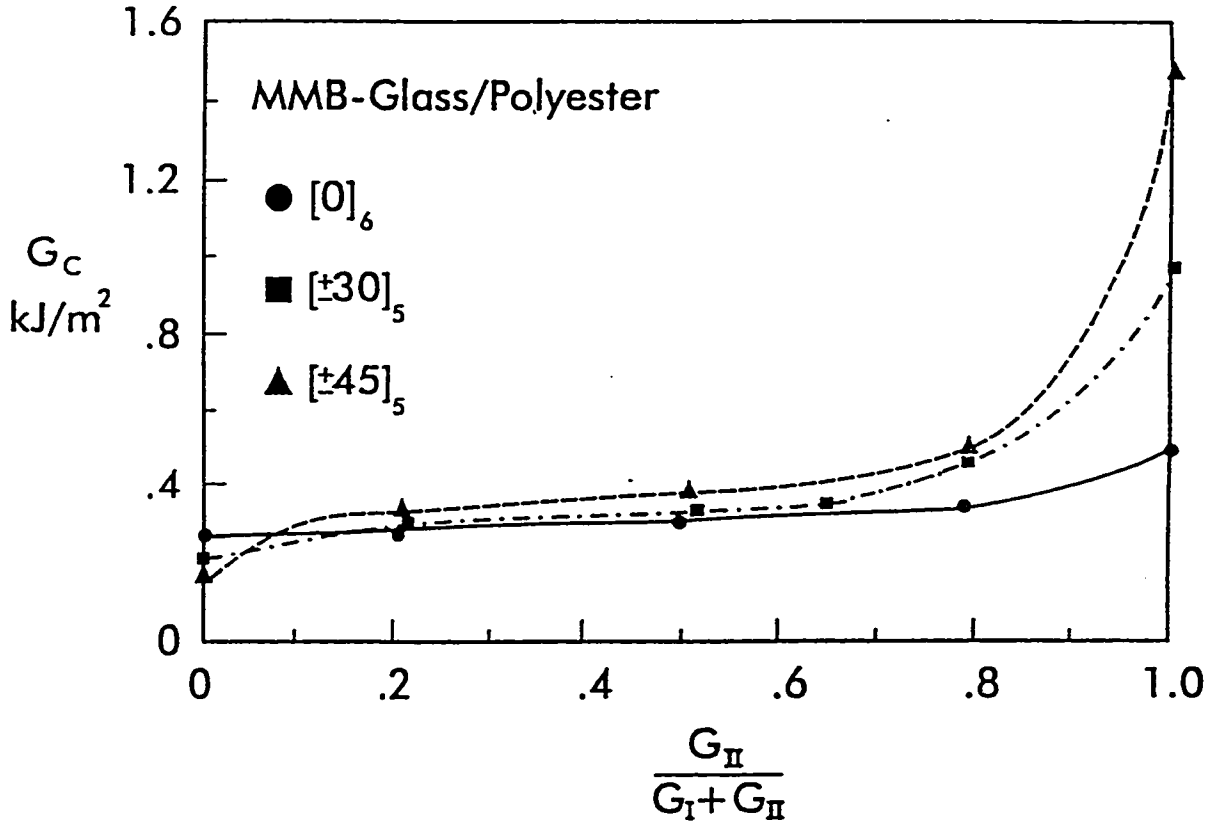

Fig. 4.11 Fracture toughness G_c versus mode II fraction for glass/polyester MMB specimens.

the mode II fracture toughness is approached. A similar trend was observed for unidirectional glass/epoxy by Benzeggagh and Kenane [64].

Although the parameters d_c and s, eqs. (2.45) and (2.46), are defined for far-field mode I and mode II loadings, they have significance also for the MMB test. The discussion in Chapter 1 on the shapes of the crack fronts in DCB and ENF tests would indicate a more uniform distribution of energy release rate across the MMB specimen width because of superposition of two opposite effects. As a result, a more uniform crack propagation would be expected in the MMB test than in the DCB and ENF tests.

In order to monitor the interlaminar crack front after a fracture test, some MMB specimens were unloaded after a certain increment of crack growth, and black India ink was injected at the crack front between the two sub-laminates. The specimens were examined under an intense light source and the crack front was marked on each specimen. Figure 4.12 shows examples of crack fronts in $[0]_6$, $[\pm 30]_5$ and $[\pm 45]_5$ MMB specimens. As predicted from Table 4.4, all fracture specimens exhibited nonuniform crack fronts after growth from the straight insert, see Fig. 4.12. Also, the angle-ply specimens displayed skewed crack fronts due to the presence of D_{16} terms ($s \neq 0$). The crack fronts, however, are less curved than those observed in the DCB and ENF tests. This observation is in agreement with the above discussion on the effect of the combination of mode I and mode II loading on the distribution of energy release rate across the width of the MMB specimen.

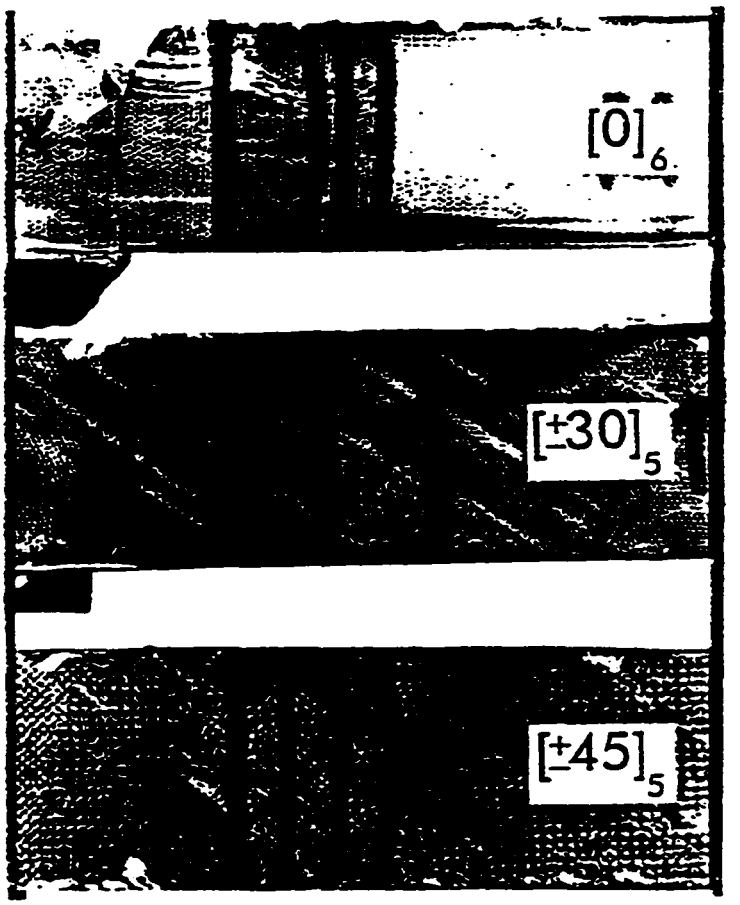

Fig. 4.12 Crack front shapes for glass/polyester MMB specimens. Crack propagated from the initial straight front on the left. The mode ratios, G_I/G_{II}, for the $[0]_6$, $[\pm 30]_5$ and $[\pm 45]_5$ laminates were 4.01, 3.84, and 0.28, respectively.

4.2 Fracture Tests of Glass/Epoxy Cylinder Specimens

4.2.1 Materials and Specimens

The glass/epoxy cylinders were manufactured by IFREMER using the filament winding process. E-glass fibers of density of 2.60 g/cm^3 were obtained from Vetrotex. The epoxy is a LY556 bisphenol A based resin from Ciba Geigy with HY917 anhydride hardener, which is a low-viscosity resin suitable for filament winding. The internal diameter of the cylinders was 160 mm and the nominal wall thicknesses were 6 and 12 mm. A very thin (around 50 g/m^2) matt liner was adhered to the inner surface. Cylinders of 6 and 12 mm wall thickness consist of 12 and 24 layers, respectively. The corresponding lay-ups of the cylinders were $[\pm\theta]_6$ and $[\pm\theta]_{12}$, where θ= 30°, 55° and 85°. A 58 mm long and 13 μm thick aluminum film was inserted at the mid-plane of the cylinders during the filament winding process to define a starter delamination crack, Fig. 3.13. After filament winding, the cylinders were rotated in an oven at 160 °C for three hours to cure the resin. Measured fiber volume fraction for all lay-ups was 61 ± 3% from the burn-off test (ASTM D2584). Curved beam fracture specimens of a nominal length of 200 mm and a nominal width of 18 mm were cut from the cylinder wall for the subsequent DCB, ENF, and MMB tests. In order to accommodate the curved cross-section of the beam fracture specimens, contoured aluminum loading pins and supports were designed, Fig. 4.13, manufactured, and fitted to the ENF and MMB test fixtures originally designed for flat beam specimens, see Figs. 3.17 and 3.19. In addition, contoured aluminum loading tabs were made and adhesively bonded to DCB and MMB specimens. Hinge loading tabs were then fastened

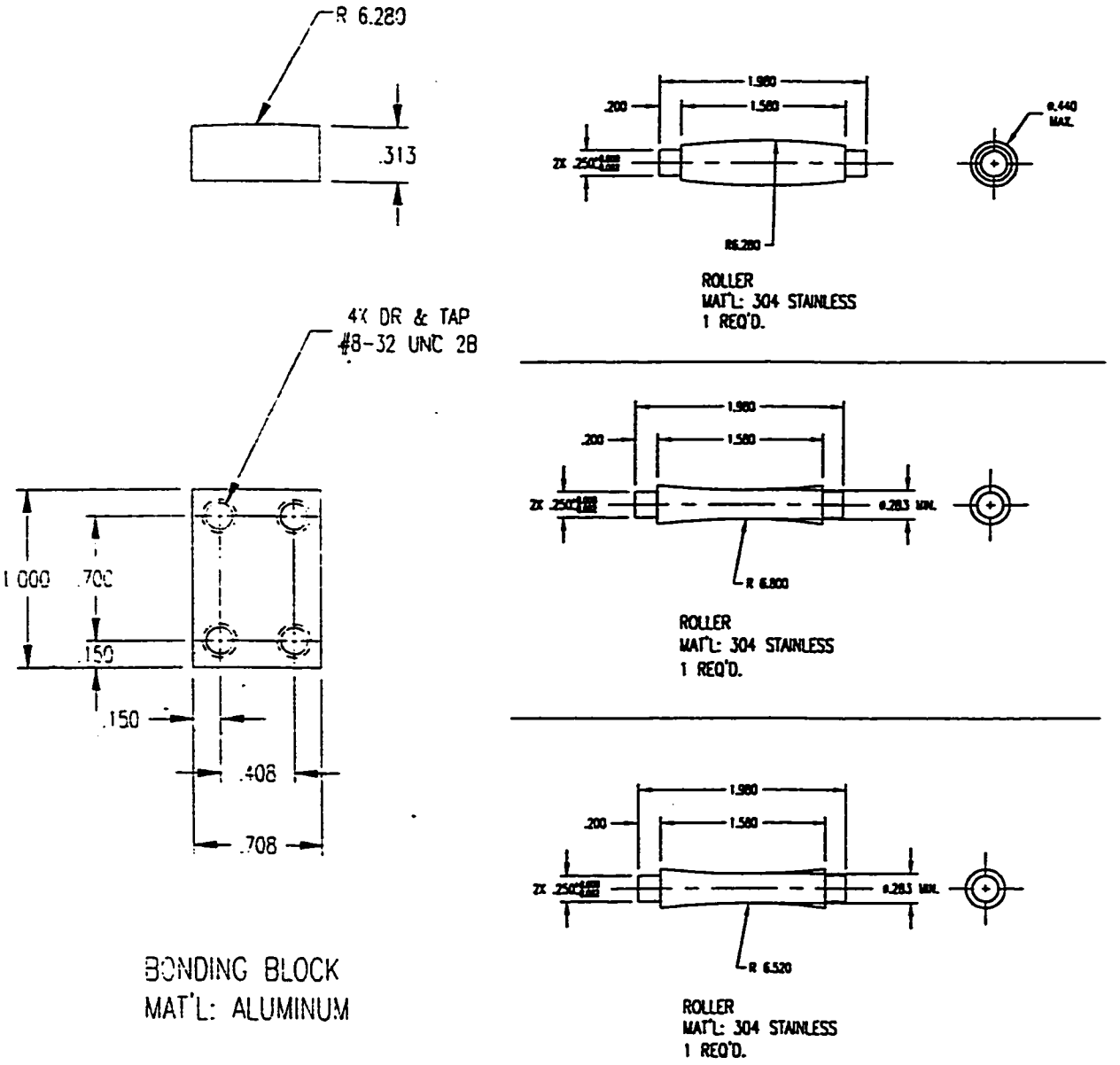

Fig. 4.13 Contoured loading tabs, pins and supports.

to the contoured aluminum tabs, Figs. 3.15 and 3.19. The initial crack lengths for the DCB and MMB specimens, a_0 in Figs. 3.15 and 3.17, were 31 ± 2 and 28 ± 3 mm, respectively. A crack length of 25 ±1 mm was employed for fracture tests of the ENF specimens, Fig. 3.17.

The unidirectional ply properties for glass/epoxy were backed out from mechanical properties determined from tests on various filament wound angle-ply laminates. The ply properties are summarized in Table 3.2. The coefficients of thermal expansion in Table 3.2 were obtained from Ref. [65]. The effective bending modulus, E_x, and the out-of-plane modulus, E_z, of the glass/epoxy angle-ply laminates were calculated following the procedures detailed in Chapter 3. Calculated E_x and E_z values are listed in Table 4.9.

4.2.2 DCB Tests of Glass/Epoxy Cylinder Specimens

4.2.2.1 Fracture Testing

Figure 3.15 shows an angle-ply laminate DCB specimen with curved cross-section machined from the wall of a filament wound composite cylinder. Prior to fracture testing, specimen dimensions (width, thicknesses of the laminate (H) and sub-laminates (h_1 and h_2), and initial crack length (a)) were measured. Then, one edge of the specimen was painted with white 'liquid paper" to facilitate visual observation of the onset of crack propagation and crack length measurements. The initial crack length was marked on the painted specimen edge. All fracture tests were performed from the end of the (straight)

Table 4.9 Bending and out-of-plane extensional moduli, E_x and E_z, for glass/epoxy angle-ply laminates. H is the nominal total laminate thickness.

Lay-up	$[\pm 30]_6$	$[\pm 55]_6$	$[\pm 85]_6$	$[\pm 30]_{12}$	$[\pm 55]_{12}$	$[\pm 85]_{12}$
H, mm	6	6	6	12	12	12
E_x, GPa	21.30	9.54	8.01	21.70	9.56	8.01
E_z, GPa	8.86	9.11	8.03	8.86	9.11	8.03

insert without precracking the specimen. Three replicate specimens were tested for each lay-up. The specimens were loaded in a displacement-controlled Tinius Olsen DS-50 testing frame shown in Fig. 4.1 using a 1.33 kN load cell. A slow cross-head speed (0.76 mm/min) allowed for visual monitoring of crack propagation. Displacement of the cross-head was measured with a LVDT, and a real-time load (P) versus displacement (δ) response was recorded on a x-y plotter. The onset of crack growth from the starter insert was determined by inspection of the specimen edge with the Wild 820 travelling microscope of 20x magnification during the test, and by observation of the progression of the P-δ curve on the chart recorder. The crack growth behavior was continuously monitored during fracture tests using the traveling microscope to detect any crack jumping from the initial mid-plane and to identify and examine the fracture mechanisms. Fracture testing was performed using the incremental test method described earlier for the flat DCB specimens, Sect. 4.1.2, employing crack length increments of about 5 mm.

4.2.2.2 Compliance Predictions

To examine the validity of the compliance predictions using eq. (3.54), a comparison was made with experimental results on the glass/epoxy angle-ply laminates under consideration. The unidirectional ply properties listed in Table 3.2 and test geometry parameters measured prior to fracture tests were used in the compliance calculation. As discussed earlier, the curved, angle-ply DCB beam specimens considered in the experiments possessed additional asymmetry due to different thicknesses of the upper and lower sub-laminates of the delaminated region ($h_1 \neq h_2$). This was expected

since it is generally difficult to achieve uniform ply thickness in filament wound composite cylinders. Overall, the thinner laminates ($[\pm\theta]_6$) were more asymmetric than the thicker ones ($[\pm\theta]_{12}$). The $[\pm 85]_6$ specimens displayed the most asymmetry in geometry. For the $[\pm\theta]_6$ laminates, the degree of asymmetry (h_1/h_2 ratio) ranged from 0.9 to 1.6 while it varied from 1.1 to 1.4 for the $[\pm\theta]_{12}$ laminates. Due to the specimen-to-specimen variations of total and sub-laminate thicknesses, a compliance vs. crack length curve was measured and calculated for each specimen. Figure 4.14 shows representative compliance vs. crack length data for angle-ply laminate DCB specimens. No compliance vs. crack length curve is shown for the $[\pm 85]_6$ and $[\pm 85]_{12}$ laminates because these specimens failed in flexure prior to delamination propagation. Also shown in Fig. 4.14 are predicted curves of compliance vs. crack length. The predictions are overall in good agreement with experimental data except at longer crack lengths where the elastic foundation (EF) model predicts less compliance than measured experimentally. Such a discrepancy is attributed to multiple delamination of the angle-ply laminates at longer crack lengths (to be discussed later). Such cracking tends to increase the beam compliance. Overall, the good agreement with experimental results at shorter crack lengths supports the applicability of the present EF beam model for analysis of curved, angle-ply laminate DCB specimens.

4.2.2.3 Fracture Test Results

Representative load-displacement (P-δ) curves for the $[\pm 30]_n$ and $[\pm 55]_n$ (n= 6,12) DCB specimens are shown in Fig. 4.15. P-δ curves are not shown for the $[\pm 85]_6$ and

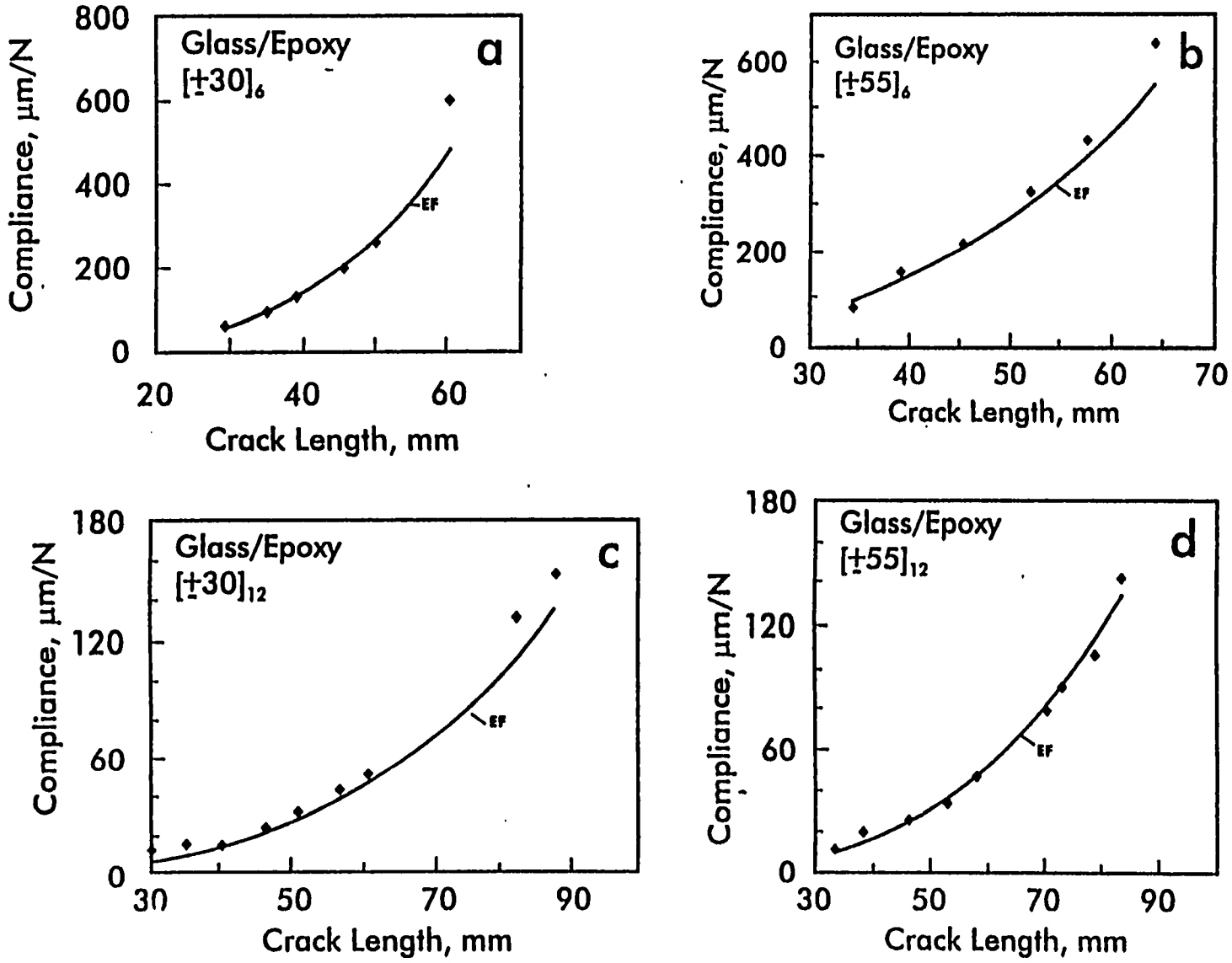

Fig. 4.14 Calculated (EF) and experimentally measured compliance vs. crack length for glass/epoxy DCB specimens, a) $[\pm 30]_6$, b) $[\pm 55]_6$, c) $[\pm 30]_{12}$, and d) $[\pm 55]_{12}$.

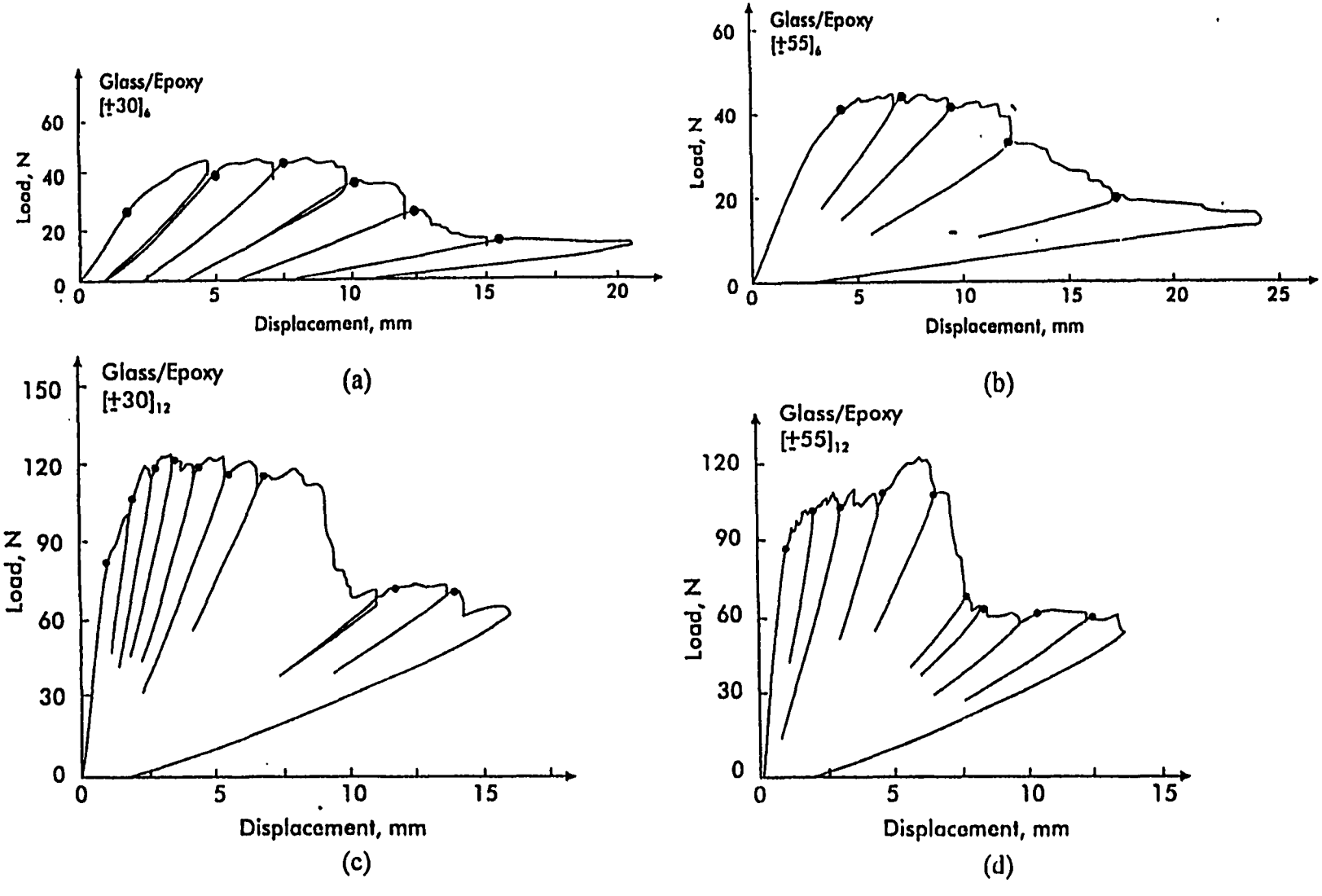

Fig. 4.15 Representative load-displacement response curves for glass/epoxy DCB specimens, a) $[\pm 30]_6$, b) $[\pm 55]_6$, c) $[\pm 30]_{12}$, and d) $[\pm 55]_{12}$.

$[\pm 85]_{12}$ lay-ups because, as mentioned earlier, these specimens failed in flexure prior to delamination propagation. The first loading-unloading cycle represents in each case crack growth directly from the insert film. The circles on the graphs mark visually observed onset of crack propagation.

For the $[\pm 30]_6$ laminate, Fig. 4.15a, the P-δ response is linear before the onset of crack propagation. Crack propagation occurs initially in a stable manner at progressively increasing load during the first increment. The small vertical drop at the end of each crack growth increment is due to stress relaxation during crack length measurement prior to unloading of the specimen for compliance evaluation. Figure 4.15a indicates oscillations in the fracture load and occasional stick-slip crack growth that are attributed to the increased fracture resistance associated with fiber bridging, and the reduced resistance associated with pull-out and breakage of the bridged fibers. Such behavior was observed for all specimens. Fiber bridging became significant after about 5 mm of stable crack growth from the insert and increased with increased crack length until bridged fibers broke at larger crack lengths. Similar observations have been made by other researchers [31-34,48,54,57]. After some further crack growth, the delamination was arrested due to an interlaced fiber bundle. With further opening displacement, another crack formed and grew in a plane above or below the original delamination plane. Figure 4.16 is an edge photograph of a DCB specimen showing multiple cracking and branching. The crack jumping resulted in sudden and large vertical drops in load, especially pronounced for the $[\pm\theta]_{12}$ laminates, see Figs. 4.15c and 4.15d, and continued

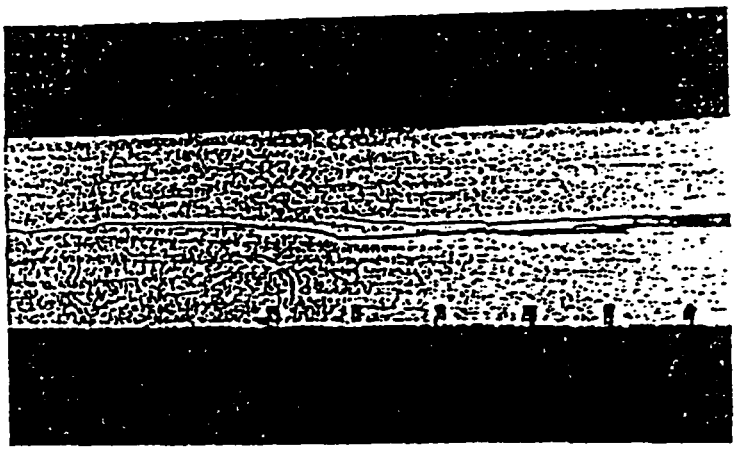

Fig. 4.16 Photograph of multiple cracking and branching observed during DCB test of a $[\pm 30]_{12}$ glass/epoxy specimen.

delamination growth at another interface. Further growth occurred until the delamination was rearrested by another interlaced fiber bundle. We believe that the main reason for the crack arrest and substantial resistance to further propagation is the interlaced fiber bundles originating from the filament winding process, see Fig. 4.17. The film insert, Fig. 3.13, would prevent fiber interlacing during the winding process, but, after some increment of crack growth along the axis of the cylinder, the crack tip would intersect a region of interlaced fiber bundles. After unloading the specimens it was observed that the thinner laminates displayed substantial permanent deformation, see Figs. 4.15a and 4.15b. Such behavior is attributed to matrix yielding and possible microcracking. The P-δ curves for the thicker $[\pm 30]_{12}$ and $[\pm 55]_{12}$ laminates, Figs. 4.15c and 4.15d, are more linear and display less permanent deformation than the thinner laminates.

Due to the nonlinear load-displacement response and permanent deformations observed for the thinner DCB specimens of $[\pm 30]_6$ and $[\pm 55]_6$ lay-ups, linear elastic fracture mechanics (LEFM) is not strictly applicable. Fracture toughness, G_c, was nevertheless reduced using the LEFM approach, which would produce conservative toughness data. The elastic foundation model (EF) analysis presented above will be employed to reduce the delamination fracture toughness, G_c, from the experimental data. Following the procedures detailed in Chapter 3, the moduli, E_x and E_z, Table 4.9, and area moments of inertia for the arms of the DCB specimen (I_1 and I_2) were calculated from basic ply properties, Table 3.2, and measured beam cross-sectional dimensions. Then, G/P^2 was calculated from eq. (3.55) for each specimen as a function of crack

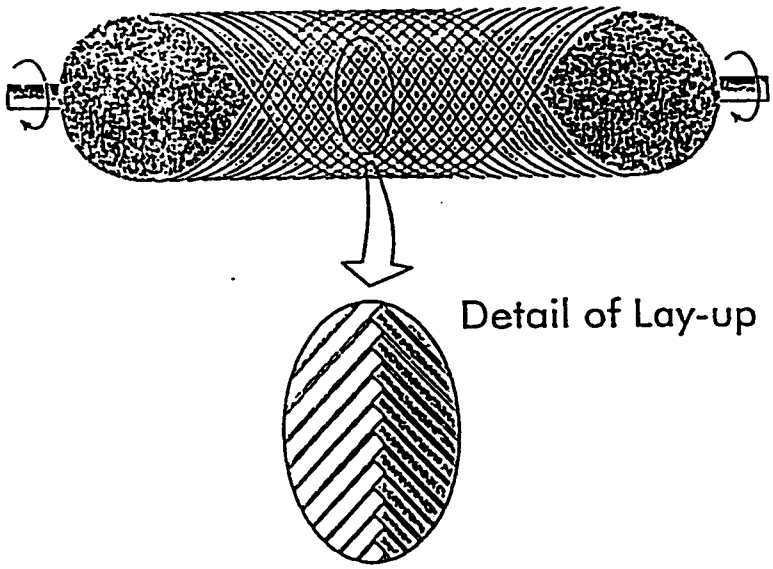

Fig. 4.17 Interlacing of fiber bundles during the filament winding process.

length. To determine G_c at any given crack length, the critical load P_c corresponding to the onset of crack growth was measured in a DCB fracture test and substituted in the G/P^2 relation at that crack length. In addition, the experimental compliance method [12] described in Sect. 4.1.3.1 was used to directly evaluate G_c given by eq. (4.2). Resistance curves (R-curves) were constructed. Figure 4.18 shows representative R-curves for each lay-up. The elastic foundation model (EF) produces similar R-curves as the compliance calibration (CC) method as would be expected from the accurate compliance predictions, Fig. 4.14. For the $[\pm 30]_6$ lay-ups, Fig. 4.18a, G_c increases initially steeply with crack length for crack lengths of up to about 40 mm due to toughening caused by bridging of angle-ply fiber bundles, then drops and levels off after crack jumping to a new interface. For the $[\pm 55]_6$ lay-up, G_c continuously increased with crack length, Fig. 4.18b, until it reached an "apparent" plateau at a crack length of 50 mm where fracture testing was discontinued. Since the $[\pm 55]_6$ specimens behaved very similar to the $[\pm 30]_6$, $[\pm 30\ ]_{12}$, and $[\pm 55]_{12}$ specimens during the fracture tests, their R-curve would be expected to be similar to those had they been tested further for longer crack lengths. We should point out that the R-curves shown in Fig. 4.18 are not unique, but depend on laminate thickness. Clearly, due to fiber bridging, our DCB tests correspond to the "large scale bridging regime", where R-curve depends on specimen geometry and size [61,66].

Table 4.10 lists the initiation values of fracture toughness obtained from the DCB tests. No toughness values are presented for the $[\pm 85]_6$ and $[\pm 85]_{12}$ lay-ups since they failed in flexure prior to interlaminar crack growth. The initiation values of fracture

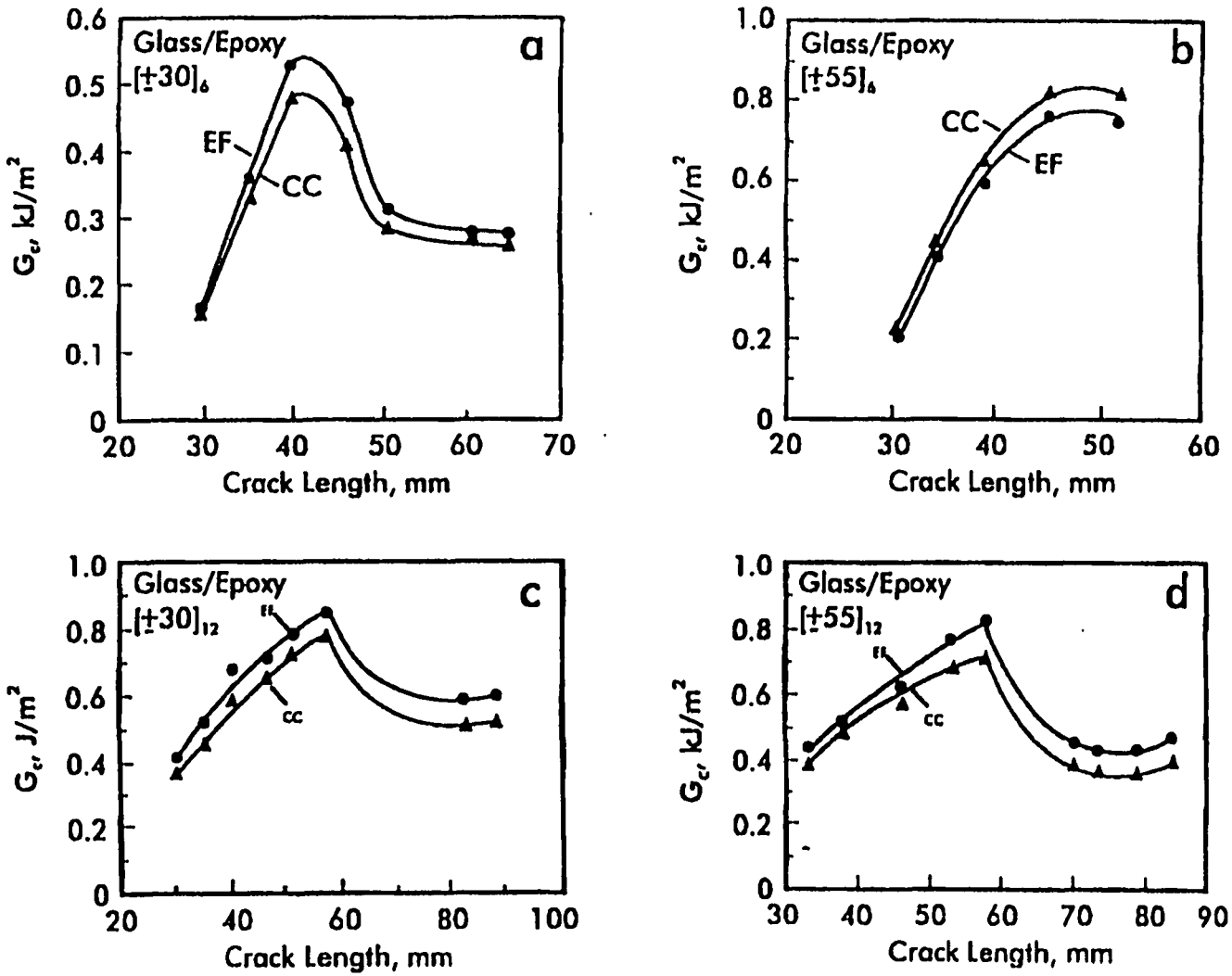

Fig. 4.18 Fracture resistance curves for glass/epoxy DCB specimens, a) $[\pm 30]_6$, b) $[\pm 55]_6$, c) $[\pm 30]_{12}$, and d) $[\pm 55]_{12}$.

Table 4.10 Initiation fracture toughness values of glass/epoxy laminates reduced by elastic foundation model (EF) and experimental compliance calibration method (CC).

Lay-up	G_c^{EF} (init.) (J/m^2)	G_c^{CC} (init) (J/m^2)
$[\pm 30]_6$	175 ± 42	172 ± 45
$[\pm 55]_6$	210 ± 18	219 ± 49
$[\pm 30]_{12}$	369 ± 17	418 ± 24
$[\pm 55]_{12}$	403 ± 60	450 ± 15

toughness in Table 4.10 represent crack growth directly from the insert without any influence of fiber bridging and crack jumping as observed during further crack propagation. Since the evaluation of fracture toughness becomes questionable after crack jumping, the apparent plateau values observed in Fig. 4.18 can not be considered as steady state propagation toughness values. Table 4.10 shows that the initiation fracture toughness values obtained from the EF and CC methods are relatively close. It should also be reemphasized that the linear elastic evaluation of G_c values for the thinner specimens is associated with substantial difficulties making the data highly conservative and less reliable than those for the thicker laminates. The subsequent discussion is therefore based on the results for the thicker laminates. Inspection of the data for the $[\pm\theta]_{12}$ laminates in Table 4.10 indicates that the initiation toughness increases with increased angle θ at the $\pm\theta$ interface, although the influence of angle is quite moderate. For comparison, the initiation mode I fracture toughness for flat glass/polyester angle-ply laminates, Sect. 4.1.3, was also found to be relatively independent of θ. Trends of increasing mode I fracture toughness with interface angle θ have also been observed for similar glass/epoxy angle-ply laminates with curved cross-section [48] and for flat graphite/epoxy angle-ply laminates [31,34,54]. Furthermore, the range of initiation fracture toughness data in Table 4.10 for the curved, glass/epoxy angle-ply laminates are in close agreement with G_{Ic} for curved glass/epoxy laminates of $\pm30°$ and $\pm45°$ interfaces (216-256 J/m^2) and for flat, unidirectional glass/epoxy (247 – 316 J/m^2) [48].

To examine the possibility of nonuniform crack extension, the parameters, d_c and s, defined in Chapter 1, eqs. (2.45) and (2.46), were calculated, see Table 4.11. For all lay-ups, the parameter d_c is nonzero indicating tendency for nonuniform crack extension. Since there is no bending/twist coupling in the sub-laminates of the $[\pm\theta]_n$ (n = 6,12) lay-ups considered, the skewness parameter s vanishes indicating no tendency for formation of skewed crack fronts. In order to monitor the interlaminar crack front during fracture testing, selected DCB specimens were unloaded, removed from the grips, and examined under a strong light source to observe and mark the crack front. The specimen was then reloaded and the procedure was repeated after each crack increment. This method worked since glass/epoxy is somewhat transparent. Figure 4.19 shows photographs of representative crack front shapes for the various lay-ups examined. As predicted from Table 4.11, all fracture specimens exhibited nonuniform crack fronts after growth from the straight insert. The crack extended further at the center than at the edges. Similar growth has been predicted and observed in flat, unidirectional and angle-ply DCB laminates discussed in Sect. 4.1.3.

4.2.3 ENF Tests of Glass/Epoxy Cylinder Specimens

4.2.3.1 Fracture Testing

Figure 4.20 shows an angle-ply laminate ENF specimen machined from the wall of a filament wound composite cylinder and the three-point loading fixture with contoured loading pins and supports. Prior to fracture testing, specimen dimensions

Table 4.11 Parameters d_c and s characterizing nonuniform distribution of energy release rate for glass/epoxy laminates, n = 6 and 12.

Lay-up	Sub$[\pm 30]_n$	Sub$[\pm 55]_n$	Sub$[\pm 85]_n$
d_c	0.193	0.242	0.022
s	0	0	0

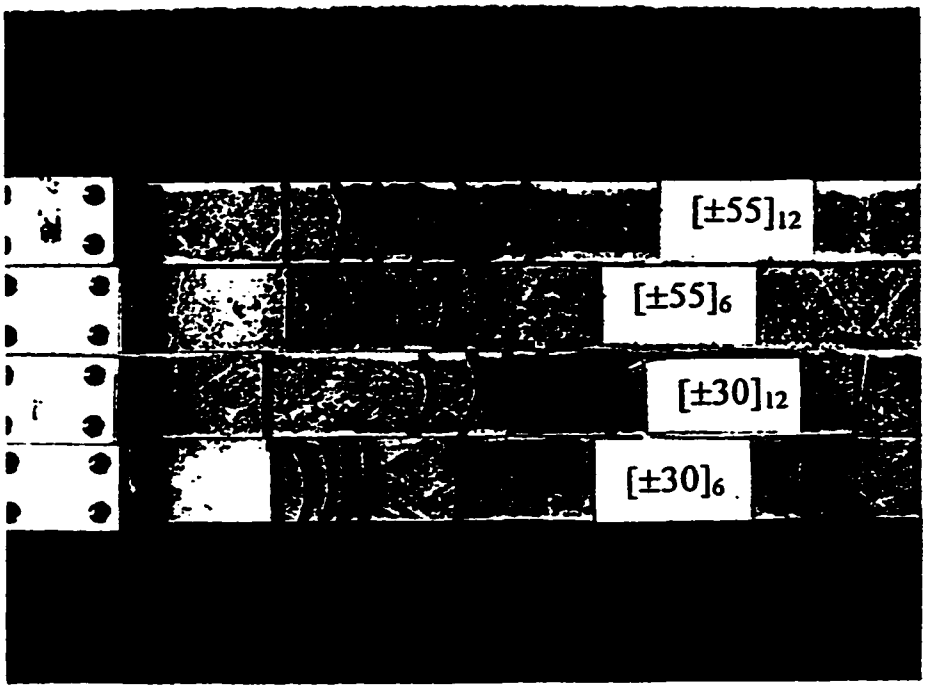

Fig. 4.19 Photographs of initial (straight) crack fronts defined by insert film and crack fronts after propagation for $[\pm 30]_6$, $[\pm 55]_6$, $[\pm 30]_{12}$, and $[\pm 55]_{12}$ glass/epoxy DCB specimens. The crack propagated from left to right.

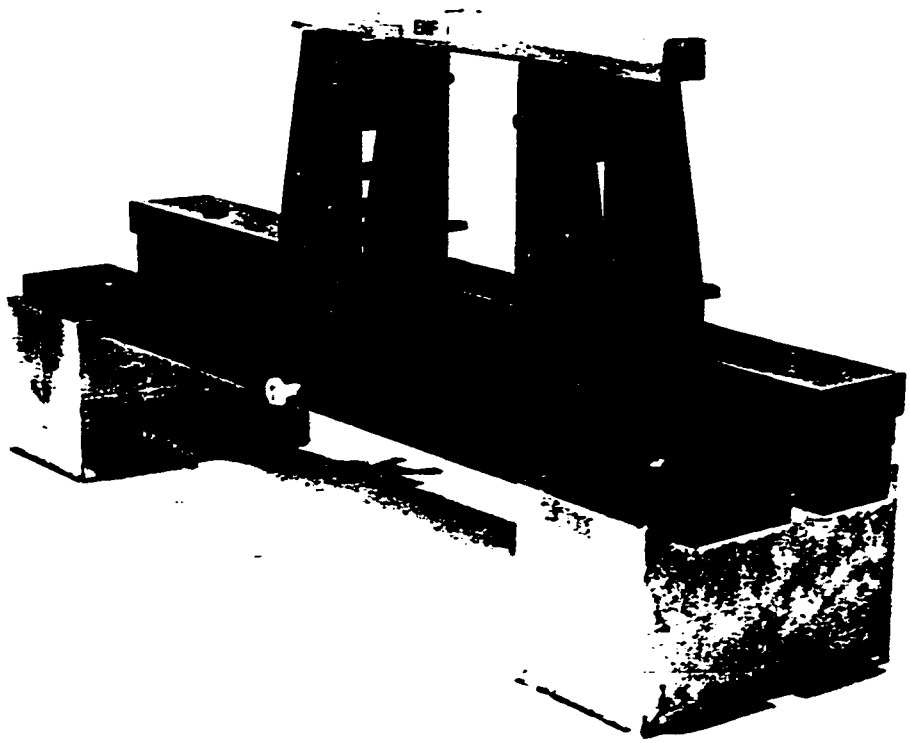

Fig. 4.20 A glass/epoxy ENF specimen machined from the wall of a filament wound cylinder and ENF loading fixture.

(width, thicknesses of the laminate (H) and sub-laminates (h_1 and h_2), and initial crack length) were measured. Similar to the previously measured DCB specimen, it was observed that the curved, angle-ply ENF beam specimens considered in the experiments possessed additional asymmetry due to different thicknesses of the upper and lower sub-laminates of the delaminated region ($h_1 \neq h_2$). The $[\pm 85]_6$ specimens displayed the most asymmetry in geometry. Overall, the thinner laminates, namely, ($[\pm\theta]_6$) were more asymmetric than the thicker lay-ups ($[\pm\theta]_{12}$). For the $[\pm\theta]_6$ laminates, the degree of asymmetry (h_1/h_2 ratio) ranged from 1.3 to 1.7 while it varied from 1.1 to 1.4 for the $[\pm\theta]_{12}$ laminates. Since a thicker sub-laminate in the bottom would result in crack face contact over the majority of the crack length which would complicate the analysis of deformation, all ENF specimens were tested with the thicker sub-laminate on top.

One edge of the specimen was painted with white 'liquid paper" to facilitate visual observation of the onset of crack propagation. The initial crack position was marked on the painted specimen edge. The span length, 2L, was 100 mm. Compliance measurements at small loads were performed at crack lengths of 0, 10, 20, and 30 mm on all specimens before fracture testing. All fracture tests were performed at a crack length of 25 mm from the end of the (straight) insert without precracking the specimen. Four replicate specimens were tested for each lay-up. All testing was performed in a displacement-controlled Tinius Olsen DS-50 test frame, Fig. 4.1. A 1.36 kN load cell was used in fracture tests of $[\pm\theta]_6$ lay-ups whereas a 136 kN load cell was employed for the $[\pm\theta]_{12}$ lay-ups. A cross-head speed of 0.76 mm/min allowed visual monitoring of crack

propagation. Displacement of the cross-head was measured with a LVDT, and the real-time load (P) versus displacement (δ) response was recorded on a x-y plotter. The onset of crack growth from the starter insert was determined by inspection of the specimen edge with the Wild 820 traveling microscope of 20x magnification during the test, and by observation of the P-δ curve. The onset of crack growth as observed from the edge was marked on the P-δ curve to indicate the corresponding critical load and displacement values. As noticed in DCB testing of the laminates, Sect. 4.2.2, the crack did not propagate at the specimen mid-plane after onset of crack propagation. Such behavior will influence the apparent fracture toughness and invalidate fracture mechanics analysis based on the assumption of collinear crack propagation. Therefore, the crack growth behavior was continuously examined during fracture tests using the traveling microscope.

Prior to fracture testing, specimens dimensions (width, thickness of laminate (H), and sublaminates thicknesses (h_1 and h_2), and crack length) were measured. Following the equations derived in Chapter 3, the effective bending compliances, d_{11}, for the cracked and uncracked regions of each specimen, Fig. 3.17, were calculated from basic ply properties in Table 3.2. Then, energy release rate per square of applied load, G/P^2, was determined from eq. (3.64) for each individual specimen prior to fracture testing. To determine G_c, the critical load P_c corresponding to the onset of crack growth was measured in an ENF fracture test and substituted in the G/P^2 relation.

4.2.3.2 Compliance Predictions

To examine the validity of the compliance predictions from the present shear deformation beam theory model using eq. (3.60), a comparison was made with experimental results. The unidirectional ply properties listed in Table 3.2 and test geometry parameters measured prior to fracture tests were used in the compliance calculation. Due to the variations of total and sub-laminate thicknesses, width, and crack length from specimen-to-specimen for each lay-up, a compliance vs. crack length curve was developed for each specimen tested. Figure 4.21 shows calculated and measured compliance vs. crack length for a $[\pm 55]_{12}$ specimen. Table 4.12 summarizes average calculated and measured compliance values and their scatter. The predictions are overall in good agreement with experimental data. The discrepancies between predicted and measured compliances may be due to a nonuniform distribution of fiber volume fraction through the thickness that would have a strong influence on the beam compliance. Overall, the agreement with experimental results supports the applicability of the present SBT formulation for analysis of curved, angle-ply laminate ENF specimens.

4.2.3.3 Fracture Test Results

Representative load-displacement (P-δ) curves for the curved, angle-ply laminate ENF specimens are shown in Fig. 4.22. The filled circle on each graph marks the point where onset of crack propagation was visually observed. As shown in Fig. 4.22, the visual onset of crack propagation coincides with unstable growth. P-δ curves are not shown for the $[\pm 85]_6$ and $[\pm 85]_{12}$ lay-ups because these specimens failed in flexure prior

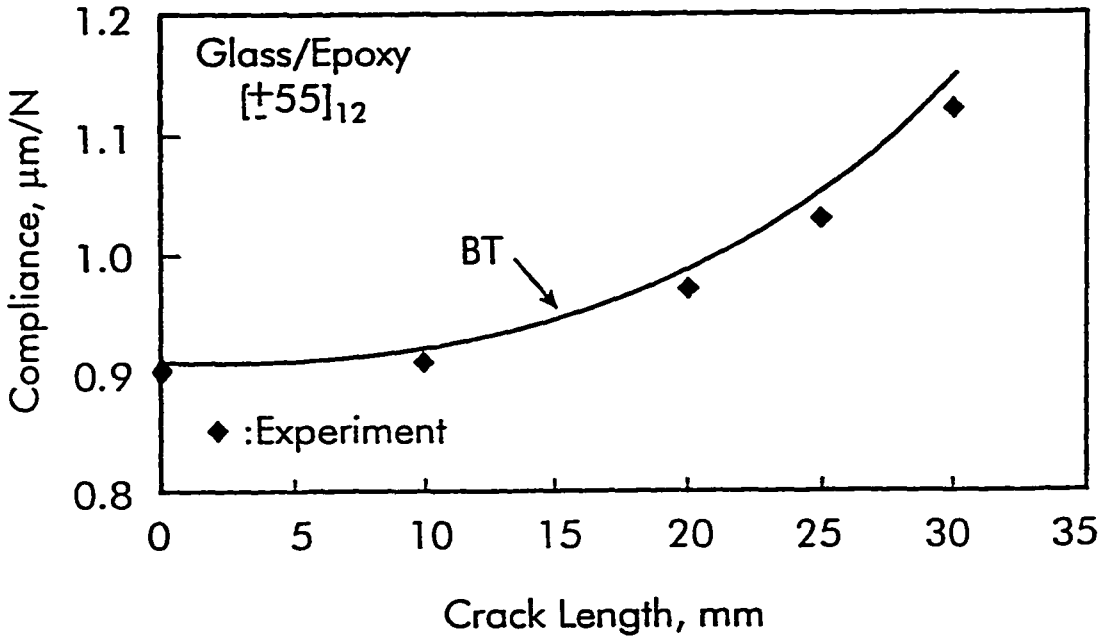

Fig. 4.21 Predicted (BT) and experimental compliance vs. crack length for a $[\pm 55]_{12}$ glass/epoxy ENF specimen.

Table 4.12 Predicted (BT) and measured (exp) compliances for glass/epoxy ENF specimens (a=25mm, L=50mm).

Lay-up	C^{BT} (10^{-6} m/N)	C^{exp} (10^{-6} m/N)
$[\pm 30]_6$	6.41 ± 0.60	7.37 ± 0.23
$[\pm 55]_6$	7.13 ± 0.26	6.78 ± 0.58
$[\pm 85]_6$	8.41 ± 0.42	8.05 ± 0.31
$[\pm 30]_{12}$	0.58 ± 0.05	0.71 ± 0.03
$[\pm 55]_{12}$	1.04 ± 0.13	1.01 ± 0.03
$[\pm 85]_{12}$	1.36 ± 0.07	1.27 ± 0.03

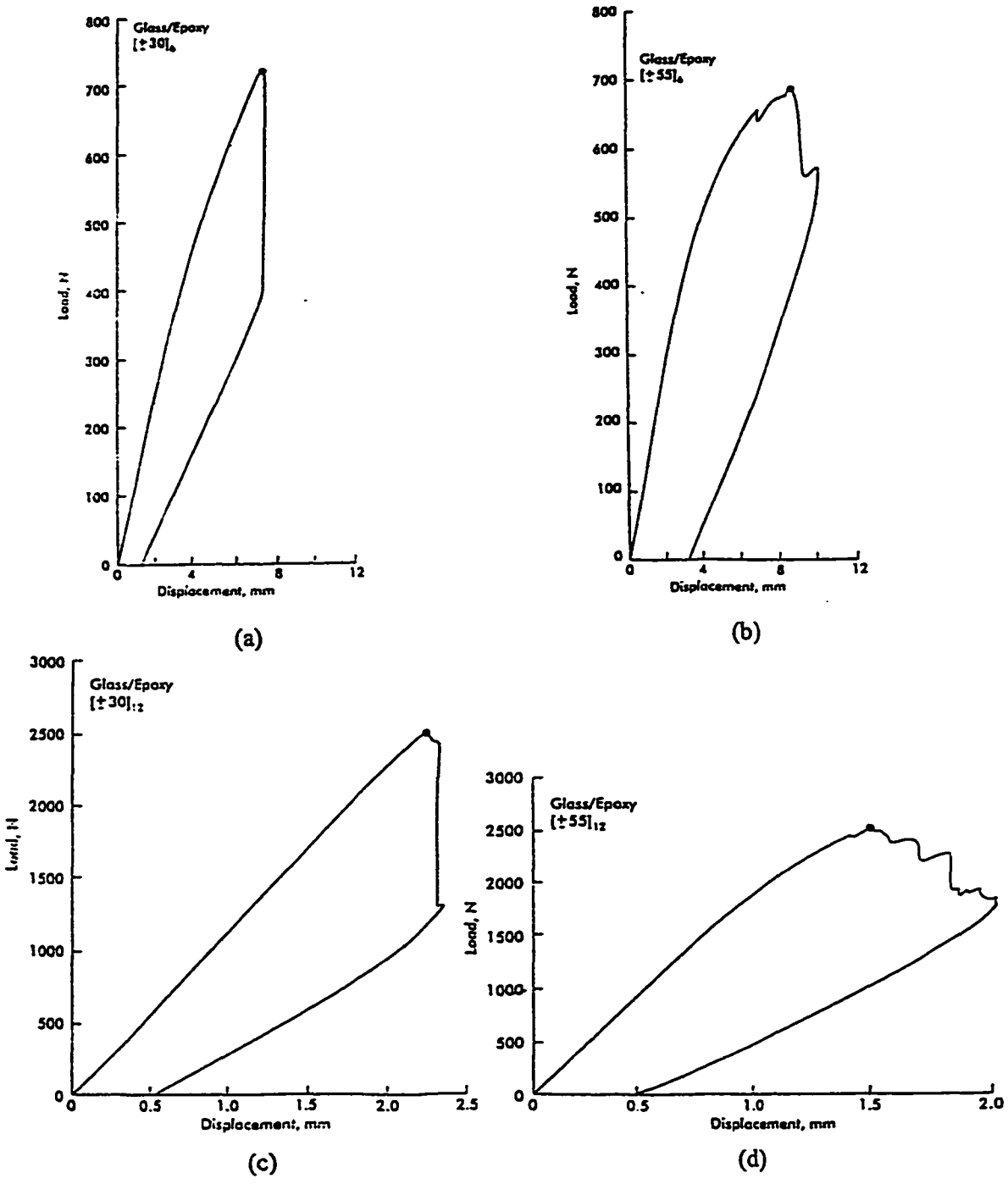

Fig. 4.22 Representative load-displacement response curves for glass/epoxy ENF specimens, a) $[\pm 30]_6$, b) $[\pm 55]_6$, c) $[\pm 30]_{12}$, and d) $[\pm 55]_{12}$.

to delamination propagation. Upon loading the $[\pm 85]_6$ laminates, the initial delamination kinked upward at an angle of 45° to 60° with respect to the specimen's longitudinal axis before any delamination growth was observed. At increased load, another crack initiated from the bottom (tension side) of the lower sublaminate, that grew through the laminate thickness, and eventually broke the thinner lower sublaminate in a very fast, unstable manner. Significant permanent bending deformation due to matrix yielding of the $[\pm 85]_6$ specimens was visible after the failed specimens were removed from the fixture.

For the $[\pm 30]_6$, $[\pm 55]_6$, and $[\pm 55]_{12}$ laminates, Figs. 4.22a, 4.22b, and 4.22c, the P-δ curves are nonlinear prior to fracture. The P-δ record for the $[\pm 55]_6$ specimen reveals several "pop-ins" prior to fast fracture. This is attributed to secondary matrix cracks that initiated in the thin matt liner on the tension side of the specimen, grew perpendicular to the specimen's longitudinal axis, and were arrested prior to interlaminar crack growth. More secondary cracks were observed with increased load. In the case of $[\pm 30]_6$ lay-ups, the secondary cracks grew first perpendicular to the specimen's longitudinal axis, then kinked and propagated parallel to the specimen's longitudinal axis under increased load before they were arrested prior to interlaminar fracture. Permanent deformation remaining after unloading specimens indicates also that significant matrix yielding occurred except for the $[\pm 30]_{12}$ lay-ups, Fig. 4.22b.

For the $[\pm 30]_6$ and $[\pm 30]_{12}$ lay-ups, Figs. 4.22a and 4.22c, unstable delamination growth occurred until the crack was arrested at mid-span below the load application point

(a = L), where the compressive forces are large enough to suppress further crack growth. For the $[\pm 55]_6$ and $[\pm 55]_{12}$ lay-ups, Figs. 4.22b and 4.22d, unstable, collinear interlaminar crack growth from the inset film was arrested when another crack formed and grew at another interface in the upper (compression dominated) sub-laminate of the specimen. Similar observations were made by other researchers [53,54]. Polaha et al. [53] observed in ENF tests of flat, multidirectional lay-ups that the delamination would generally shift interfaces through a transverse crack, and the shift was always upwards towards the compression dominated surface. Chou et al. [54] conducted ENF tests on flat, graphite/epoxy composites with a 60°/-60° crack interface. They similarly found that the delamination crack shifted to the compressive side through matrix cracks.

Due to the nonlinear response, linear elastic fracture mechanics (LEFM) is not strictly applicable to these laminates. Although there are other more appropriate methods to calculate the fracture toughness for cases where plasticity is present [58-60], such methods are considered outside the scope of this paper. Thus, fracture toughness values of all specimens were determined based on the LEFM approach which would produce conservative toughness data. In addition to the beam theory formulation, eq. (3.64), the experimental compliance method [12] was used to directly evaluate the fracture toughness. Experimental compliance versus crack length data was fitted to a cubic polynomial of the form as guided by eq. (3.60),

$$C = c_0 + c_1 a^3 \tag{4.3}$$

where a is the crack length and c_0 and c_1 are determined from the fitting procedure. The fracture toughness G_c is obtained by differentiation of eq. (4.3) with respect to crack length according to eq. (2.44) and substitution of the measured critical load P_c at the onset of crack advance.

Figure 4.23 shows representative compliance calibration plots of the angle-ply lay-ups considered in the experiments. Table 4.13 lists the fracture toughness values obtained from the ENF tests. No toughness values are presented for the $[\pm 85]_6$ and $[\pm 85]_{12}$ lay-ups since they failed in flexure prior to interlaminar crack growth. Table 4.13 indicates that the fracture toughness values obtained from the shear deformation beam theory and compliance calibration method are consistent which supports the viability of the present formulation for analysis of cylinder ENF specimens. The differences are similar to those observed between the predicted and experimental compliance values in Table 4.12. Hence, lay-ups with higher experimental compliance than predicted by the present beam theory also have higher fracture toughness obtained by experimental compliance calibration method than that reduced from the beam theory.

Inspection of the data in Table 4.13 reveals that the fracture toughness of the ±30° interface is independent of laminate thickness as would be expected since the fiber volume fractions are similar. For the ±55° interface, the data indicate a steep increase of toughness with increased laminate thickness. We believe that part of the reason for this

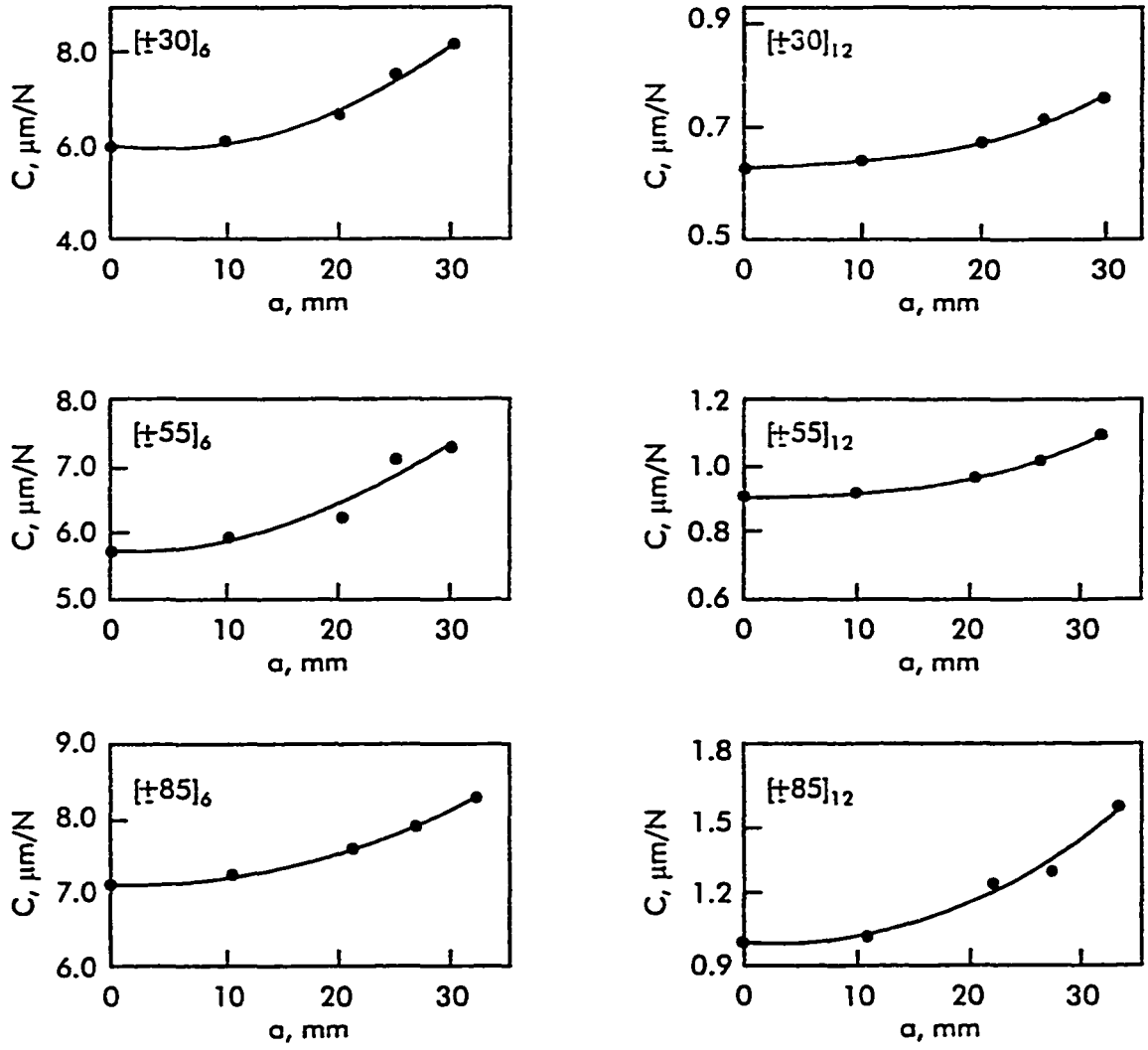

Fig. 4.23 Representative compliance calibration plots of the glass/epoxy ENF specimens.

Table 4.13 Fracture toughness values of glass/epoxy ENF specimens reduced by beam theory (BT) and experimental compliance calibration method (CC).

Lay-up	G_c^{BT} (kJ/m^2)	G_c^{CC} (kJ/m^2)
$[\pm 30]_6$	1.78 ± 0.40	2.23 ± 0.45
$[\pm 55]_6$	1.36 ± 0.05	1.21 ± 0.08
$[\pm 30]_{12}$	1.83 ± 0.11	2.20 ± 0.31
$[\pm 55]_{12}$	2.62 ± 0.33	2.99 ± 0.37

anomaly is the strong nonlinear behavior observed prior to crack growth. Especially, the $[\pm 55]_6$ laminates displayed substantial nonlinear P-δ response prior to crack propagation, and the fracture toughness values reduced for these laminates (1.36 and 1.21 kJ/m^2) are probably highly conservative.

The apparent mode II fracture toughness data for the curved glass/epoxy angle-ply laminates may be compared to such data obtained for flat glass/polyester laminates, Table 4.6. If we neglect the unrealistically low toughness of the $[\pm 55]_6$ laminate in Table 4.13, both systems show increasing toughness with increased angle θ of the $\pm\theta$ interface. The curved glass/epoxy laminates display somewhat larger fracture toughnesses at similar angles than the flat glass/polyester laminates. Trends of increasing mode II fracture toughness with increased angle θ at $\pm\theta$ interfaces have been observed for flat graphite/epoxy laminates by Chai [32] and Chou et al. [54]. The apparent mode II fracture toughness data for the curved glass/epoxy angle-ply laminates, Table 4.13, agree well also with that for flat, unidirectional glass/epoxy composite laminates that range between 1.79 kJ/m^2 and 2.66 kJ/m^2 [67].

After fracture tests, the specimens were examined under a light source and the crack front was marked. Figure 4.24 shows representative crack front shapes for the various lay-ups examined. As predicted from Table 4.11, all fracture specimens exhibited nonuniform crack fronts after growth from the straight insert. The larger energy release rate at the edges of an ENF specimen predicted by Davidson et al. [17] is reflected by

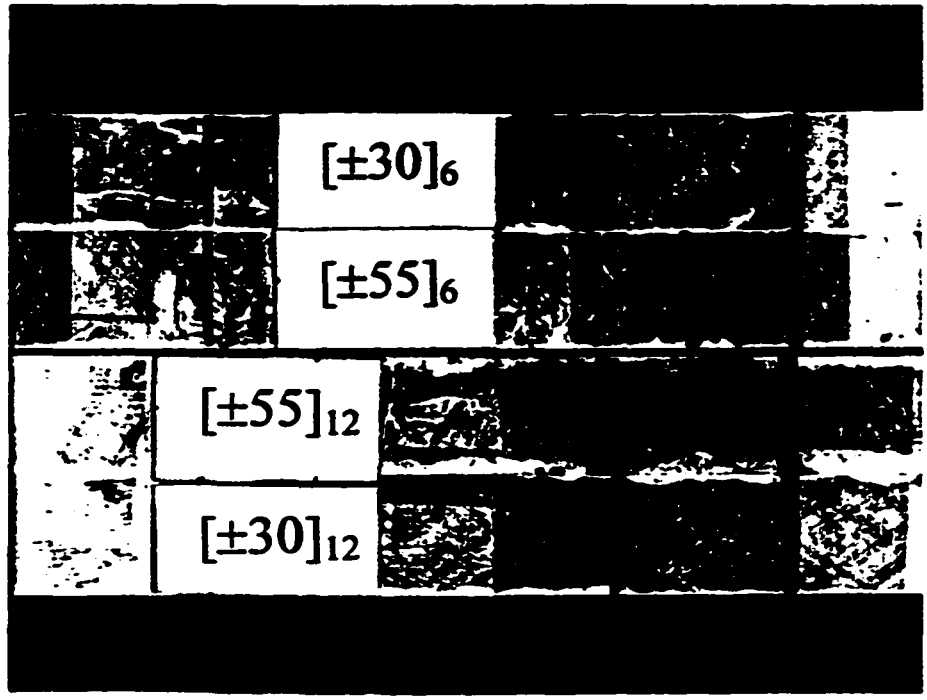

Fig. 4.24 Photographs of initial (straight) crack fronts defined by insert film and crack fronts after propagation for glass/epoxy ENF specimens. The crack propagated from right to left.

further crack extension at the edges than at the center.

4.2.4 MMB Tests of Glass/Epoxy Cylinder Specimens

4.2.4.1 Fracture Testing

Figure 3.19 shows the geometry of an MMB specimen with curved cross-section machined from the wall of a filament wound composite cylinder. Prior to fracture testing, specimen dimensions (width, thicknesses of the laminate (H) and sub-laminates (h_1 and h_2), and initial crack length) were measured. Similar to the previously tested DCB and ENF specimens, Sects. 4.2.2 and 4.2.3, the curved, angle-ply MMB beam specimens considered in the experiments possessed additional asymmetry due to different thicknesses of the upper and lower sub-laminates of the delaminated region ($h_1 \neq h_2$).

One edge of the specimen was painted with white 'liquid paper" to facilitate visual observation of the onset of crack propagation and crack length measurements. The initial crack length was marked on the painted specimen edge. All fracture tests were performed from the end of the (straight) insert without precracking the specimen. Load positions, c, of 28 and 97 mm, see Fig. 3.7, were employed. Two replicate specimens per each mode ratio were tested for each lay-up. The specimens were loaded in a MMB test fixture, Fig. 3.7, positioned in a displacement-controlled Tinius Olsen DS-50 test frame using a 1.33 kN load cell. A slow cross-head speed (0.50 mm/min) allowed for visual monitoring of crack propagation. Displacement of the cross-head was measured with a linear voltage differential transducer (LVDT), and a real-time load (P) versus displacement (δ) response was recorded on a x-y plotter. The onset of crack growth from

the starter insert was determined by inspection of the specimen edge with a Wild 820 traveling microscope of 20x magnification during the test, and by observation of the P-δ curve. The crack growth behavior was observed during the fracture tests using the travelling microscope to detect any crack jumping from the initial mid-plane, and to identify and examine the fracture mechanisms.

4.2.4.2 Compliance Predictions

The unidirectional ply properties listed in Table 3.2 and test geometry parameters measured prior to fracture tests were used in the compliance calculation. The experimental compliance ($C = \delta/P$) of the MMB specimens was measured from the slope of the initial linear region of each P/δ curve. Due to the specimen-to-specimen variations of total and sub-laminate thicknesses and width, compliance was determined for each specimen. Table 4.14 presents experimental and predicted compliances for angle-ply laminate MMB specimens along with the nominal fracture mode ratios. Compliance increases with increasing ply angle θ and G_I/G_{II} ratio, and decreasing laminate thickness. Overall, the predictions are in agreement with experimental data which supports the applicability of the present beam model.

Table 4.14 Measured (EXP) and calculated (BT) compliance data for glass/epoxy MMB specimens.

Lay-up	$[\pm 30]_6$		$[\pm 55]_6$		$[\pm 85]_6$		$[\pm 30]_{12}$		$[\pm 55]_{12}$		$[\pm 85]_{12}$	
c, mm	28	97	28	97	28	97	28	97	28	97	28	97
G_I/G_{II}	0.32	4.47	0.30	4.27	0.30	4.22	0.36	5.11	0.33	4.72	0.33	4.50
C^{BT} μm/N	13.7 ± 2.6	92.5 ± 4.2	20.0 ± 0.4	124 ± 5	25.7 ± 4.2	227 ± 18	1.5 ± 0.1	7.2 ± 0.6	2.4 ± 0.1	16.4 ± 0.6	3.6 ± 0.2	26.8 ± 1.7
C^{EXP} μm/N	15.6 ± 0.4	109 ± 5	23.2 ± 0.1	139 ± 32	22.4 ± 0.2	N/A	1.8 ± 0.4	7.5 ± 0.1	2.9 ± 0.6	19.3 ± 1.5	4.1 ± 0.5	27.0 ± 2.2

4.2.4.3 Fracture Test Results

Representative load-displacement (P-δ) curves for the $[\pm 30]_n$ and $[\pm 55]_n$ (n = 6,12) MMB specimens at various mixed mode ratios are shown in Figs. 4.25 through 4.28. P-δ curves are not shown for the $[\pm 85]_6$ and $[\pm 85]_{12}$ lay-ups because these specimens failed in flexure prior to delamination propagation. The filled circles on the graphs mark visually observed onset of crack propagation.

The P-δ curves for the $[\pm 30]_6$ laminates, Fig. 4.25, are quite linear prior to crack growth. The $[\pm 55]_6$ laminates, however, Fig. 4.26, display nonlinear response due to matrix yielding and possible micro-cracking before the onset of crack propagation and some permanent deformation after unloading. For the thicker $[\pm 30]_{12}$ and $[\pm 55]_{12}$ laminates, Figs. 4.27 and 4.28, the P-δ curves are more linear and display less permanent deformation. The nonlinearity of the P-δ response curves prior to delamination growth and permanent deformation upon unloading increased with decreased thickness and mode ratio, G_I/G_{II}, and increased ply angle. Similar to the behavior of the previously examined DCB specimens, Sect. 4.2.2, crack propagation at large G_I/G_{II} ratios (mode I dominated) occurred initially in a stable manner at progressively increasing load evidencing R-curve behavior until delamination growth was arrested, Figs. 4.25b, 4.26b, 4.27b, and 4.28b. On the other hand, crack propagation at small G_I/G_{II} ratios (mode II dominated) was unstable, see e.g., Fig. 4.27a. Such behavior was observed also in ENF (mode II) testing of the laminates, Sect. 4.2.3. While the DCB specimen is inherently stable, the ENF geometry is unstable under displacement control. After some increment of crack growth,

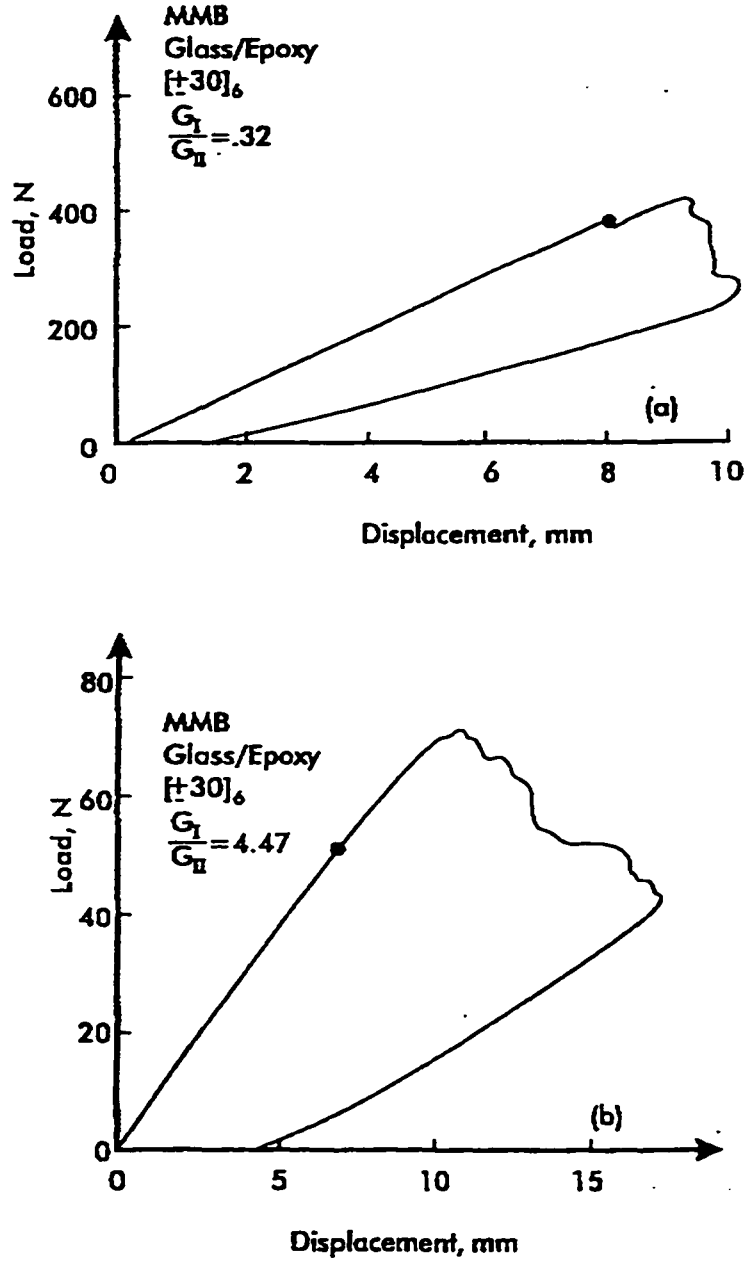

Fig. 4.25 Load-displacement curves for a $[\pm 30]_6$ glass/epoxy MMB specimen, a) c = 28 mm, b) c = 97 mm.

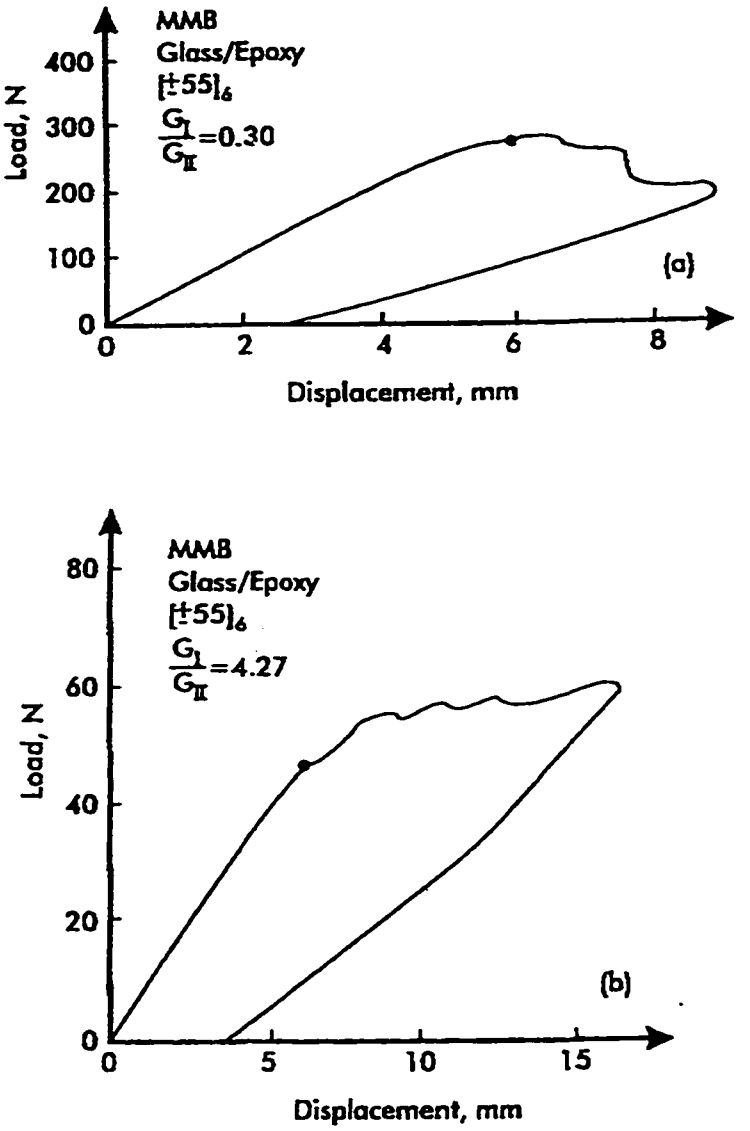

Fig. 4.26 Load-displacement curves for a $[\pm 55]_6$ glass/epoxy MMB specimen, a) c = 28 mm, b) c = 97 mm.

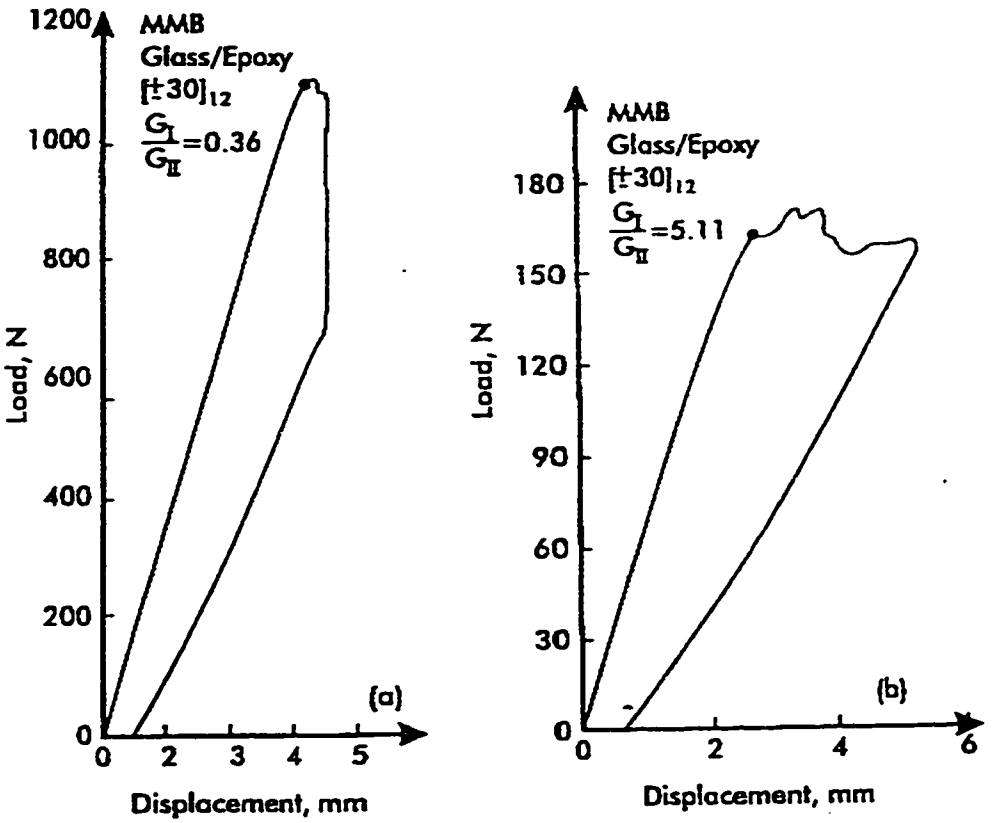

Fig. 4.27 Load-displacement curves for a $[\pm 30]_{12}$ glass/epoxy MMB specimen, a) c = 28 mm, b) c = 97 mm.

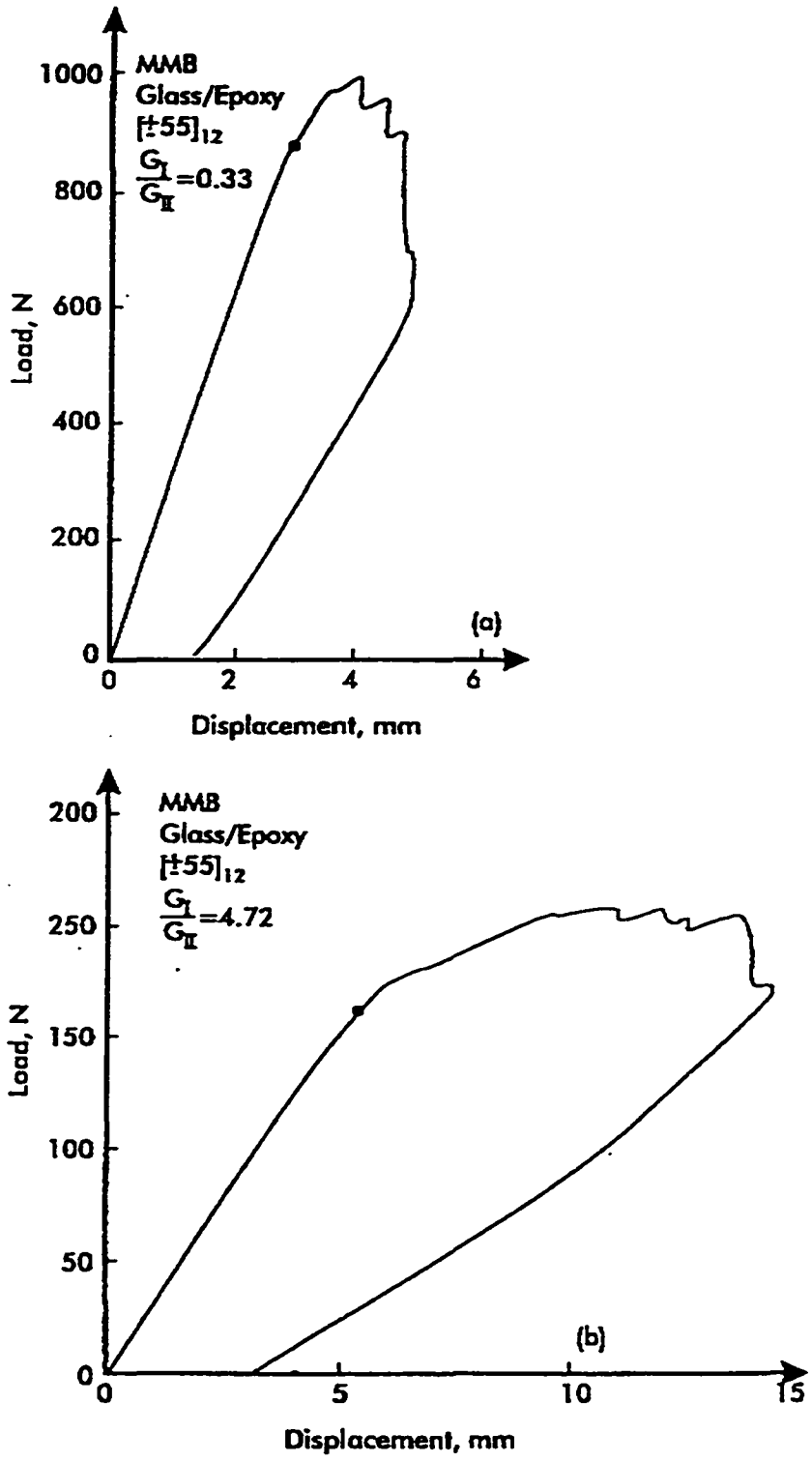

Fig. 4.28 Load-displacement curves for a $[\pm 55]_{12}$ glass/epoxy MMB specimen, a) c = 28 mm, b) c = 97 mm.

the crack tip would intersect a region of interlaced fiber bundles originating from the filament winding process which would arrest further growth. When the crack grew in a stable manner, the arrested interlaminar crack eventually jumped to another interface in the upper (compression-dominated) sub-laminate of the specimen. Crack jumping resulted in sudden and large vertical drops in fracture load, as is especially evident in Fig. 4.28b.

Fracture toughness, G_c, was reduced using the linear elastic fracture mechanics (LEFM) approach. Although there are nonlinearities present, LEFM would produce conservative toughness data. The effective extensional and out-of-plane moduli, E_x and E_z, Table 4.9, the area moments of inertia I_1 and I_2 for the upper and lower arms, and the effective bending compliances d_{11} for the cracked and uncracked regions of the MMB specimen were calculated from basic ply properties, Table 3.2, and measured beam cross-sectional dimensions. Then, G/P^2 was calculated from eq. (3.65) for each specimen as a function of crack length. To determine G_c at any given crack length, the critical load P_c corresponding to the onset of crack growth was measured in a MMB fracture test and substituted in the G/P^2 relation at that crack length.

Table 4.15 lists the initiation values of fracture toughness obtained from the MMB tests. For completeness, G_c values measured in the previous DCB and ENF tests of the glass/epoxy laminates, Sects. 4.2.2 and 4.2.3, are included in Table 4.15. No data is listed for the $[\pm 85]_6$ and $[\pm 85]_{12}$ lay-ups since they failed in flexure prior to interlaminar crack growth. The initiation values of mixed mode fracture toughness in Table 4.15

Table 4.15 Initiation values of mixed mode fracture toughness for glass/epoxy MMB specimens.

Lay-up	$[\pm 30]_6$				$[\pm 55]_6$				$[\pm 30]_{12}$				$[\pm 55]_{12}$			
G_I/G_{II}	0 ENF	0.32	4.47	∞ DCB	0 ENF	0.30	4.27	∞ DCB	0 ENF	0.36	5.11	∞ DCB	0 ENF	0.33	4.72	∞ DCB
G_c J/m^2	1780 ± 400	1080 ± 10	411 ± 11	172 ± 45	1360 ± 50	1030 ± 113	525 ± 126	219 ± 49	1830 ± 110	1040 ± 179	359 ± 47	369 ± 17	2620 ± 330	1340 ± 10	903 ± 64	403 ± 60

represent crack growth directly from the insert. The G_c values for the ±30° interface are independent of laminate thickness within the experimental scatter. For the ±55° interface, however, the data indicates a steep apparent increase of G_c with increased laminate thickness. This anomaly is attributed to the nonlinear behavior observed prior to crack growth in these highly flexible laminates. Such problems were also observed in DCB and ENF tests of the $[\pm 55°]_6$ laminates, Sects. 4.2.2 and 4.2.3. The linear elastic toughness data determined for these laminates is overly conservative and not considered reliable. Figure 4.29 shows G_c plotted versus the mode II fraction, G_{II}/G (with data for the $[\pm 55°]_6$ laminate omitted). The initiation toughness increases with increased mode II fraction (G_{II}/G) and increased angle θ at the $\pm\theta$ interface. Similar trends have been observed for flat, glass/polyester angle-ply laminates, Sect. 4.1.5. A unidirectional glass/epoxy composite displayed a similar toughness trend with increased mode II fraction [64].

In order to monitor the interlaminar crack front after a fracture test, the specimens were unloaded, removed from the MMB fixture, and examined under a strong light source to observe and mark the crack front. Figure 4.30 shows photographs of representative crack fronts for the various mode ratios and lay-ups examined. All fracture specimens exhibited nonuniform crack fronts after growth from the straight insert, as predicted by the nonzero values of the parameter d_c for all lay-ups, see Table 4.11. Inspection of Fig. 4.30 reveals thumb nail shaped cracks, i.e. more crack extension at the center than at the edges, at large G_I/G_{II} ratios (mode I dominated). For more equal shares of G_I and G_{II}, the crack fronts were straighter due to the increased mode II dominance.

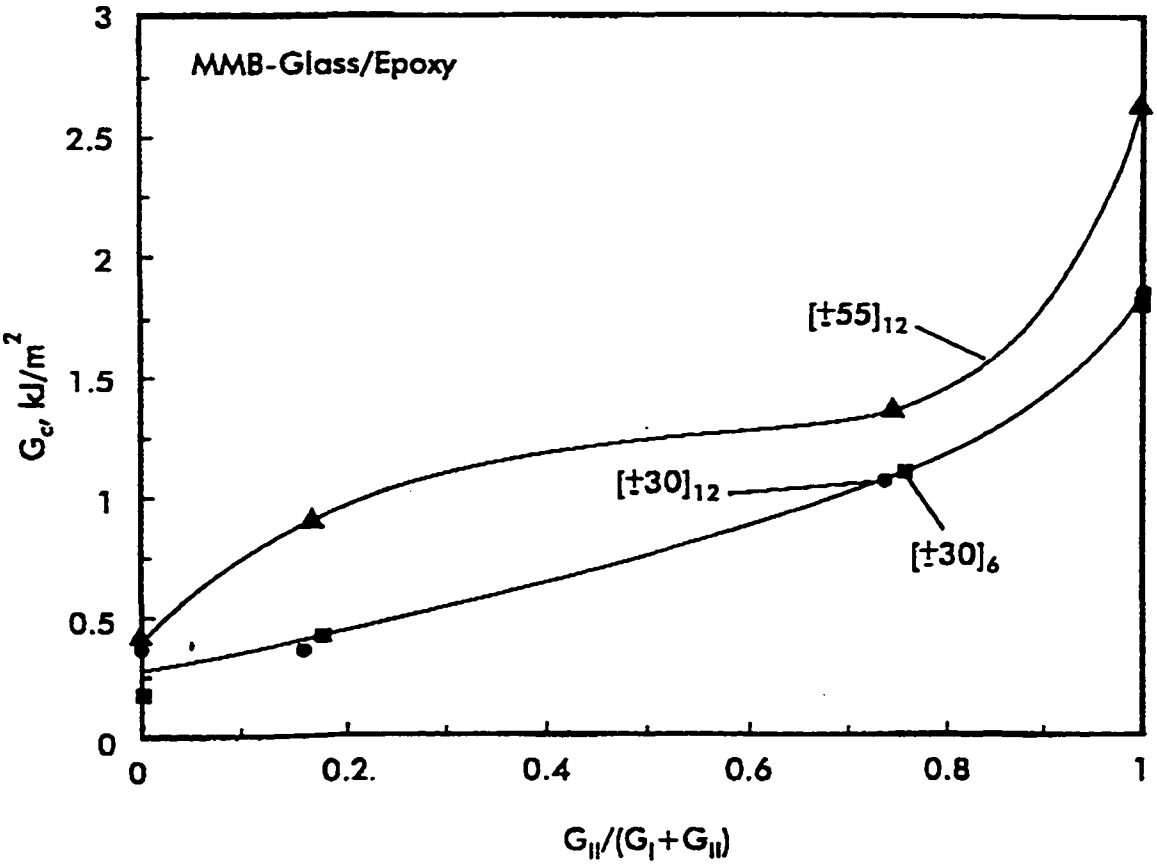

Fig. 4.29 Mixed mode fracture toughness G_c vs. mode II fraction (G_{II}/G) for glass/epoxy laminates.

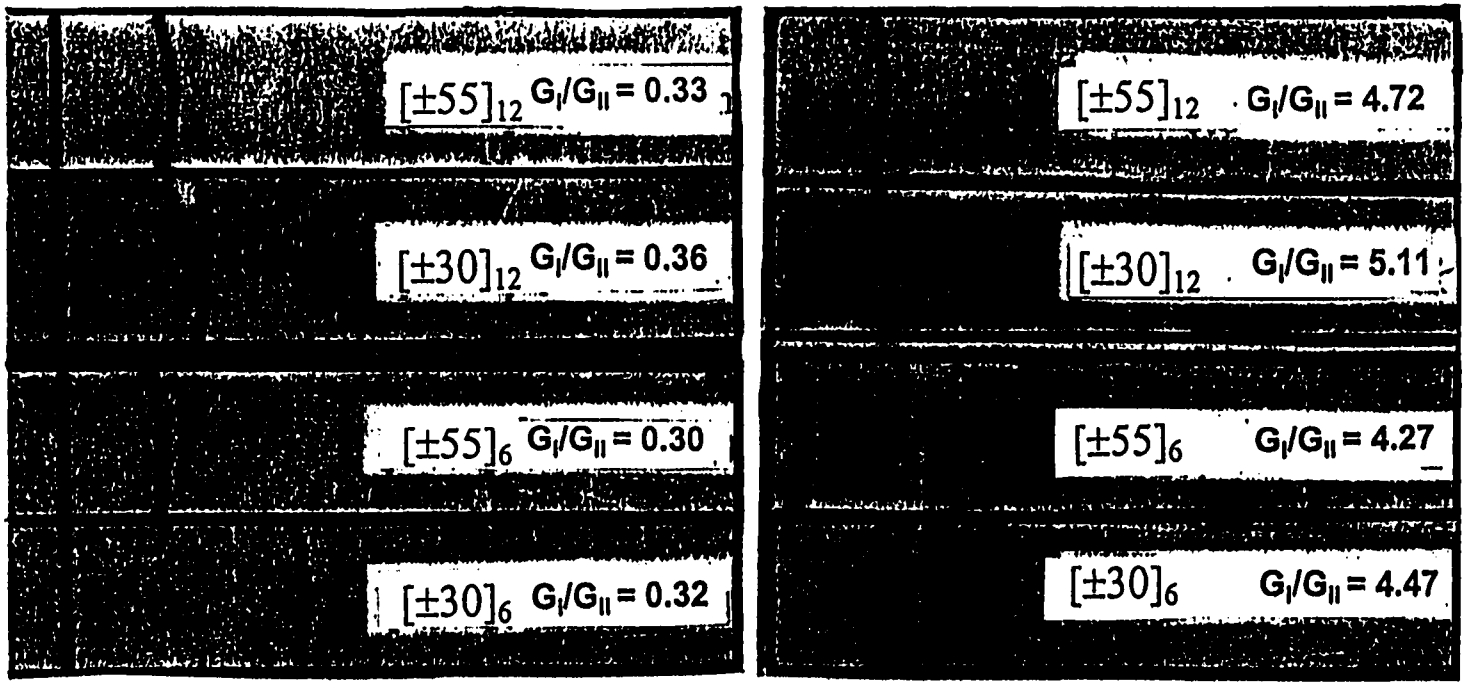

Fig. 4.30 Photographs of initial (straight) crack fronts defined by insert film and crack fronts after propagation for $[\pm 30]_6$, $[\pm 55]_6$, $[\pm 30]_{12}$, and $[\pm 55]_{12}$ glass/epoxy MMB specimens. The crack propagated from left to right, a) c = 28 mm, b) c = 97 mm.

Chapter 5 CONCLUSIONS

Delamination growth has been investigated as a potential failure mechanism for filament-wound composite cylinders used for offshore and underwater structures. Analysis and experiments on DCB, ENF, and MMB beam fracture specimens machined from angle-ply laminate panels and filament-wound composite cylinders are presented. Bending analysis of beam fracture specimens machined from flat panels and composite cylinders was derived from first order shear deformation theory and one-dimensional expressions obtained from laminated plate and shell theories. Elastic foundation effects were included in the DCB specimen analysis. Experiments on flat, glass/polyester laminate beam specimens considered $[0]_6$, $[\pm 30]_5$ and $[\pm 45]_5$ lay-ups with mid-plane delaminations. Experiments on beam specimens machined from composite cylinders were conducted on $[\pm\theta]_6$ and $[\pm\theta]_{12}$ lay-ups with mid-surface delaminations where θ = 30°, 55° and 85°.

For all lay-ups considered, laminated beam model predictions of compliance and energy release rate were in good agreement with experimental data over the range of laminate thicknesses, ply angles, and crack lengths examined. Comparison of analytical predictions with experimental data showed that elastic foundation effects are important to consider for the built-in beams of the DCB specimen. Shear deformation influences the

compliance of the ENF specimen, but has negligible influence on the energy release rate. Fracture toughness for delamination propagation was examined for flat glass/polyester panels and glass/epoxy cylinders. Laminated beam theory models produced similar fracture toughness as the empirical compliance calibration method. The $[\pm 30]_6$ and $[\pm 55]_6$ glass/epoxy laminates were found to be too compliant to allow application of LEFM. The $[\pm 85]_n$ (n = 6,12) glass/epoxy laminates failed in flexure prior to crack propagation. Mode I fracture toughness showed resistance (R-curve) behavior due to fiber and bundle bridging of fracture surfaces. The initiation value of mode II fracture toughness, G_{IIc}, was much larger than the initiation value of mode I fracture toughness G_{Ic}. The initiation value of mixed mode fracture toughness, G_c, increased with decreased ratio G_I/G_{II} and increased ply angle θ. Debonding of transversely oriented fiber bundles was observed as a major crack arrest and fracture resistance mechanism for the flat, glass/polyester angle-ply laminates. Bridging by interlaced fiber bundles and crack jumping to another interface contributed to crack arrest and limited the growth in the curved, glass/epoxy angle-ply laminates. Post-fracture examination of fracture specimens revealed that, for all lay-ups, the crack propagated in a non-uniform manner across the width of the specimen as explained by elastic coupling effects in the laminate beams of the cracked region. Elastic coupling effects in the angle-ply laminates are partially included in the laminated beam formulations, but require more detailed study.

REFERENCES

1. Rajapakse, Y.D.S. (editor), "Mechanics of Thick Composites", AMD - Vol. 162, ASME, New York, 1993.

2. Girala, H.J. and Chaduri, R.A., "Structural Evaluation of Advanced Composite Thick-Section Cylinders Under Biaxial Compressive Loading", in AMD-Vol. 162, Mechanics of Thick Composites, (Y.D.S. Rajapakse ed.), ASME, New York, 1993, p. 227.

3. Slaughter, W.S. and Fleck, N. A., "A Micro-buckling of Fiber Composites," in AMD- Vol. 162, Mechanics of Thick Composites (Y.D.S. Rajapakse ed.), ASME, New York, 1993, p. 67.

4. Kardomateas, G. A. and Chung, C. B., "A Thin Film Modeling of Delamination Buckling in Pressure Loaded Laminated Composite Shells," AIAA J., Vol. 30, 1992, p. 2119.

5. McCullough, R. L., "Introduction to Anisotropic Elasticity", Section 2.1 in Delaware Composites Design Encyclopedia, Vol. 2 (L.A. Carlsson and J.W. Gillespie, Jr. Rev. Eds.), Technomic, Lancaster, 1990, p. 3.

6. Whitney, J. M., "Structural Analysis of Laminated Anisotropic Plates", Technomic, Lancaster, 1987.

7. Jones, R.M., "Mechanics of Composite Materials", McGraw-Hill, New York, 1975.

8. Whitney, J. M., "Lamination Theory and Free Edge Stress Analysis", Sect. 5.4 in Delaware Composites Design Encyclopedia, Vol. 2 (L. A. Carlsson and J.W. Gillespie, Jr. Rev. Eds.), Technomic, Lancaster, 1990, p. 3.

9. Timoshenko, S. P. and Goodier, J. N., Theory of Elasticity, 3rd ed., McGraw Hill, New York, 1970.

10. Reddy, J. N., Mechanics of Laminated Composite Plates, CRC Press, Boca Raton, FL 1997.

11. Carlsson, L. A. and Gillespie, J. W., Jr., "Fracture of Fiber Composites", Structure and Properties of Composites, Vol. 13, VCH, Weinheim, 1993.

12. Ewalds, H. L. and Wanhill, R. J. H., "Fracture Mechanics", Edward Arnold, London, 1989.

13. Carlsson, L. A. and Pipes, R. B., "Experimental Characterization of Advanced Composite Materials" (2nd ed.), Technomic, Lancaster, 1996.

14. Wang, S.S. and Choi, I., "The Interface Crack Between Dissimilar Anisotropic Composite Materials", J. Appl. Mech., Vol. 50, 1983, p. 169.

15. Ting, T.C.T., "Explicit Solutions and Invariance of the Singularities at an Interface Crack in Anisotropic Composites", Int. J. Solids Struct., Vol. 22, 1986, p. 965.

16. Raju, I.S., Crews Jr., J.H. and Aminpour, M.A., "Convergence of Strain Energy Release Rate Components for Edge-Delaminated Composite Laminates", Eng. Fracture Mech., Vol. 30, 1988, p. 383.

17. Suo, Z., "Singularities, Interfaces and Cracks in Dissimilar Anisotropic Media", Proc. Roy. Soc. Lond., Vol. A 427, 1990, p. 331.

18. Suo, Z. and Hutchinson, J.W., "Sandwich Test Specimens for Measuring Interface Crack Toughness", Mater. Sci. Eng., Vol. A 107, 1989, p. 135.

19. Davidson, B.D., Hu, H. and Schapery, R.A., "An Analytical Crack Tip Element for Layered Elastic Structures", J. Appl. Mech., Vol. 62, 1995, p. 294.

20. Davidson, B.D. and Schapery, R.A., "Effect of Finite Width on Deflection and Energy Release Rate of an Orthotropic Double Cantilever Beam Specimen", J. Compos. Mater., Vol. 22, 1988, p. 641.

21. Sun, C. T. and Zeng, S., "Delamination Characteristics of Double-Cantilever Beam and End-Notched Flexure Composite Specimens", Compos. Sci. Tech., Vol. 56, 1996, p. 451.

22. Davidson, B.D., "An Analytical Investigation of Delamination Front Curvature in Double Cantilever Beam Specimen", J. Compos. Mater., Vol. 24, 1990, p. 1124.

23. Crews, J.H. Shivakumar, K.N. and Raju, I.S., "Strain Energy Release Rate Distribution for Double Cantilever Beam Specimen", AIAA J., 1991, P. 1686.

24. Nilsson, K.F., "On Growth of Crack Fronts in the DCB Test", Compos. Eng., Vol. 3, 1993, p. 527.

25. Davidson, B.D., Krüger, R. and König, M.,"Effect of Stacking Sequence on Energy Release Rate Distributions in Multi-directional DCB and ENF Specimens", Eng. Fracture Mech., Vol. 55, 1996, p. 557.

26. Davidson, B.D., Krüger, R. and König, M., "Three-Dimensional Analysis and Resulting Design Recommendations for Unidirectional and Multi-directional End-Notched Flexure Tests", J. Compos. Mater., Vol. 29, 1995, p. 2108.

27. Hutchinson, J. W. and Suo, Z., "Mixed Mode Cracking in Layered Materials", Advances in Applied Mechanics, Vol. 29, 1992, p. 63.

28. Sundararaman, S and Davidson, B. D, "New Test Methods for Determining Fracture Toughness as a Function of Mode Mix for Bimaterial Interfaces", Application of Fracture Mechanics in Electronic Packaging and Materials, ASME, EEP-Vol. 1/MD-Vol. 64, 1995, p.141.

29. Todero, T. J., Dodson, C.L and Beckwith, S. W., "G_{Ic} and G_{IIc} Characterization of Filament Wound Carbon/Epoxy Composites", Proc. 32nd Int'l. SAMPE Sympos., April 6-9, 1987, Anaheim, CA, p. 1544.

30. Prel, Y. J., Davies, P., Benzeggagh, M. L., and de Charentenay, F.X., "Mode I and Mode II Delamination of Thermosetting and Thermoplastic Composites", ASTM STP 1012, Philadelphia, PA, 1989, p. 251.

31. Nicholls, D. J and Gallagher, J. P., "Determination of G_{Ic} in Angle-ply Composites a Cantilever Beam Test Method", J. Reinf. Plast. Compos., Vol. 2, 1983, p. 2.

32. Chai, H., "The Characterization of Mode I Delamination Failure in Non-Wowen, Multi-directional Laminates", Composites, Vol. 15, 1984, p. 277.

33. Laksimi, A., Benzeggagh, M. L., Jing, G., Hecini, M. and Roelant, J. M., "Mode I Interlaminar Fracture of Symmetrical Cross-Ply Composites", Compos. Sci. Tech., Vol. 41, 1991, p. 147.

34. Robinson, P. and Song, D. Q., "A Modified DCB Specimen for Mode I Testing of Multidirectional Laminates", J. Compos. Mater., Vol. 26, 1992, p. 1554.

35. Reeder, J. R and Crews, J. H., Jr., "Mixed-Mode Bending Method for Delamination Testing", AIAA J., Vol. 1, No. 7, p. 1270.

36. Wilkins, D. J., Eisenmann, J. R., Camin, R. A., Margolis, W. S. and Benson, R. A., "Characterizing Delamination Growth in Graphite-Epoxy," ASTM STP 775, 1982, p. 168.

37. Kanninen, M. F., "An Augmented Double Cantilever Beam Model for Studying Crack Propagation and Arrest", Int. J. Fracture, Vol. 9, No. 1, 1973, p. 83.

38. Kanninen, M. F., "A Dynamic Analysis of Unstable Crack Propagation and Arrest in the DCB Test Specimen", Int. J. Fracture, Vol. 10, No. 3, 1974, p. 415.

39. Cook, R. D. and Young, W. C., Advanced Strength of Materials, MacMillan, NewYork, 1985.

40. Hyer, M. W. and Knott, T. W., "Analysis of End-Fitting Induced Strains in Axially Loaded Glass-Epoxy Cylinders", in Composite Structs for SMES Plants (NISTIR5024), (R.P. Reed and J.D. McColskey eds.), Oct. 1994.

41. Gere, J. M. and Timoshenko, S. P., Mechanics of Materials, (4th ed.), PWS, Boston, 1997.

42. Carlsson, L. A., Sendlein, L. S. and Merry, S. L., "Characterization of Face Sheet/Core Shear Fracture of Composite Sandwich Beams", J. Compos. Mater., Vol. 25, 1991, p. 101.

43. Whitney, J. M. and Pagano, N. J., "Interlaminar Fracture of Laminated Composite Materials", J. Appl. Mech., Vol. 37, 1970, p. 1031.

44. Gillespie, J. W., Jr. and Carlsson, L. A., "Experimental Characterization of Advanced Composite Materials", in Delaware Composites Design Encyclopedia, Vol. 6 (L.A. Carlsson and J.W. Gillespie, Jr. Rev. Eds.), Technomic, Lancaster, 1990, p. 34.

45. Suo, Z., Bao, G., Fan, B. and Wang, T.C., "Orthotropy Rescaling and Implications for Fracture in Composites", Int. J. Solids Struct., Vol. 28, 1991, p. 235.

46. Nairn, J. A., "Fracture Mechanics of Composites with Residual Thermal Stresses", J. Applied Mechanics, 1997.

47. Hyer, M. W., "Calculations of the Room Temperature Shapes of Unsymmetric Laminates", J. Compos. Mater., Vol. 15, 1981, p. 296.

48. Davies, P. and Rannou, F., "The Effect of Defects in Tubes: Part I. Mode I Delamination Resistance", Appl. Compos. Mater., Vol. 1, 1995, p. 333.

49. The Math Works, Inc., Matlab User's Guide (unpublished), 1992.

50. Personal Communication with Peter Davies, IFREMER, Brest Center, Marine Materials Lab., 29280 Plouzane, France.

51. O'Brien, T. K., Murri, G. B. and Salpekar, S. A., "Interlaminar Shear Fracture Toughness and Fracture Thresholds for Composite Materials", ASTM STP 102, 1989, p. 222.

52. Davies, P., Sims, G. D., Blackman, B. R. K. et al., "Comparison of Test Configurations for the Determination of G_{IIc}: An International Round Robin", Proc. Of ECCM-CTS4, Lisbon, August, 1998.

53. Polaha, J.J., Davidson, B. D., Hudson, R. C., and Pieracci, A., "Effects of Mode Ratio, Ply Orientation and Precracking on the Delamination Toughness of a Laminated Composite", J. Reinf. Plast. Compos., Vol. 15, 1996, p. 141.

54. Chou, I., Kimpara, I., and Kagayama, K., "Mode I and Mode II Fracture Toughness of Differently Oriented Interlaminae of Graphite/Epoxy Composites", 5th ASTM Symposium on Compos. Mater., Atlanta, 1993.

55. Berry, J. P., "Determination of Fracture Surface Energies by the Cleavage Technique", J. Appl. Phys., Vol. 34, 1983, p. 62.

56. Alif. N., Carlsson, L. A., and Gillespie, J. W, Jr., "Mode I, Mode II, and Mixed Mode Interlaminar Fracture of Woven Fabric Carbon/Epoxy", in ASTM STP 1242, 1997, p. 82.

57. Togho K. et. al., "Mode I Interlaminar Fracture Toughness and Fracture Mechanism of Angle-Ply Carbon/Nylon Laminates", J. Compos. Mater., V. 30, No. 6, 1996, p. 650.

58. Landes, J.D. and Begley, J.A., "The Influence of Specimen Geometry on J_{IC}", ASTM STP 514, 1972, p. 24.

59. Rice, J.R. Paris, P.C. and Merkle, J.G., "Some Further Results of J Integral Analysis and Estimates", ASTM STP 536, 1973, p. 231.

60. Liebowitz, H. and Eftis, J., "On Nonlinear Effects in Fracture Mechanics", Eng. Fracture Mechanics", Vol. 3, 1971, p. 267.

61. Spearing, S.M. and Evans, A.G., "The Role of Fiber Bridging in the Delamination Resistance of Fiber-Reinforced Composites", Acta Metall. Mater., Vol. 40, 1992, p. 2191.

62. Shi, Y.B., Hull, D. and Price, J.N., "Mode II Fracture of $\pm\theta$ Angled Laminate Interfaces", Compos. Sci. Tech., Vol. 27, 1993, p. 173.

63. Ducept, F., Davies, P. and Gamby, D., "An Experimental Study to Validate Tests Used to Determine Mixed Mode Failure Criteria of Glass/Epoxy Composites", Composites - Part A, Vol. 28A, 1997, p. 719.

64. Benzeggagh, M. L. and Kenane, K.,"Measurement of Mixed-Mode Delamination Fracture Toughness of Unidirectional Glass/Epoxy Composites with Mixed-Mode Bending Apparatus", Compos. Sci. Tech., Vol. 56, 1996, p. 439.

65. Hyer, M. W., stress Analysis of Fiber-Reinforced Composite Materials", WCB/McGraw-Hill, Boston, 1998.

66. Suo, Z., Bao, G. and Fan, B., "Delamination R-curve Phenomena due to Damage", J. Mech. Phys. Solids, Vol. 40, 1992, p. 1.

67. Baizeau, R., Davies, P. and Choqueuse, D., "Evaluation of the Integrity of Composite Tubes", Progress in Durability Analysis of Composite Systems (A. H. Cardon, H. Fukuda and K. Reifsnider, eds.), Proc. Int'l. Confer. Duracosys 95, Brussels, July 16-21, 1995.

APPENDIX A

Calculation of E_z by a Laminate Homogenization Method

To compute the effective out-of-plane modulus E_z of a laminate, the laminate homogenization method of Hyer and Knott [40] is adopted. A cubic element of the laminate is subjected to a known stress σ_z. The following assumptions are made in the analysis:

1. Normals remain straight, hence the contraction strains in the x and y directions ε_x^o and ε_y^o, are independent of thickness.
2. The laminate is balanced so there is no change in the right angles in the x-y plane, i.e., $\gamma_{xy}^o = 0$.
3. Owing to the thinness of a ply, the normal strain ε_z^0 is assumed to be independent of z within each ply. However, ε_z^0 can vary from ply to ply.

Due to the requirement of continuity of σ_z at each ply interface and assumption #3, σ_z is independent of z and is the same in each ply. For such loading, E_z becomes,

$$E_z = \frac{\sigma_z}{\varepsilon_z^o} = \frac{t}{\sum_{k=1}^{N}\left[\frac{1}{(C'_{33})_k} - \left[\frac{(C'_{13})_k}{(C'_{33})_k}\right] A_{xz} - \left[\frac{(C'_{23})_k}{(C'_{33})_k}\right] A_{yz}\right] t_k} \qquad \text{(A1)}$$

where $t = 2h$ is the full laminate thickness, t_k is the ply thickness, and N is total number of plies in the laminate. The $(C_{ij}^{\cdot})_k$ are the transformed stiffnesses of each ply in the x-y-z coordinate system given as [27],

$$C_{13}^{\cdot} = C_{13} m^2 + C_{23} n^2$$

$$C_{23}^{\cdot} = C_{23} m^2 + C_{13} n^2 \qquad \text{(A2)}$$

$$C_{33}^{\cdot} = C_{33}$$

where C_{ij} are the ply stiffnesses in the principal material directions [27] and $m = \cos\theta$ and $n = \sin\theta$, where θ is the ply angle. A_{xz} and A_{yz} are defined as [27],

$$A_{xz} = \frac{A_{12} A_{27} - A_{22} A_{17}}{A_{11} A_{22} - A_{12}^2} \qquad \text{(A3)}$$

$$A_{yz} = \frac{A_{12} A_{17} - A_{11} A_{27}}{A_{11} A_{22} - A_{12}^2}$$

where A_{11}, A_{22}, and A_{12} are the elements of extensional stiffness matrix [A] of the full laminate, eq. (2.19) and A_{17} and A_{27} are defined as [27],

$$A_{17} = \sum_{k=1}^{N} \overline{Q}_{17}^{k} t_k \qquad \text{(A4)}$$

$$A_{27} = \sum_{k=1}^{N} \overline{Q}_{27}^{k} t_k$$

where $\overline{Q}_{17}$ and $\overline{Q}_{27}$ are defined as [27],

$$\overline{Q}_{17} = \frac{C_{13}}{C_{33}} \tag{A5}$$

$$\overline{Q}_{27} = \frac{C_{23}}{C_{33}}$$

APPENDIX B

Classical Plate Theory (CPT) Analysis for Laminate ENF Specimens

Davidson et al. [25] derived the following classical plate theory (CPT) equations for the compliance, C, and energy release rate, G, of a specially orthotropic, mid-plane symmetric laminate ENF specimen with a delamination at the geometric center,

$$C^{CPT} = \frac{4L^3 + a^3(R-2)}{24b D_u} \tag{B1}$$

$$G^{CPT} = \frac{P^2 a^2 (R-2)}{16 b^2 D_u} \tag{B2}$$

where the symbols L, a, P and b are defined in Fig. 3.5, and D is the effective bending rigidity of the uncracked region of the beam. R is the ratio of flexural rigidities of the laminates of the uncracked and cracked regions,

$$R = D_u / D_c \tag{B3}$$

where subscripts "u" and "c" denote uncracked and cracked, respectively. For "generalized plane stress" conditions, consistent with the present SBT formulation,

$$D_i = \left(D_{11} - \frac{D_{12}}{D_{11}} \right)_i (i = u, c) \tag{B4}$$

where the bending stiffness elements D_{ij} are defined in eq. (2.21).

APPENDIX C

Properties of the Curved Cross-Section of the Beam

Figure C1 illustrates the geometry of a beam with curved cross-section where b is the width of the beam and R_i and R_o are the inner and outer radii of the cylindrical shell from which the beam is extracted, respectively. The dimensions z_i' and h_o can be calculated from the geometry as

$$\begin{aligned} z'_i &= \frac{1}{2}\sqrt{4R_i^2 - b^2} \\ h_0 &= \frac{1}{2}\sqrt{4R_0^2 - b^2} - \sqrt{4R_i^2 - b^2} \end{aligned} \tag{C1}$$

The beam cross-sectional area A is given by,

$$A = A_1 + A_2 - A_3 \tag{C2}$$

where

$$\begin{aligned} A_1 &= R_O^2 \sin^{-1}\left(\frac{b}{2R_O}\right) - \frac{b}{4}\sqrt{4R_O^2 - b^2} \\ A_2 &= b h_O \\ A_3 &= R_i^2 \sin^{-1}\left(\frac{b}{2R_i}\right) - \frac{b}{4}\sqrt{4R_i^2 - b^2} \end{aligned} \tag{C3}$$

Substituting eqs. (C3) and (C1) in eq. (C2), the cross-sectional area A of the beam becomes,

$$A = \frac{b}{4}\left(\sqrt{4R_O^2 - b^2} - \sqrt{4R_i^2 - b^2}\right) + R_O^2 \sin^{-1}\left(\frac{b}{2R_O}\right) - R_i^2 \sin^{-1}\left(\frac{b}{2R_i}\right) \tag{C4}$$

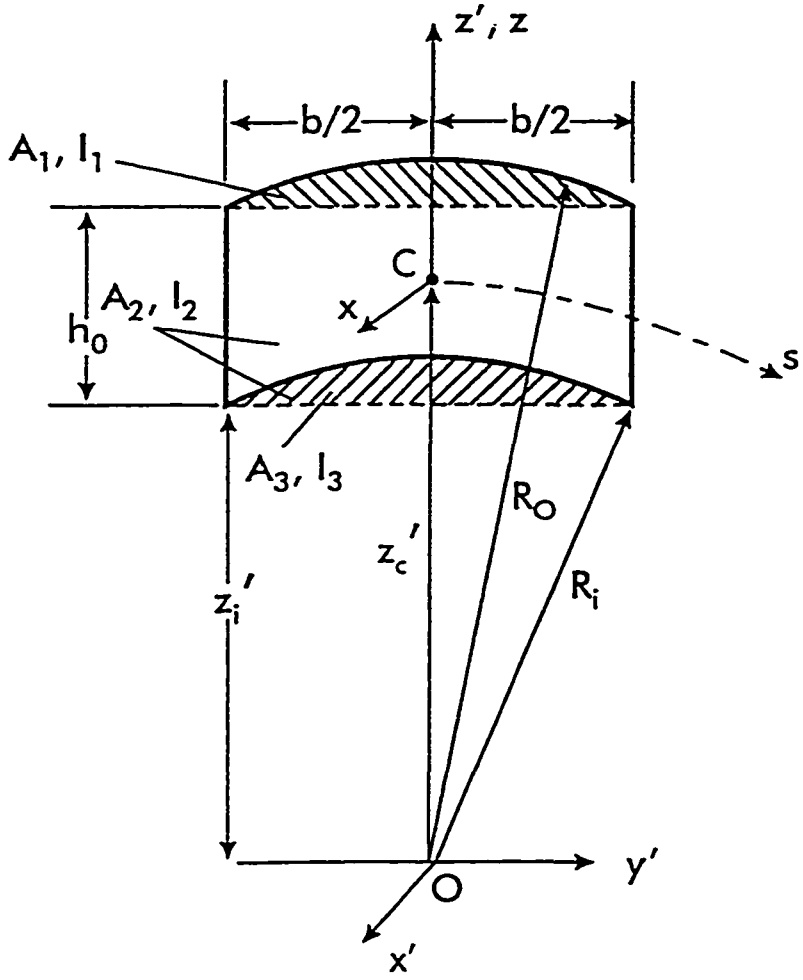

Fig. C1. Geometry of a beam with curved cross-section.

The area moment of inertia of the beam cross-section in Fig. C1 with respect to the y′-axis is given by [41],

$$I_{y'} = \int_A z'^2 \, dA \tag{C5}$$

where dA is an area element and z′ is the distance from the center of the element to the y′-axis. For simplification, the integral in eq. (C5) is split into three contributions,

$$I_{y'} = I_1 + I_2 - I_3 \tag{C6}$$

where

$$\begin{aligned} I_1 &= \frac{R_O^4}{4}\left(\frac{\pi}{2} - \sin^{-1}\left(\frac{\sqrt{4R_O^2 - b^2}}{2R_O}\right)\right) + \frac{b\sqrt{4R_O^2 - b^2}}{16}\left(\frac{b^2}{2} - R_O^2\right) \\ I_2 &= \frac{R_i^4}{4}\left(\frac{\pi}{2} - \sin^{-1}\left(\frac{\sqrt{4R_i^2 - b^2}}{2R_i}\right)\right) + \frac{b\sqrt{4R_i^2 - b^2}}{16}\left(\frac{b^2}{2} - R_i^2\right) \\ I_3 &= \frac{b h_O^3}{12} + \left(z_i + \frac{h_O}{2}\right)^2 b h_O \end{aligned} \tag{C7}$$

To obtain the moment of inertia, I, with respect to the centroid of the cross-section marked as "C" in Fig. C1, we apply the parallel-axis theorem [41],

$$I = I_{y'} - A z'^2_c \tag{C8}$$

where z'_c is the distance between the centroid and the y′-axis, Fig. C1. z'_c is obtained from [41],

$$z'_c = \frac{\int_A z' dA}{\int_A dA} = \frac{b(R_o^2 - R_i^2)}{2A} \tag{C9}$$

Note that the expressions for A, I, and zc' depend on three parameters only, namely, b, R_o, and R_i.

APPENDIX D

Computer Program in MATLAB™ to Compute Thermal Contribution, G^{Th}, to the Energy Release Rate

INTERL.M

```
clear;

% Notation: q1=q11, q2=q22, q3=q33, q4=q12, q5=q16, q6=q26

c0 = [];
c1 = [];
c2 = [];

theta = [30 -30 55 -55 85 -85];
alpha = [6.34 23.3 0]*1e-6;
T = -100;

Z3 = .0:.0005:.003;
Z6 = -.003:.0005:.003;
Z61 = .0:.0005:.006;
Z12 = -.006:.0005:.006;

% z3(i,j),  w.r.t. []3; i--ply number; j--orders.
for i = 1:6
        z3(1,i) = Z3(i+1) - Z3(i);
        z3(2,i) = (Z3(i+1)^2 - Z3(i)^2)/2;
        z3(3,i) = (Z3(i+1)^3 - Z3(i)^3)/3;
end

% z6(i,j),  w.r.t. []6; i--ply number; j--orders.
for i = 1:12
        z6(1,i) = Z6(i+1) - Z6(i);
        z6(2,i) = (Z6(i+1)^2 - Z6(i)^2)/2;
        z6(3,i) = (Z6(i+1)^3 - Z6(i)^3)/3;

        z61(1,i) = Z61(i+1) - Z61(i);
        z61(2,i) = (Z61(i+1)^2 - Z61(i)^2)/2;
        z61(3,i) = (Z61(i+1)^3 - Z61(i)^3)/3;
end

% z12(i,j),  w.r.t. []12; i--ply number; j--orders.
for i = 1:24
        z12(1,i) = Z12(i+1) - Z12(i);
        z12(2,i) = (Z12(i+1)^2 - Z12(i)^2)/2;
        z12(3,i) = (Z12(i+1)^3 - Z12(i)^3)/3;
end
```

```
: Following data generated by Promal---

q(1,:) = [27 11.01 9.136 7.581 9.89 3.959];              %w.r.t. +30
q(2,:) = [27 11.01 9.136 7.581 -9.89 -3.959];            %w.r.t. -30
q(3,:) = [12.62 23.56 10.05 8.492 5.313 9.715];          %w.r.t. +55
q(4,:) = [12.62 23.56 10.05 8.492 -5.313 -9.715];        %w.r.t. -55
q(5,:) = [8.185 39.68 4.206 2.651 .2174 2.56];           %w.r.t. +85
q(6,:) = [8.185 39.68 4.206 2.651 -.2174 -2.56];         %w.r.t. -85

e(:,1) = [-5.994e-4; -1.72e-3; -2.973e-1];               %w.r.t. (+-30)3
e(:,2) = [-5.809e-4; -1.713e-3; -7.328e-2];              %w.r.t. (+-30)6
e(:,3) = [-5.764e-4; -1.711e-3; -1.798e-2];              %       (+-30)12
e(:,4) = [-1.485e-3; -6.706e-4; -3.126e-1];              %       (+-55)3

e(:,5) = [-1.474e-3; -6.503e-4; -7.601e-2];              %       (+-55)6
e(:,6) = [-1.471e-3; -6.453e-4; -1.887e-2];              %       (+-55)12
e(:,7) = [-2.316e-3; -6.295e-4; -9.462e-2];              %       (+-85)3
e(:,8) = [-2.315e-3; -6.284e-4; -2.36e-2];               %       (+-85)6
e(:,9) = [-2.315e-3; -6.281e-4; -5.896e-3];              %       (+-85)12


: Notation in following calculations: i-- w.r.t. ply angles;  j-- w.r.t. layu
ps.

for i = 1:2
        for j =1:3

        c0(i,j) = (q(i,1)*e(1,j)^2 + 2*q(i,4)*e(1,j)*e(2,j) +q(i,2)*e(2,j)^2)
/2 - T*(e(1,j)*(q(i,1)*alpha(1) + q(i,4)*alpha(2) + q(i,5)*alpha(3)) + e(2,j)
*(q(i,4)*alpha(1) + q(i,2)*alpha(2) + q(i,6)*alpha(3)));
        c1(i,j) = T*e(3,j)*(q(i,5)*alpha(1) + q(i,6)*alpha(2) + q(i,3)*alpha(
3)) - q(i,5)*e(1,j)*e(3,j) - q(i,6)*e(2,j)*e(3,j);
        c2(i,j) = (q(i,3)*e(3,j)^2)/2;

        end
end

for i = 3:4
        for j =4:6

        c0(i,j) = (q(i,1)*e(1,j)^2 + 2*q(i,4)*e(1,j)*e(2,j) +q(i,2)*e(2,j)^2)
/2 - T*(e(1,j)*(q(i,1)*alpha(1) + q(i,4)*alpha(2) + q(i,5)*alpha(3)) + e(2,j)
*(q(i,4)*alpha(1) + q(i,2)*alpha(2) + q(i,6)*alpha(3)));
        c1(i,j) = T*e(3,j)*(q(i,5)*alpha(1) + q(i,6)*alpha(2) + q(i,3)*alpha(
3)) - q(i,5)*e(1,j)*e(3,j) - q(i,6)*e(2,j)*e(3,j);
        c2(i,j) = (q(i,3)*e(3,j)^2)/2;

        end
end

for i = 5:6
        for j =7:9

        c0(i,j) = (q(i,1)*e(1,j)^2 + 2*q(i,4)*e(1,j)*e(2,j) +q(i,2)*e(2,j)^2)
/2 - T*(e(1,j)*(q(i,1)*alpha(1) + q(i,4)*alpha(2) + q(i,5)*alpha(3)) + e(2,j)
*(q(i,4)*alpha(1) + q(i,2)*alpha(2) + q(i,6)*alpha(3)));
        c1(i,j) = T*e(3,j)*(q(i,5)*alpha(1) + q(i,6)*alpha(2) + q(i,3)*alpha(
3)) - q(i,5)*e(1,j)*e(3,j) - q(i,6)*e(2,j)*e(3,j);
        c2(i,j) = (q(i,3)*e(3,j)^2)/2;

        end
end

% f3(i,j),  w.r.t. []3; j--30, -30, 55, -55, 85, -85; i--c0, c1, c2
% f6(i,j),  w.r.t. []6; i--30, -30, 55, -55, 85, -85; j--c0, c1, c2
% f12(i,j),  w.r.t. []12; i--30, -30, 55, -55, 85, -85; j--c0, c1, c2

x3_30 = [c0(1,1) c0(2,1); c1(1,1) c1(2,1); c2(1,1) c2(2,1)];
x6_30 = [c0(1,2) c0(2,2); c1(1,2) c1(2,2); c2(1,2) c2(2,2)];
x12_30 = [c0(1,3) c0(2,3); c1(1,3) c1(2,3); c2(1,3) c2(2,3)];
```

```
f3_30 = [x3_30 x3_30 x3_30];
f6_30 = [x6_30 x6_30 x6_30 x6_30 x6_30 x6_30];
f12_30 = [x12_30 x12_30 x12_30 x12_30 x12_30 x12_30 x12_30 x12_30 x12_30 x12_
30 x12_30 x12_30];

x3_55 = [c0(3,4) c0(4,4); c1(3,4) c1(4,4); c2(3,4) c2(4,4)];
x6_55 = [c0(3,5) c0(4,5); c1(3,5) c1(4,5); c2(3,5) c2(4,5)];
x12_55 = [c0(3,6) c0(4,6); c1(3,6) c1(4,6); c2(3,6) c2(4,6)];

f3_55 = [x3_55 x3_55 x3_55];
f6_55 = [x6_55 x6_55 x6_55 x6_55 x6_55 x6_55];
f12_55 = [x12_55 x12_55 x12_55 x12_55 x12_55 x12_55 x12_55 x12_55 x12_55 x12_
55 x12_55 x12_55];

x3_85 = [c0(5,7) c0(6,7); c1(5,7) c1(6,7); c2(5,7) c2(6,7)];
x6_85 = [c0(5,8) c0(6,8); c1(5,8) c1(6,8); c2(5,8) c2(6,8)];
x12_85 = [c0(5,9) c0(6,9); c1(5,9) c1(6,9); c2(5,9) c2(6,9)];

f3_85 = [x3_85 x3_85 x3_85];
f6_85 = [x6_85 x6_85 x6_85 x6_85 x6_85 x6_85];
f12_85 = [x12_85 x12_85 x12_85 x12_85 x12_85 x12_85 x12_85 x12_85 x12_85 x12_
85 x12_85 x12_85];


g3_30 = f3_30.*z3;
g6_30 = f6_30.*z6;
g61_30 = f6_30.*z61;
g12_30 = f12_30.*z12;

g3_55 = f3_55.*z3;
g6_55 = f6_55.*z6;
g61_55 = f6_55.*z61;
g12_55 = f12_55.*z12;

g3_85 = f3_85.*z3;
g6_85 = f6_85.*z6;
g61_85 = f6_85.*z61;
g12_85 = f12_85.*z12;

G3_30 = 0;
G6_30 = 0;
G61_30 = 0;
G12_30 = 0;
G3_55 = 0;
G6_55 = 0;
G61_55 = 0;
G12_55 = 0;
G3_85 = 0;
G6_85 = 0;
G61_85 = 0;
G12_85 = 0;

for i = 1:3
        for j = 1:6
        G3_30 = G3_30 + g3_30(i,j);
        G3_55 = G3_55 + g3_55(i,j);
```

```
        G3_85 = G3_85 + g3_85(i,j);
        end
end

for i = 1:3
        for j = 1:12
        G6_30 = G6_30 + g6_30(i,j);
        G6_55 = G6_55 + g6_55(i,j);
        G6_85 = G6_85 + g6_85(i,j);
        end
end

for i = 1:3
        for j = 1:12
        G61_30 = G61_30 + g61_30(i,j);
        G61_55 = G61_55 + g61_55(i,j);
        G61_85 = G61_85 + g61_85(i,j);
        end
end

for i = 1:3
        for j = 1:24
        G12_30 = G12_30 + g12_30(i,j);
        G12_55 = G12_55 + g12_55(i,j);
        G12_85 = G12_85 + g12_85(i,j);
        end
end

G6_30 = G6_30 - 2*G3_30
G12_30 = G12_30 - 2*G61_30

G6_55 = G6_55 - 2*G3_55
G12_55 = G12_55 - 2*G61_55

G6_85 = G6_85 - 2*G3_85
G12_85 = G12_85 - 2*G61_85
```

IMAGE EVALUATION
TEST TARGET (QA-3)

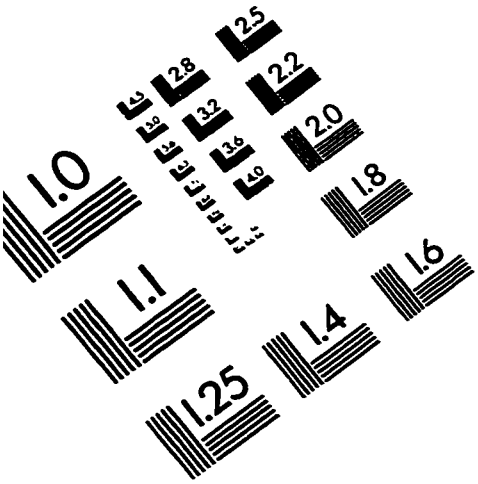

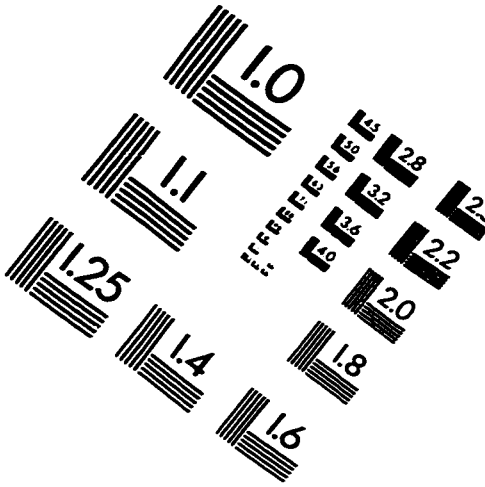

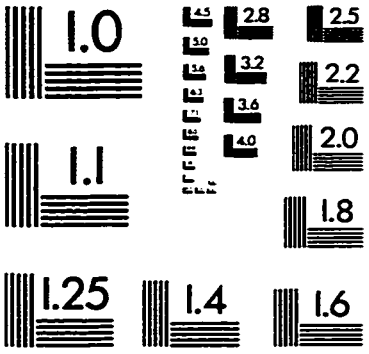

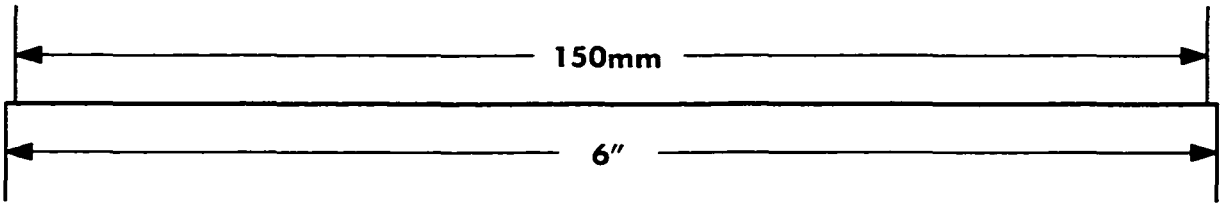

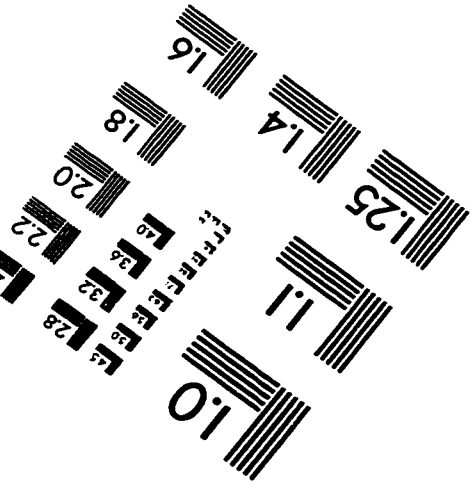

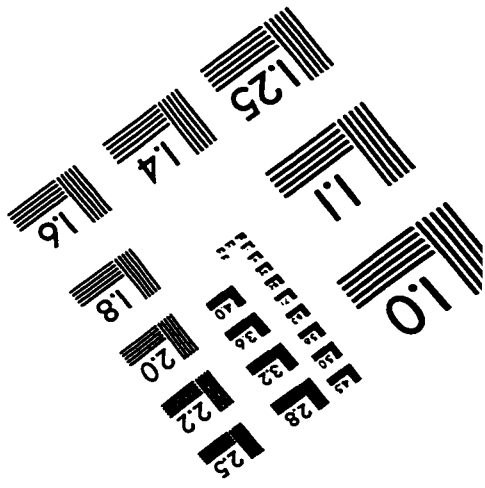

APPLIED IMAGE . Inc
1653 East Main Street
Rochester, NY 14609 USA
Phone: 716/482-0300
Fax: 716/288-5989